**This document is downloaded from DR-NTU (https://dr.ntu.edu.sg)
Nanyang Technological University, Singapore.**

A study of photophysical processes using raman and fluorescence spectroscopy at the ensemble and single molecule levels

Jefri Sanusi Teguh

2014

Jefri Sanusi Teguh. (2014). A study of photophysical processes using raman and fluorescence spectroscopy at the ensemble and single molecule levels. Doctoral thesis, Nanyang Technological University, Singapore.

https://hdl.handle.net/10356/61680

https://doi.org/10.32657/10356/61680

Downloaded on 13 Mar 2024 17:23:44 SGT

A STUDY OF PHOTOPHYSICAL PROCESSES USING RAMAN AND FLUORESCENCE SPECTROSCOPY AT THE ENSEMBLE AND SINGLE MOLECULE LEVELS

JEFRI SANUSI TEGUH

SCHOOL OF PHYSICAL AND MATHEMATICAL SCIENCES

NANYANG TECNOLOGICAL UNIVERSITY

2014

A STUDY OF PHOTOPHYSICAL PROCESSES USING RAMAN AND FLUORESCENCE SPECTROSCOPY AT THE ENSEMBLE AND SINGLE MOLECULE LEVELS

JEFRI SANUSI TEGUH

School of Physical and Mathematical Sciences

A thesis submitted to Nanyang Technological University
in partial fulfillment of the requirement for the degree of
Doctor of Philosophy in Chemistry

2014

ACKNOWLEDGEMENT

Firstly, I would like to express my gratitude to my supervisor Associate Professor Edwin Yeow. Without his constant guidance and advice, this thesis could not be completed.

Secondly, I would like to thank the faculty and officers in Division of Chemistry and Biological Chemistry, School of Physical and Mathematical Sciences. They were a great source of help when I encountered many technical and administrative issues.

Thirdly, I would like to thank my group members, both past and present: Dr. Wu Xiangyang, Dr. Bi Wuguo, Lv Shengtao and Wang Jin. They provided a friendly environment for me to study and work.

Fourthly, I would like to acknowledge Miss Tan Hwee Leng (Analytical Technologies Pte. Ltd.) for her help in microscope Raman setup and Mr. Tok Wee Lee (EINST Technology Pt. Ltd.) for his help in single molecule fluorescence microscope setup.

Special thanks to Miss Tan Ying Shan for her help in electrochemistry measurement and Dr. Lu Yunpeng for his help in computational modeling.

TABLE OF CONTENTS

Acknowledgement **3**

Table of Content **4**

List of Abbreviation **8**

Publications **10**

Summary **11**

Chapter 1 General Introduction **13**

- 1.1 Motivation 14
- 1.2 Charge transfer in SERS 14
  - 1.2.1 Theoretical background of Raman spectroscopy 14
  - 1.2.2 SERS and its mechanism 17
    - 1.2.2.1 Electromagnetic enhancement 18
    - 1.2.2.2 Chemical enhancement 23
  - 1.2.3 Advanced Raman spectroscopy technique 26
    - 1.2.3.1 Anti-Stokes/Stokes Hyper Raman Scattering 26
    - 1.2.3.2 Coherent Anti Stokes/Stokes Raman Spectroscopy 27
- 1.3 Charge movement under electrical field 29
  - 1.3.1 Charge movement in electrical device 30
    - 1.3.1.1 OLED 30
    - 1.3.1.2 Capacitor 34
  - 1.3.2 Charge movement in open and closed circuit 37
- 1.4 Charge movement in conjugated polymer 37
- 1.5 Energy transfer in fluorescence using conjugated polymer nanoparticle system 43

1.6 Förster Resonance Energy Transfer (FRET) 47

1.7 Single Molecule Spectroscopy 50

1.8 Outline of this thesis 53

1.9 References 54

Chapter 2 Surface Enhanced Raman Spectroscopy (SERS) of Nitrothiophenol Isomers Chemisorbed on TiO_2 61

2.1 Introduction 62

2.2 Experimental section 64

2.2.1 Materials 64

2.2.2 Characterization of TiO_2 65

2.2.3 UV-vis absorption and cyclic voltammetry 66

2.2.4 Elemental analysis and Raman spectroscopy 66

2.2.5 Density Functional Theory (DFT) calculation 68

2.3 Results and discussion 68

2.3.1 Surface Enhanced Raman Spectrum (SERS) 68

2.3.2 Absorbance spectrum 83

2.3.3 Cyclic voltammetry 84

2.3.4 DFT calculations 87

2.4 Conclusion 91

2.5 References 91

Chapter 3 Other Origins for the Fluorescence Modulation of Single Dye Molecules in Open-Circuit and Short-Circuit Devices 95

3.1 Introduction 96

3.2 Experimental section 97

3.2.1. Materials 97

3.2.2. Short-circuit device 99

3.2.3. Open-circuit device 99

3.2.4. Single molecule spectroscopy 100

3.2.5. Ellipsometry and AFM 101

3.3 Result and discussion 101

3.3.1. Short-circuit device 101

3.3.2. Open-circuit device 108

3.4 Conclusion 110

3.5 Movie caption 111

3.6 References 111

Chapter 4 Effect of Charge Accumulation on the Stability of PEDOT:PSS During Device Operation 113

4.1 Introduction 114

4.2 Experimental section 117

4.2.1. Materials 117

4.2.2. Device fabrication 117

4.2.3. Device characterization and spectroelectrochemistry 118

4.2.4. Raman spectroscopy 119

4.3 Result and discussion 120

4.3.1. Device characterization and spectroelectrochemistry 120
4.3.2. Raman spectroscopy 122
4.4 Conclusion 128
4.5 References 128

Chapter 5 Fluorescence Intensity Modulation of MEH-PPV Nanoparticle in the Presence of Electric Field and Energy Transfer 130

5.1 Introduction 131
5.2 Experimental section 133
5.2.1. Materials 133
5.2.2. Polymer purification 134
5.2.3. Synthesis of nanoparticles 134
5.2.4. Characterization and bulk spectroscopy 134
5.2.5. Device fabrication 135
5.2.6. Single particle spectroscopy 135
5.3 Result and discussion 136
5.3.1. 5.3.1 Characterization and bulk spectroscopy 136
5.3.2. 5.3.2 Single particle spectroscopy 139
5.4 Conclusion 147
5.5 References 148

LIST OF ABBREVIATION

Alq3	Tris-(8-hydroxyquinoline) aluminum
BEL	Backscattered Excitation Light
CARS	Coherent Anti-Stokes Raman Spectroscopy
CCD	Charge Coupled Device
CE	Chemical Enhancement
CPN	Conjugated Polymer Nanoparticle
CO-520	Polyoxyethylene nonylphenylether
CSRS	Coherent Stokes Raman Spectroscopy
CT	Charge Transfer
DFT	Density Functional Theory
EBL	Electron Blocking Layer
EC	Electric Current
EE	Electromagnetic Enhancement
EF	Enhancement Factor
ETL	Electron Transport Layer
FRET	Förster Resonance Energy Transfer
FTO	Fluorine-doped Tin Oxide
F8BT	poly[(9,9-di-n-octylfluorenyl-2,7-diyl)-alt-(benzo[2,1,3]thiadiazol-4,8-diyl]
HBL	Hole Blocking Layer
HOMO	Highest Occupied Molecular Orbital
HTL	Hole Transport Layer
ITO	Indium Tin Oxide

LUMO	Lowest Unoccupied Molecular Orbital
MEH-PPV	Poly[2-methoxy-5-(2’-ethylhexyloxy)-p-phenylene vinylene]
NTP	Nitrothiophenol
OLED	Organic Light Emitting Diode
PCBM	[6,6]-phenyl C_{61} butyric acid methyl ester
PDHF	Poly(9,9-dihexylfluorene)
PEDOT:PSS	Poly(3,4-ethylenedioxythiophene):poly(styrenesulfonate)
PFB	[poly(9,9-dioctylfluorene-2,7-diyl-*co*-bis-*N,N’*-(4-butylphenyl)-bis-*N,N’*-phenyl-1,4-phenylenediamine]
PFEMO	Poly[9,9-dibromohexylfluorene-2,7-ylenethylene-*alt*-1,4-(2,5-dimethoxy)phenylene
PMMA	Poly(methyl methacrylate)
PPE	Poly(*p*-phenylene ethynylene)
PPV	Poly(phenylene vinylene)
PtOEP	Platinum (II) octaethyl porphine
PS	Polystyrene
PVA	Poly(vinyl alcohol)
PVK	poly(9-vinylcarbazole)
P3HT	Poly(3-hexylthiophene-2,5-diyl)
SERS	Surface Enhanced Raman Spectroscopy
SPAD	Single Photon Avalanche Diode
THF	Tetrahydrofuran
TPD	*N,N’*-bis(3-methylphenyl)-*N,N’*-diphenylbenzidine
TPP	*meso*-Tetraphenylporphyrin

PUBLICATIONS

1.) **Teguh, J. S.**, Sum, T. C., Yeow, E. K. L. Effect of Charge Accumulation on the Stability of PEDOT:PSS During Device Operation *Chem. Phys. Lett.* **2014**, *607*, 52-56.
2.) **Teguh, J. S.**, Kurniawan, M., Wu, X., Sum, T. C., Yeow, E. K. L. Other Origins for the fluorescence modulation of single dye molecules in open-circuit and short-circuit devices *Phys. Chem. Chem. Phys.* **2013**, *15*, 90-93.
3.) **Teguh, J. S.**, Liu, F., Xing, B., Yeow, E. K.L. Surface-Enhanced Raman Scattering (SERS) of Nitrothiophenol Isomers Chemisorbed on TiO_2 *Chem. Asian J.* **2012**, *7*, 975-981.

Conference Presentation:

1.) **Teguh, J. S.**, Yeow, E. K. L. (October 2012, Poster) Surface-Enhanced Raman Scattering (SERS) of Nitrothiophenol Isomers Chemisorbed on TiO_2. 2nd Asian Network for Natural and Unnatural Materials (ANNUM), Nanyang Technological University, Singapore
2.) **Teguh, J. S.**, Yeow, E. K. L. (July 2013, Poster) Surface-Enhanced Raman Scattering (SERS) of Nitrothiophenol Isomers Chemisorbed on TiO_2. 7th International Conference on Materials for Advanced Technologies, Suntec, Singapore.

SUMMARY

This work investigates the phenomenon of charge transfer probed using Raman and fluorescence spectroscopy techniques. Under Raman spectroscopy study, we chose a system of nitrothiophenol (NTP) isomers chemisorbed onto TiO_2 and system of poly(3,4-ethylenedioxythiophene)-poly(styrenesulfonate) (PEDOT:PSS) in a diode-like device. Under fluorescence spectroscopy study, we chose a system of poly[2-methoxy-5-(2’-ethylhexyloxy)-p-phenylene vinylene] (MEH-PPV) nanoparticle under the influence of electric field and energy transfer in a capacitor-like device.

Chapter 1 provides general introduction of Raman spectroscopy and the mechanism of Surface Enhanced Raman Spectroscopy (SERS). Particular attention will be given to chemical enhancement mechanism of SERS which involves charge transfer. Since charge movement is influenced by electric field, the fabrication of proper electrical device is necessary. Application of charge transfer in the fluorescence of conjugated polymer in an electrical device will be described, along with the combined effect of charge transfer and energy transfer.

In Chapter 2, surface enhanced Raman signal of meta- and para-nitrothiophenol (*m*-NTP and *p*-NTP, respectively) were observed when they were chemisorbed onto TiO_2. The enhancement mechanism was deduced from absorption spectrum and Density Functional Theory (DFT) and was found to be due to charge transfer from NTP isomers to TiO_2.

In Chapter 3, fluorescence intensity of single dye molecule (ATTO 647N) and backscattered light intensity were studied in an open and a closed circuit device. In an open circuit, electric field did not influence fluorescence and backscattered light intensity. In a closed circuit, the resulting alternating electric current modulated both fluorescence and

backscattered light intensity. This artificial result was found to be due displacement (i.e. mechanical jerk) of the substrate.

In Chapter 4, Raman spectrum of PEDOT:PSS in OLED (Organic Light Emitting Diode) device was investigated. During OLED operation, holes are injected into PEDOT:PSS, oxidizing it to form a benzoid structures. The vibrational frequency of PEDOT:PSS was found to gradually shift to higher wavenumber. After the operation, it gradually shifted back to its initial wavenumber.

In Chapter 5, fluorescence intensity of a single MEH-PPV nanoparticle was studied in an open circuit. The alternating electric fieldinduces modulation of fluorescence intensity. This result was interpreted in the light dissociation of singlet exciton to become electron and hole polaron. Electric field then induced the movement of hole polaron within the nanoparticle, modulating its fluorescence intensity. An energy acceptor, *meso*-Tetraphenylporphyrin (TPP), was added to the nanoparticle. The resulting composite nanoparticle showed lesser modulation of fluorescence intensity under the influence of electric field. This is interpreted in the light of quenching of singlet exciton via Förster Resonance Energy Transfer (FRET), thereby reducing the probability of dissociation of singlet exciton to become electron and hole polaron.

CHAPTER 1

GENERAL INTRODUCTION

1.1 Motivation

Charge transfer (CT, in particular electron transfer) is ubiquitous. It ranges from simple redox reaction in galvanic cell, iron rusting and battery to a delicate biological redox reaction in the Krebs cycle and in photosystem I/II. Charge transfer can be further harnessed in an electrical device such as light emitting diode and photovoltaic cell since it allows one to control the direction of charge transfer.

Seeing the huge potential in electrical device development, we believe a deeper understanding of charge transfer is crucial. This thesis is dedicated to studying charge transfer processes using both Raman and fluorescence spectroscopy. By studying the enhancement of Raman spectrum, one can deduce the interfacial charge transfer process between an organic adsorbate and the substrate. We are also interested to study how changes in Raman and fluorescence spectrum/intensity can be used to probe charge transfer processes in organic materials found in an electrical device. Finally, we investigated the effect of energy transfer on charge transfer processes in an electrical device.

1.2 Charge transfer in SERS

1.2.1 Theoretical background of Raman spectroscopy

Depending on the cross section, there are a number of possibilities when molecule interacts with light. A molecule can let light pass through, completely absorb light, absorb and emit light at different wavelengths (via fluorescence or phosphorescence), or scatter light. Elastic light scattering by a molecule is known as Rayleigh scattering (named after John Strutt, 3rd Baron Rayleigh) whereas inelastic light scattering is known as Raman scattering (discovered by Chandrasekhara Venkata Raman in 1928). In the simplest case, there are two types of Raman scattering: Stokes-Raman and anti-Stokes-Raman scattering. When the scattered light has lower energy compared to its initial energy, this phenomenon is known as Stokes-Raman scattering. In contrast, anti-Stokes-Raman scattering occurs when the scattered light has higher energy than its initial energy.

We will first try to understand the origin of the three types of scattered light from classical physics.[1] Incident light can be considered an electric field which oscillates with frequency ν_0. At any given time, its electric field can be described as:

$$\vec{E} = \vec{E}_0 \cos(2\pi\nu_0 t) \quad \text{...} \quad (1.1)$$

The incident electric field induces a dipole in the molecule $\vec{\mu}_{ind}$ which can be expressed as:

$$\vec{\mu}_{ind} = \tilde{\alpha}(\nu) \cdot \vec{E}_0 \cos(2\pi\nu_0 t) \quad \text{..................................} \quad (1.2)$$

$\tilde{\alpha}(\nu)$ is a time-dependent polarizability of the molecule and represents the movement of electron cloud as the molecule oscillates from its normal coordinate Q_k with vibrational frequency ν_k. Hence, $\tilde{\alpha}(\nu)$ can be written as:

$$\tilde{\alpha}(\nu) = \tilde{\alpha}_0(\nu_0) + \left(\frac{\partial\tilde{\alpha}}{\partial Q_k}\right)_0 Q_k \cos(2\pi\nu_k t) \quad \text{.........................} \quad (1.3)$$

By combining equations (1.2) and (1.3), one arrives at the expression:

$$\vec{\mu}_{ind} = \vec{E}_0 \left[\tilde{\alpha}_0(\nu_0) + \left(\frac{\partial\tilde{\alpha}}{\partial Q_k}\right)_0 Q_k \cos(2\pi\nu_k t)\right] \cos(2\pi\nu_0 t) \quad \text{.............} \quad (1.4)$$

Using the trigonometric identity $\cos\ A\ \cos\ B = 0.5\{\cos(A+B\} + \cos(A-B)\}$, one can rewrite equation (1.4) as

$$\vec{\mu}_{ind} = \vec{E}_0 \tilde{\alpha}_0(\nu_0) \cos(2\pi\nu_0 t) + \frac{\vec{E}_0}{2}\left(\frac{\partial\tilde{\alpha}}{\partial Q_k}\right)_0 Q_k \cos[2\pi(\nu_k + \nu_0)t]$$

$$+ \frac{\vec{E}_0}{2}\left(\frac{\partial\tilde{\alpha}}{\partial Q_k}\right)_0 Q_k \cos[2\pi(\nu_0 - \nu_k)t] \quad \text{..............................} \quad (1.5)$$

The sum on the right hand side of equation (1.5) provides polarizability of three different frequencies: ν_0, $(\nu_k + \nu_0)$, and $(\nu_0 - \nu_k)$. The first frequency ν_0 is related to elastic/

Rayleigh scattering, the second frequency $(\nu_k + \nu_0)$ to anti-Stokes-Raman scattering and the third frequency $(\nu_0 - \nu_k)$ to Stokes-Raman scattering.

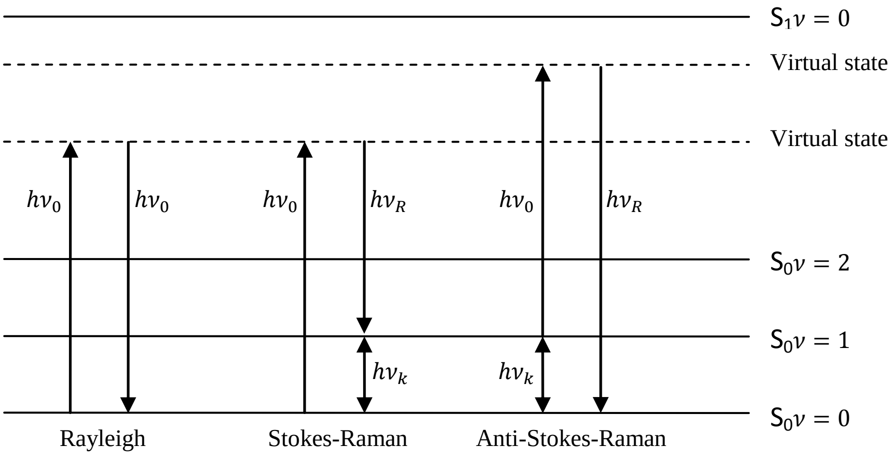
$S_1 \nu = 0$
Virtual state
Virtual state
$h\nu_0$
$h\nu_0$
$h\nu_0$
$h\nu_R$
$h\nu_0$
$h\nu_R$
$S_0 \nu = 2$
$S_0 \nu = 1$
$h\nu_k$
$h\nu_k$
$S_0 \nu = 0$
Rayleigh
Stokes-Raman
Anti-Stokes-Raman

Figure 1: Energy diagram depicting three different types of light scattering. Incident light causes molecule to be excited to a virtual state. A virtual state is an excited state which in most cases has no physical reality since it is not a true vibronic level of the molecule (virtual state is a 'visual' representation of mathematical construction of perturbation theory). From the virtual state, the molecule relaxes either via Rayleigh, Stokes-Raman or Anti-Stokes Raman scattering.

A molecular energy diagram may help to illustrate these three types of scattering (Figure 1). In Rayleigh scattering, the molecule simply scatters the incident light $(h\nu_0)$ without changing its energy. This phenomenon gives rise to the blue color of the sky. Under Stokes-Raman scattering, the scattered light $(h\nu_R)$ has lower energy than the incident light (where $h\nu_R = h(\nu_0 - \nu_k)$). In contrast, in anti-Stokes-Raman scattering, scattered light $(h\nu_R)$ is higher in energy than the incident light (where $h\nu_R = h(\nu_0 + \nu_k)$).

1.2.2 SERS and its mechanism

C. V. Raman discovered inelastic scattering after he measured it from highly concentrated samples. However, intrinsic Raman cross section of many molecules is typically very low (~10^{-29}-10^{-30} cm^2) as compared to absorbance cross section (~10^{-15}-10^{-16} cm^2).[2] Since fluorescence quantum yields of most chromophores are between 10 to 100%, the fluorescence cross section will typically range from ~10^{-16}-10^{-17}. Hence, Raman spectroscopy was initially not widely used as an analytical tool despite its advantage of revealing vibrational fingerprints of the molecules investigated. The study in this field was later greatly encouraged by the development of the laser due to its high intensity and monochromaticity and improvements in detector sensitivity. In 1974, Fleischman and coworkers obtained a very good Raman signal of pyridine adsorbed onto roughened silver electrode.[3] They attributed the enhancement of Raman signal to an increase in the surface area of silver and hence increase in the number of adsorbed pyridine. However, Van Duyne[4] and Creighton[5] argued that an increase in surface area alone is not enough to account for the large enhancement of Raman signal. Van Duyne then proposed the electromagnetic enhancement mechanism whereas Creighton proposed the chemical enhancement mechanism.

The enhancement factor (EF) of a Raman signal is quantified using the following equation:

$$EF = \frac{\frac{I_{SERS}}{N_{SERS}}}{\frac{I_{NR}}{N_{NR}}} \text{ .... } (1.6)$$

where I_{SERS} is the enhanced Raman intensity, N_{SERS} is the corresponding number of molecules, I_{NR} is the unenhanced Raman intensity and N_{NR} is the corresponding number of molecules. Electromagnetic enhancement has been reported to give EF as high as 10^6-10^{14}

whereas chemical enhancement contribution is only in the range of 10^1-10^2.[6-11] Both enhancement mechanisms will be further explained in the next section.

1.2.2.1 Electromagnetic enhancement

When incident light falls onto a coinage metal surface, the incoming oscillating electric field causes the conduction electrons of metal to oscillate (see Figure 2). The density of electrons, effective electron mass, shape and size of the charge distribution influence the oscillation frequency.[12] The interaction between incident light and the metal surface can be approximated using a quasistatic model. In this model, the incident field with wavelength λ interacts with small spherical particle with radius a where $a/\lambda<0.1$. Hence, the field is approximately uniform around the sphere.

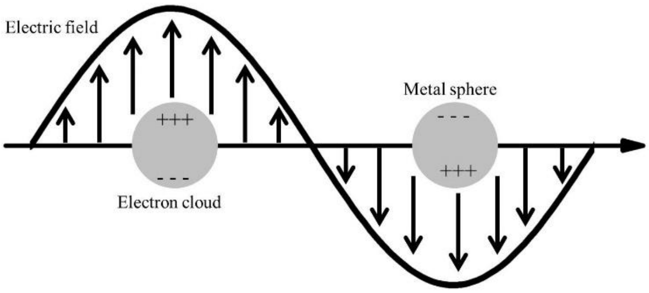

Figure 2: Oscillation of electron cloud of a small metal sphere in response to incident electric field

Let incident electric field vector be E_0. The electric field outside the sphere (E_{out}) can be expressed as:[12]

$$E_{out} = E_0\hat{\boldsymbol{x}} - \alpha E_0\left[\frac{\hat{x}}{r^3} - \frac{3x}{r^5}(x\hat{\boldsymbol{x}} + y\hat{\boldsymbol{y}} + z\hat{\boldsymbol{z}})\right] \text{.......................} \quad (1.7)$$

With *x, y, z* representing Cartesian coordinates and $\hat{\boldsymbol{x}}, \hat{\boldsymbol{y}}, \hat{\boldsymbol{z}}$ their respective vectors, r the radial distance, and α the metal polarizability defined as:

$$\alpha = ga^3 \qquad (1.8)$$

where a is the radius of the sphere and g is defined as

$$g = \frac{\varepsilon_{in} - \varepsilon_{out}}{(\varepsilon_{in} + 2\varepsilon_{out})} \qquad (1.9)$$

ε_{in} is the dielectric constant on the metal nanoparticle whereas ε_{out} is the dielectric constant of the external environment. Electromagnetic enhancement is wavelength dependent as determined by the dielectric constant and its maximum enhancement occurs under resonance condition when $\varepsilon_{in} \approx -2\varepsilon_{out}$. Extinction spectrum $E(\lambda)$ of an arbitrarily shaped nanoparticle can be estimated using Mie theory.

$$E(\lambda) = \frac{24\pi^2 N a^3 \varepsilon_{out}^{\frac{3}{2}}}{\lambda \ln(10)} \left(\frac{\varepsilon_{in}(\lambda)}{(\varepsilon_r(\lambda) + \chi\varepsilon_{out})^2 + \varepsilon_i(\lambda)^2} \right) \qquad (1.10)$$

where ε_r and ε_i are the real and imaginary parts of the metal dielectric function ε_{in}, respectively, χ is the shape factor of nanoparticle and gives the value of 2 for small sphere. The value of χ has to be approximated for other geometry. Hence, extinction spectrum can only be solved analytically for spherical particle. The resonance condition of $\epsilon_r \approx -\chi\epsilon_{out}$ in visible light region is often satisfied for silver and gold nanoparticle.

The equations above show how the metal nanoparticle interacts with incident electric field E_0 and radiates electric field out E_{out}. Equation (1.7) and (1.8) can be simplified to $E_{out} \approx gE_0$. The radiated electric field will interact with molecule located nearby the electric field. Due to its polarizability (equation 1.3), the molecule will then scatter the field E_s with the magnitude of $E_s \approx \tilde{\alpha} g E_0$ (in a more rigorous treatment, polarizability of an isolated molecule may not be the same as polarizability of molecule in the presence of metal particle). This scattered field will interact with metal nanoparticle, causing a second enhancement. The final radiated electric field by nanoparticle E_{SERS} can be expressed as $E_{SERS} \approx g'\tilde{\alpha}gE_0$ where g' is the magnitude of the second enhancement. This process is illustrated in Figure 3.

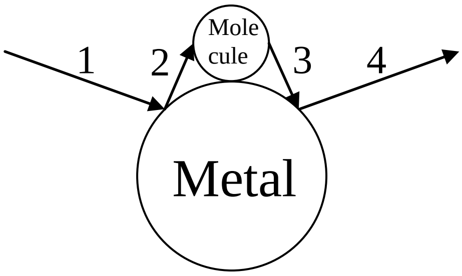

Figure 3: In a simple SERS mechanism, the incident electric field of E_0 (1) interacts with metal and gets enhanced by a factor of g. The enhanced field ($E_{out} \approx gE_0$) (2) interacts with the molecule. The molecule gives off scattered field E_s (3) whose strength is ($E_s \approx \tilde{\alpha}gE_0$) and it gets enhanced by the metal particle by a factor of g'. Finally, the metal radiated the SERS field E_{SERS} with the strength of ($E_{SERS} \approx g'\tilde{\alpha}gE_0$) (4).

The intensity of the scattered field is proportional to the square of the electric field strength. Hence, intensity of incident field is equal of E_0^2 and the intensity of SERS field is equal to E_{SERS}^2. Equation (1.6) can be expressed using E_0^2 and E_{SERS}^2as follows:

$$EF = \frac{\frac{I_{SERS}}{N_{SERS}}}{\frac{I_{NR}}{N_{NR}}} \approx \frac{\frac{E_{SERS}^2}{1}}{\frac{\tilde{\alpha}^2 E_0^2}{1}} \approx \frac{g'^2 g^2 \tilde{\alpha}^2 E_0^2}{\tilde{\alpha}^2 E_0^2} \approx g'^2 g^2 \text{ .... } (1.11)$$

When the Stokes shift is small, $g' \sim g$ and $EF \sim g^4$. In the literature, this is commonly known as the fourth power of local field enhancement on nanoparticle surface. The value of g is about 30 for silver nanoparticle at 400 nm. Hence, the enhancement factor is about 8.1×10^5.[13]

Other than its much larger enhancement factor values, another important feature which distinguishes electromagnetic enhancement from chemical enhancement is its distance dependence; molecule located at a certain distance from the metal nanoparticle can still experience electromagnetic enhancement whereas chemical enhancement requires contact between molecule and metal surface (typically via formation of covalent bond). The intensity of SERS at a certain distance from the metal surface I'_{SERS} can be calculated using the following equation:[14]

$$I'_{SERS} = I_{SERS}(\frac{a+r}{a})^{-10} \quad \text{...} \quad (1.12)$$

where a is the average size of the metal surface responsible for field enhancing, r is the distance between surface and molecule and I_{SERS} is the SERS intensity on the surface of metal (r = 0). One example of modification of r is by using Al_2O_3 spacer deposited via atomic layer deposition technique[14] or by alkane chain spacer fabricated via self-assembled monolayer technique.[15]

In the case whereby the molecule is adsorbed on the metal (r = 0), the electric field irradiated from metallic surface is polarized and this gives rise to surface selection rules. This rule states the vibrational mode perpendicular to the surface will be preferentially enhanced compared to the one parallel to the surface.[16] As such, SERS spectrum can be extracted to give information on the orientation of adsorbate and this has been applied to study the orientation of 1- and 2-napthalenethiol,[17] *p*-nitrophenol,[18] and *p*-mercaptobenzoic acid[19] molecules adsorbed onto metal surface. To illustrate the use of selection rule to determine the orientation of molecule, we will first need to look into the symmetry of vibrational mode. An example of this is given from the adsorption of *p*-aminothiophenol on metal surface.[20] When the molecule is oriented flat on the surface of metal, b_2 mode is more enhanced compared to a_2 and b_1 modes. As a comparison, when the molecule is oriented in a more upright position, a_2 mode is more enhanced than b_2 and b_1 modes (see Figure 4).

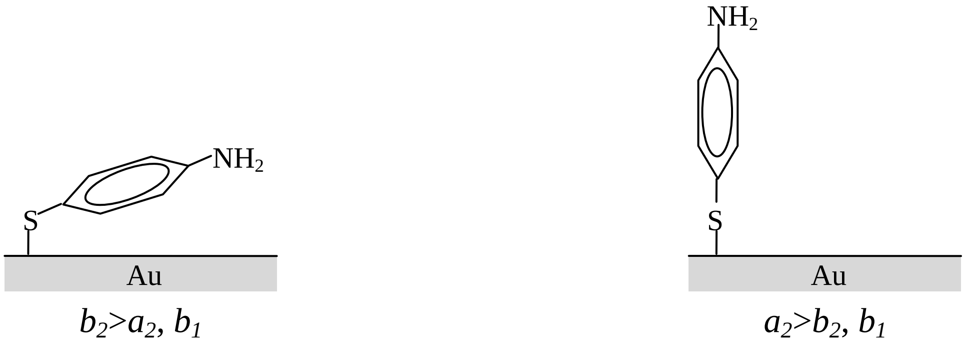

$b_2 > a_2, b_1$ $a_2 > b_2, b_1$

Figure 4: Surface selection rule operating on *p*-aminothiophenol when it is adsorbed onto Au surface. When it is adsorbed in a flat orientation, its b_2 vibrational mode is more enhanced. When it is adsorbed in an upright orientation, its a_2 mode is more enhanced.

Of particular interest is when the molecule is located in between 2 or more metal particles. This interstitial site is often referred to as ‘hot spot’ site. In this site, the EF can be as high as 10^{10}-10^{11}, allowing detection of Raman signal of single molecules.[21-22] The mechanism behind ‘hot spot’ is illustrated in Figure 5.[13,23] When two metal particles are brought together, the incident electric field generates additional electric field in the interstitial site. The molecule which happens to be located inside this site experiences both enhanced incident field and the additional field.

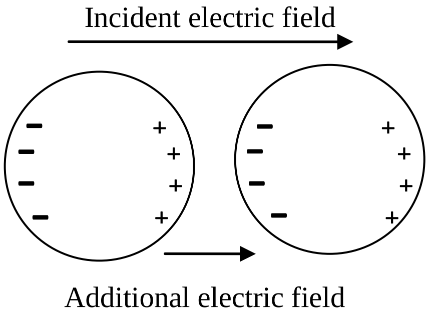

Figure 5: Incident electric field generating additional electric field in between two metal particles, giving rise to the ‘hot spot’ phenomenon.

1.2.2.2 Chemical enhancement

While electromagnetic enhancement is well studied and attractive due to its high enhancement factor, it cannot account for several experimental results. CO and N_2 have almost identical Raman cross section yet their respective SERS spectra are different.[24] Similarly, methane and ethane possess vibrational mode of equivalent strength to that of ethylene or benzene. Yet, SERS of methane and ethane are one hundred fold less intense as compared to SERS of ethylene or benzene.[24] Since many early SERS experiments were conducted on colloidal metal nanoparticles, one would expect to see Raman spectrum of water (poor Raman cross section of water would be compensated with its abundant quantity). However, SERS of water has never been observed. More importantly, SERS of pyridine adsorbed on silver electrode in electrochemical environment shows correlation between maximum Raman intensity and electrode potential and excitation wavelength used.[25] And finally, recent studies have shown SERS of molecules adsorbed onto semiconductor materials such as TiO_2 and ZnO.[26,27]

Chemical enhancement can be thought of as a form of ‘resonance’. In a normal (non-SERS condition) resonance Raman spectroscopy, a molecule is excited from HOMO to LUMO which then gives off Raman signal as it relaxes.[28,29] Depending on the molecule, fluorescence may or may not interfere with the Raman signal. In the presence of nearby metal (SERS condition), the HOMO and LUMO of molecule may form covalent bond and interact with the metal Fermi level. Through this covalent bond, the excitation wavelength (mainly in the visible region) can encourage charge (mainly electron) transfer from molecule to metal or from metal to molecule. Charge transfer will increase polarizability and in turn will enhance Raman signals.

Lombardi *et al.*[30,31] have proposed the charge transfer theory for chemical enhancement. Let us consider a molecule with HOMO level I and LUMO level K interacting with Fermi level of a metal M (see Figure 6).

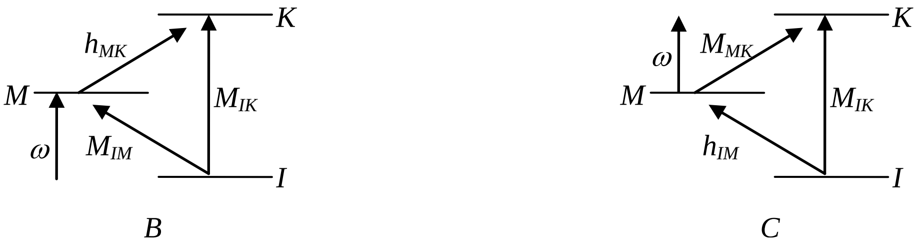

Figure 6: Energy level diagram showing molecule to metal charge transfer (B) and metal to molecule charge transfer (C). I and K are HOMO and LUMO of the molecule, respectively, whereas M is metal Fermi level state. The vibronic coupling between metal and LUMO is represented as h_{MK} whereas the coupling between HOMO and metal is h_{IM}. M_{IM} and M_{MK} represent excitation wavelength assisted charge transfer from molecule to metal and from metal to molecule, respectively. M_{IK} is the direct excitation from HOMO to LUMO (usually in UV region).

Charge transfer polarizability of the system (α_{CT}) can be expressed as

$$\alpha_{CT} = A + B + C \quad \ldots\ldots\ldots\ldots\ldots\ldots\ldots\ldots \quad (1.13)$$

A term is responsible for resonance Raman scattering and only totally symmetric Raman lines are allowed by this term. In practice, many Raman measurements are done using excitation wavelengths far away from molecular resonance. The terms B and C represent charge transfer transition from molecule to metal and metal to molecule, respectively. This transition ‘borrows’ intensity from Herzberg-Teller vibronic coupling constant (h). For B term, the coupling constant operates between metal and the LUMO of the molecule (h_{MK}). In comparison, h_{IM} couples the HOMO of the molecule with metal for C term. When nontotally symmetric normal Raman line is observed, term *B* or *C* or both have to be considered. In addition, they may also influence totally symmetric bands. The complete expressions of *B* and *C* are as follow:

$$B = -\left(\frac{2}{\hbar^2}\right) \sum_{K \neq I} \sum_{M<K} \left[M_{KI}^{\sigma} M_{MI}^{\rho} + M_{KI}^{\rho} M_{MI}^{\sigma}\right] \times \frac{(\omega_{KI}\omega_{MI}+\omega^2) h_{KM} \langle i|Q|f\rangle}{(\omega_{KI}^2-\omega^2)(\omega_{MI}^2-\omega^2)} \quad .... \quad (1.14)$$

$$C = -\left(\frac{2}{\hbar^2}\right) \sum_{K \neq I} \sum_{M>I} [M_{MK}^{\sigma} M_{KI}^{\rho} + M_{MK}^{\rho} M_{KI}^{\sigma}] \times \frac{(\omega_{KI}\omega_{KM}+\omega^2) h_{IM} \langle i|Q|f\rangle}{(\omega_{KI}^2-\omega^2)(\omega_{KM}^2-\omega^2)} \quad ... \quad (1.15)$$

where σ and ρ are representatives of three spatial directions of *x*, *y*, *z* involved in the tensor of normal mode *Q* and *i* and *f* are initial and final Raman transitions, respectively.

In an electrochemical environment, the position of the Fermi level of metal can be tuned by varying the potential. In turn, this method will determine whether the chemical enhancement mechanism is via charge transfer from molecule to metal (term *B*) or metal to molecule (term *C*). Let us first consider term *B*. The maximum Raman intensity occurs when the energy of excitation light is in resonant with ω_{MI} ($\omega = \omega_{MI}$, denominator in equation 1.14). When the external potential is biased more and more positive, the Fermi level of metal drops and the energy of excitation light required for resonance will then be lower. Hence, term *B* predicts a negative slope when one plots external potential against excitation energy. Conversely, for term C, the maximum Raman intensity occurs when energy of excitation light is in resonant with ω_{KM} ($\omega = \omega_{KM}$, denominator in equation 1.15). When the external potential is biased more and more positive, the Fermi level of metal drops and the energy of excitation light required for resonance will then be higher. Hence, term *C* predicts a positive slope when one plots external potential against excitation energy.

An interesting application of charge transfer mechanism has been studied using TiO_2 as a substitute of metal. Depending on the type of molecule used, TiO_2 can support either one of the two directions of charge transfer. SERS of p-mercaptobenzoic acid adsorbed onto TiO_2 showed enhancement of non-totally symmetric band and it was attributed to charge transfer from TiO_2 to molecule.[32] It was proposed that the electron from the valence band of TiO_2 could be excited to a surface state which will then move to the LUMO of the molecule. In contrast, SERS of dopamine adsorbed onto TiO_2 was ascribed to charge transfer from molecule to TiO_2.[26] Dopamine forms strong interaction with TiO_2 in a bi-chelate manner through its two hydroxyl groups. As such, new absorption band was formed and it was interpreted as arising from electron transfer from the HOMO of dopamine to the conduction band of TiO_2.

1.2.3 Advanced Raman spectroscopy technique

Most of the normal Raman or SERS experiments are carried out using monochromatic continuous excitation light with low power density. However, researchers have been able to develop various sophisticated Raman measurement techniques using pulsed laser with high power density and two coherent excitation lights. Two techniques will be explained briefly in the following section, namely Anti Stokes/Stokes Hyper Raman Scattering and Coherent Anti Stokes/Stokes Raman Spectroscopy.

1.2.3.1 Anti-Stokes/Stokes Hyper Raman Scattering

Normal Raman scattering intensity is proportional to the irradiance of the excitation laser used, as described in equations (1.3) and (1.4). On the other hand, hyper Raman scattering occurs when the laser irradiance is sufficiently high. Its intensity is proportional to the square of the irradiance. In Stokes hyper Raman scattering, the detected signal $h\nu_R$ is equal to $2h\nu_0 - h\nu_k$ whereas in anti-Stokes Raman scattering, $h\nu_R$ is equal to $2h\nu_0 +$

hv_k. Kneipp and coworkers reported EF as high as 10^{20} using surface enhanced hyper Raman scattering technique on crystal violet adsorbed on colloidal silver cluster.[33] Figure 7 below illustrates the phenomenon of hyper Raman scattering.

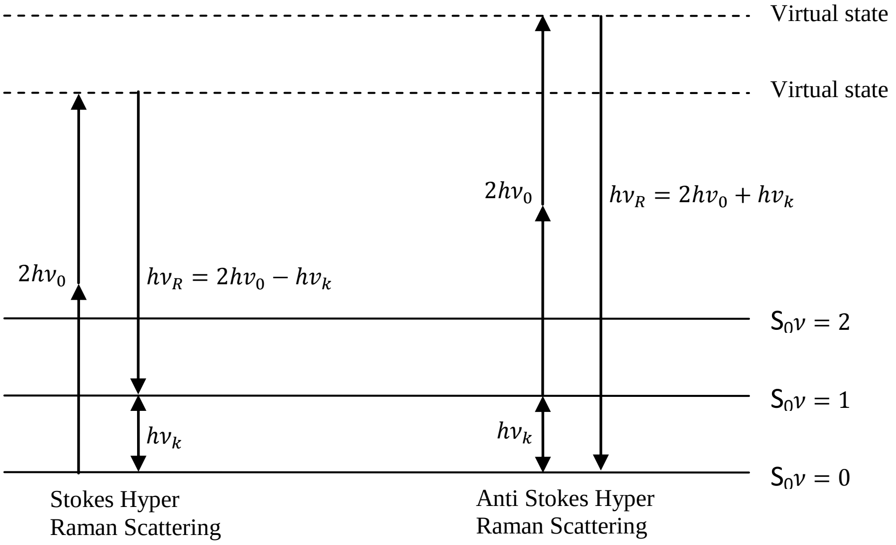
Virtual state
Virtual state
$2hv_0$
$hv_R = 2hv_0 + hv_k$
$2hv_0$
$hv_R = 2hv_0 - hv_k$
$S_0 v = 2$
$S_0 v = 1$
hv_k
hv_k
$S_0 v = 0$
Stokes Hyper Raman Scattering
Anti Stokes Hyper Raman Scattering

Figure 7: Energy diagram of Stokes and Anti-Stokes Hyper Raman Scattering

1.2.3.2 Coherent Anti Stokes/Stokes Raman Scattering

While normal Raman technique utilizes a monochromatic excitation wavelength, it is possible to use two excitation wavelengths (hv_1 and hv_2 where $hv_1 > hv_2$) to study its molecular vibration. This is the basic idea behind Coherent Anti-Stokes Raman Scattering (CARS) and Coherent Stokes Raman Scattering (CSRS). In CARS, the molecule first occupies the lowest vibrational level of the ground state. A constant excitation laser hv_1 acts as a pump to bring the molecule to a virtual state. The second beam is tuned in such a way that $hv_2 = hv_1 - hv_k$. The molecule then occupies the higher vibrational state. The second incident hv_1 excited the molecule to another virtual state. Finally, the molecule gives scattered signal $hv_R = hv_1 + hv_k$ while returning to the lowest vibrational state of the ground level. The scattered signal is said to be 'Anti-Stokes shifted' with respect to $h\nu_1$. On the other hand in the case of CSRS, the molecule first occupies higher vibrational state. The incident $h\nu_2$ is tuned in such a way that $h\nu_2 + h\nu_k = h\nu_1$. The molecule is excited to the virtual state then relaxes to the lowest vibrational state. The second incident $h\nu_2$ causes the molecule to go up to another virtual state. Finally, the molecule relaxes to the higher vibrational level while giving scattered signal $h\nu_R = h\nu_2 - h\nu_k$. The scattered signal is said to be 'Stoke-shifted' with respect to $h\nu_2$. These two phenomenon are illustrated in Figure 8.

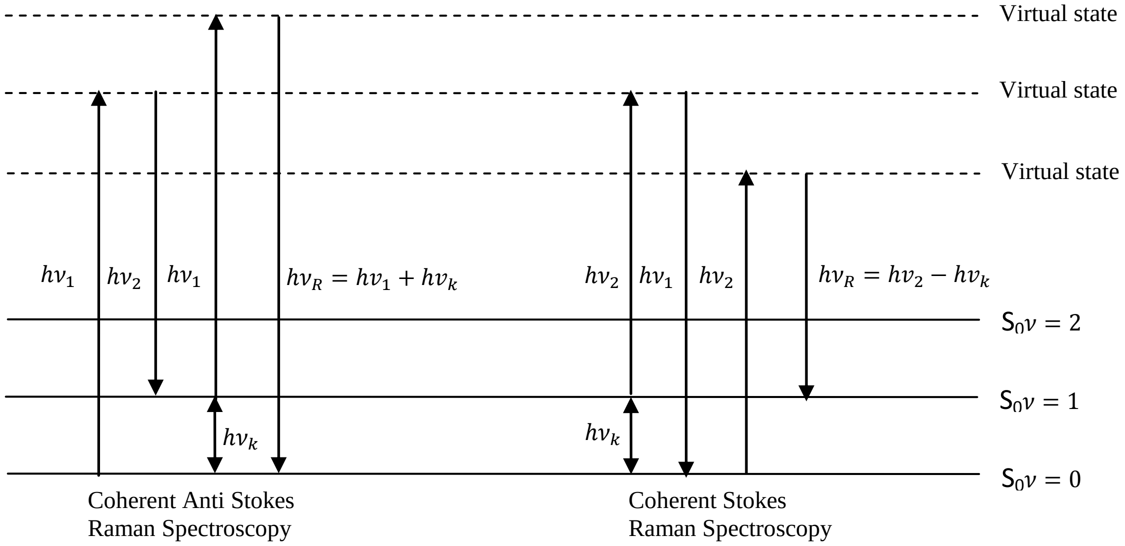
Virtual state
Virtual state
Virtual state
$h\nu_1$
$h\nu_2$
$h\nu_1$
$h\nu_R = h\nu_1 + h\nu_k$
$h\nu_2$
$h\nu_1$
$h\nu_2$
$h\nu_R = h\nu_2 - h\nu_k$
$S_0 \nu = 2$
$S_0 \nu = 1$
$h\nu_k$
$h\nu_k$
$S_0 \nu = 0$
Coherent Anti Stokes Raman Spectroscopy
Coherent Stokes Raman Spectroscopy

Figure 8: Energy diagram of CARS and CSRS

Similar to transient absorption spectroscopy, CARS and CSRS have been used to study vibrational spectrum of a transient species such as radical ions.[34-37] In particular for CARS, since the detected signal is blue-shifted, the fluorescence background is completely suppressed, making CARS suitable tool for investigating biological dye and pigment such as cytochrome c and β-carotene.[38,39]

1.3 Charge movement under electrical field

Charge transfer under chemical enhancement focuses mainly on the electron transfer between molecule and metal/semiconductor. Strictly speaking, when electron moves from one place to another, hole moves in the opposite direction. The movement of both hole and electron are of significant importance in electrical devices such as Organic Light Emitting Diode (OLED) and capacitor.

'Hole' is not merely a term to describe the absence of electron. Depending on the system studied, hole may have heavier or lighter effective mass than electron. Likewise, hole may have faster or slower mobility as compared to electron. It has been found that the effective mass of hole is 20-30% greater than the effective mass of electron in bilayer graphene.[40] In contrast, the effective mass of hole is <1% of the effective mass of electron in TiO_2.[41] Mobility of hole and electron were found to be 3.4×10^{-10} m^2/Vs and 5×10^{-8} m^2/Vs, respectively, in n-type copolymer poly{[*N*,*N*-bis(2-octyldodecyl)-naphthalene-1,4,5,8-bis(dicarboximide)-2,6-diyl]-alt-5,5-(2,2-di-thiophene)}.[42] In contrast, hole and electron mobility were found to be 1.72 and 0.42 cm^2/Vs in poly(*N*-alkyl diketopyrrolo-pyrrole-dithienylthieno[3,2,b]thiophene).[43]

Electron or hole will move under the influence of external electric field. To avoid confusion, 'incident' electric field in the SERS section above is caused by excitation light whereas 'external' electric field here is caused by difference in electric potential. Such potential difference is easily provided via a generator. Hole will move toward the direction of electric field whereas electron will move opposite to the direction of electric field (Figure 9).

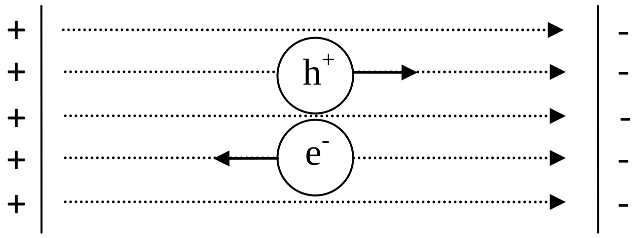

Figure 9: Potential difference between 2 electrodes with opposite charge generates electric field (dashed line). Hole (h^+) will move toward the direction of the field whereas electron (e^-) will move opposite the direction of the field.

1.3.1 Charge movement in electrical device

1.3.1.1 OLED

Electroluminescence is an emission of photon due to electric field. The first study of electroluminescence was reported by Pope *et al.* who investigated luminescence of anthracence during application of 400V potential.[44] About two decades later, Tang *et al.* reported electroluminescence from organic material during potential application of ~10V.[45] Due to application of low potential, this result has since generated world-wide interest in OLED study. The first study of electroluminescence from conjugated polymer was reported in 1990.[46] Conjugated polymer has a lot of potential as OLED material as the emission can be tuned during the synthesis[47,48] and it can be flexible enough to be bent without failure.[49]

The simplest OLED consists of a pair of electrodes and a single emissive layer such as poly(phenylene vinylene) or PPV. The cathode is usually metal with low work function such as aluminum,[47] calcium[50] or magnesium[51] whereas the anode is usually a semitransparent electrode with a high work function such as Indium Tin Oxide (ITO)[47] or Fluorine doped Tin Oxide (FTO).[52] The anode is connected to a positive terminal whereas the cathode is connected to a negative terminal. During application of an external potential, electrons are injected from cathode to the LUMO of PPV whereas holes are injected from anode to the HOMO of PPV. The recombination of electron and hole then produces electroluminescence (see Figure 10). Single OLED device generally does not possess high external quantum efficiency (ratio of photon generated to electrons injected) as the emissive layer is responsible for both transport and emitting functions. Jae *et al.* reported external quantum efficiency of 10^{-4}% for PPV and 10^{-3}% for a PPV derivative as an emissive layer.[53] A solution to improve the efficiency is to employ multilayer OLED device.

`

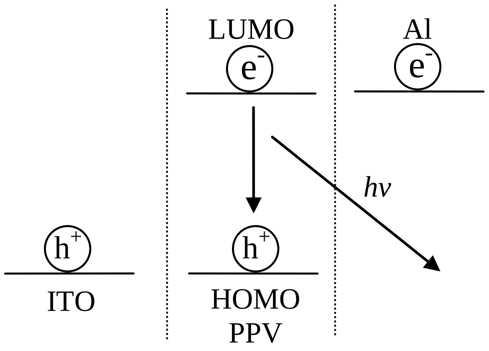

Figure 10: Simple OLED consisting of ITO anode, single PPV emissive layer and Al cathode. Electron hole recombination generates electroluminescence during application of an external potential. Dashed lines indicate interface between two layers.

In a multilayer OLED device, the transport function is mainly performed by the electron transport layer (ETL) and hole transport layer (HTL) whereas the emitting function is done by the conjugated polymer. Examples of ETL include bathocuproine, bathophenanthroline and tris-(8-hydroxyquinoline) aluminum (Alq3) whereas examples of HTL are poly(9-vinylcarbazole) (PVK) and *N*,*N*'-bis(3-methylphenyl)-*N*,*N*'-diphenylbenzidine (TPD). Sometimes, electrons from cathode may pass through the layers and reach anode. Similarly, holes from anode may pass through and reach cathode. This will then create an Ohmic loss. One strategy to further suppress Ohmic loss is by adding electron blocking layer (EBL e.g. tris(4-carbazole)triphenylamine)[54] and hole blocking layer (HBL e.g. diphenyldi(*o*-tolyl)silane).[55] With the addition of EBL and HBL, electron and hole are more confined within the emissive layer, thereby improving its quantum efficiency. Multilayer OLED device has much better external efficiency as compared to single layer OLED device. As an example, Yang *et al*. reported efficiency as high as 3% for a series of poly(paraphenylene) based OLED.[56] The structure of multilayer device is given in Figure 11.

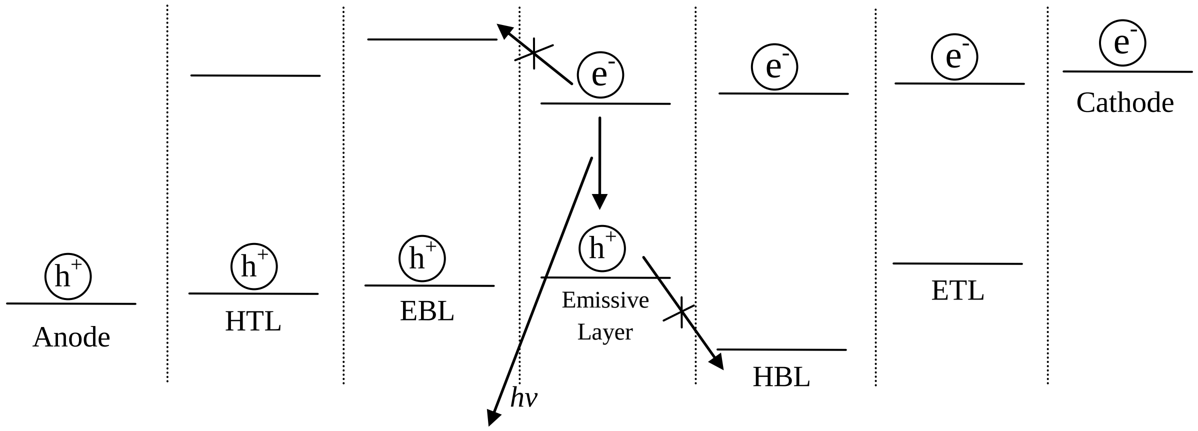

Figure 11: Multilayer OLED device in which external efficiency is improved by the addition of hole transport layer (HTL), electron blocking layer (EBL), hole blocking layer (HBL) and electron transport layer (ETL). The dashed lines represent interface between two layers. EBL prevents electron reaching anode whereas HBL prevents hole from reaching cathode (broken arrow). This will then reduce Ohmic loss as electron and hole are more confined in the emissive layer. Recombination of electron and hole generates electroluminescence light.

A common way of characterizing a diode (both organic and inorganic diode) is by measuring its current against voltage (*I-V* curve). An ideal *I-V* curve is illustrated in Figure 12. A diode allows current to move in a certain direction (forward bias) while restricting current to move in the opposite direction (reverse bias). During the fabrication of a diode, a depletion region is formed (region depleted of holes and electrons). In the forward bias, electrons move from negative electrode to the positive electrode while holes move from positive electrode to the negative electrode. However, the diffusion of electrons/holes in the depletion region is limited by the energy gap which in turn is governed by Boltzmann distribution. Hence, forward bias current is exponential in nature. In the reverse bias, the depletion region becomes wider and acts like a resistor which only allows small current leakage. Hence, reverse bias current is usually far lower than forward bias current. Finally, when the application of reverse bias is too high, the diode will breakdown.

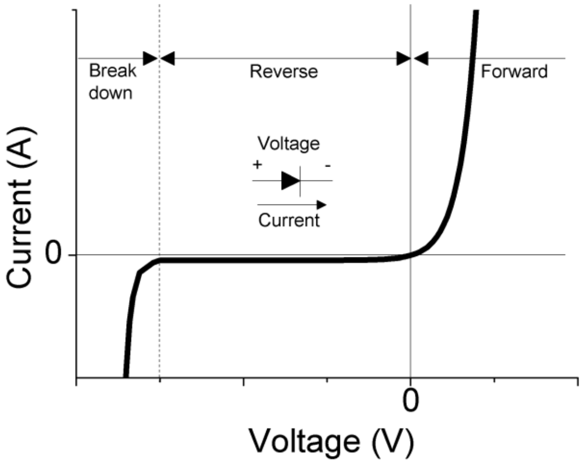

Figure 12: *I-V* curve of a diode.

A simple diode equation to explain I-V curve in the reverse and forward bias is as follows:

$$I = I_s e^{(\frac{V_D}{nV_t})} \quad \text{... (1.16)}$$

where I is the measured current, I_s is the current at reverse bias, V_D is the potential across a diode, V_t is the thermal voltage (approximately 25.7 mV at 298K) and n is the ideality factor. For silicon based diode, the ideality factor reaches 1[57] whereas for organic diode n can be as high as 8.[58] A semi ln plot of *I-V* is routinely used to find the value of n. However, the linearity may only be applicable to relatively small voltage bias. At higher voltage bias the *I-V* curve may deviate from ideal diode behavior as the charge transport is dominated by the bulk properties instead of interface properties.[58]

1.3.1.2 Capacitor

In a capacitor, a layer of insulator is inserted between anode and cathode, typically a very thick polymerlayer[59,60] or an inorganic layer such as SiO_2.[61,62, 63, 64] This insulator allows electric field to pass through but not electric current. Since there is no more ‘anode’ and ‘cathode’, electron and hole movement depends on the material used as the electrode and the direction of electric field. There are two types of charge movement in a capacitor device. The first type is when charge moves from electrode to the active layer. The second type is when charge moves solely within the active layer.

One example of charge transfer from electrode to the active layer is illustrated in the work of Barbara *et al.*[61] They deposited SiO_2 on top on ITO electrode to prevent any charge injection from ITO. On top of SiO_2, they deposited a layer of poly(methyl methacrylate) (PMMA) which contains many single polymer chains of poly[2-methoxy-5-(2’-ethylhexyloxy)-p-phenylene vinylene] (MEH-PPV), continued by deposition of TPD, a hole transport material and completed by deposition of gold electrode (see Figure 13). When the gold electrode was under positive potential, hole polaron from gold moved through TPD and reached MEH-PPV. Hole polaron then quenched MEH-PPV fluorescence (Figure 13a). On the other hand, when gold electrode was under negative potential, hole polaron was removed from MEH-PPV, restoring its fluorescence (Figure 13b). Gesquiere *et al.*[62] reported similar finding: hole polaron quenched fluorescence of poly(3-hexylthiophene-2,5-diyl) (P3HT) nanoparticle at negative potential and hole polaron was removed from P3HT at positive potential, restoring its fluorescence. Quenching of fluorescence by hole polaron is explained in Section 1.3

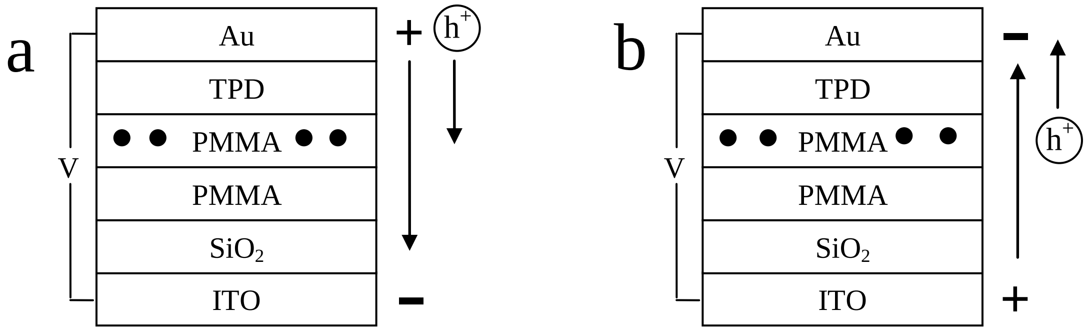

Figure 13: Charge transfer in a capacitor-like device in which the charge moves from electrode to the active layer. When gold electrode is biased positive (a), electric field goes from Au to ITO. Hole is then injected into MEH-PPV as the ‘active layer’, quenching its fluorescence. When gold electrode is injected negative (b), electric field goes from ITO to Au. Hole is then removed from MEH-PPV, restoring its fluorescence. The arrow represents the direction of electric field (● = MEH-PPV single polymer chain).

In the second type of charge transfer in capacitor-like device, the active layer is completely insulated from both electrodes. Scheblykin *et al.*[63,64] deposited SiO_2 on top of ITO electrode to prevent charge injection. Subsequently, they deposited a layer of single MEH-PPV chains in PMMA or polystyrene (PS) matrix, poly(vinyl alcohol) (PVA) and another PMMA layer. PVA and PMMA acted as another insulating layer. The device was then completed with aluminum electrode deposition (Figure 14). During the application of alternating potential bias, the direction of electric field was continuously swapped from ITO to Al and from Al to ITO. There was no charge injection from both electrodes to the active layer of MEH-PPV. MEH-PPV in itself might produce hole polaron depending on the surrounding environment. Hole polaron would then move alongside the chain due to electric field, quenching its fluorescence. The influence of charge transfer on conjugated polymer MEH-PPV is explained in Section 1.3

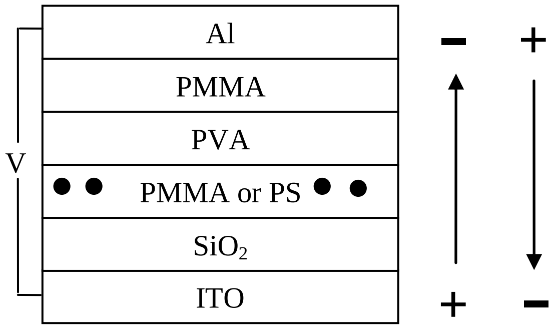

Figure 14: In a capacitor-like device in which MEH-PPV is isolated from both electrodes, only electric field is in operation. The electric field will cause singlet exciton to dissociate to become hole polaron and electron. This hole polaron is then free to move along the chain to quench the fluorescence of the neighboring exciton. The arrow represents the direction of electric field (● = MEH-PPV single polymer chain).

1.3.2 Charge movement in open and closed circuit

It is worthy to note that capacitor is an example of open circuit device as there is no current flowing. On the other hand, OLED can be considered a closed circuit as there is current flowing from one electrode to another electrode, albeit small (~10^{-6} A). A special case of closed circuit is when both electrodes are connected in such a way that the leakage current is much bigger (~10^{-1} A, Figure 15). When the electron or hole moves from one electrode to another in such low resistance, heat will be generated. This heat may cause mechanical deformation of the device which is observable under microscope (further elaborated in Chapter 3).

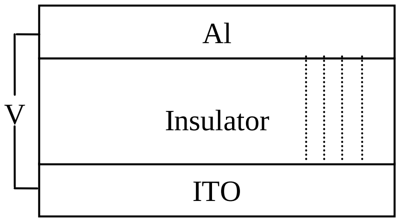

Figure 15: A current leakage (dotted lines) in a capacitor-like device, making it a close circuit and resulting in a large current flowing through the two electrodes. The heat generated by the current will result in mechanical deformation of the device.

1.4 Charge movement in conjugated polymer

Conjugated polymer can be used as an active layer in OLED or capacitor-like devices. As the name suggests, this class of polymer has extensive π-π interaction. Charge can then hop from one π orbital to another π orbital. Some examples of conjugated polymer are MEH-PPV, P3HT and poly[(9,9-di-n-octyl fluorenyl-2,7-diyl)-alt-(benzo[2,1,3] thiadiazol-4,8-diyl] (F8BT). This section will focus mainly on MEH-PPV and its interaction with hole polaron.

A single chain of MEH-PPV consists of multiple chromophores (Figure 16). For example, there are about 200 chromophores (each chromophore consists of 10-17 repeating units) in a single MEH-PPV chain with M_w of about 10^6 amu.[65] Low temperature single chain fluorescence measurement reveals the existence of ‘red’ or low energy site, probably caused by chain-chain contact which improves π stacking and lowers the exciton energy.[66] Incident light excites all the chromophores. High energy chromophores then transfer their energy to the low energy site duringan exciton lifetime (~300 ps). The fluorescence emitted may then come from both the high and low energy sites.[65]

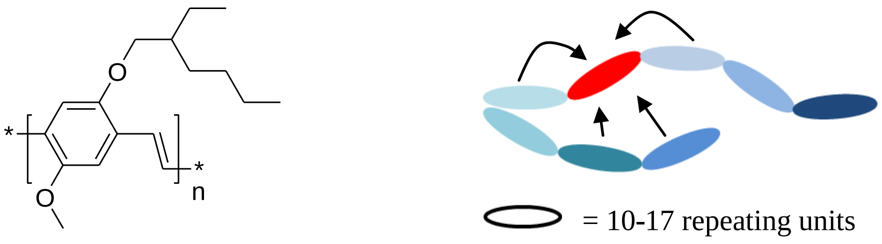

Figure 16: The structure of MEH-PPV. There are about 1700 (n = ~1700) repeating units for a single polymer chain with M_w of 10^6. 10-17 repeating units will make up one chromophore. Hence, a single chain of MEH-PPV may contain ~200 chromophores. After fluorescence excitation, the high energy chromophore will transfer energy to the low energy chromophore. Fluorescence is then a mixture of emission from both the high and low energy sites.

Triplet state of MEH-PPV exhibits interesting property. Navaratnam *et al.*[67] found quantum yield of triplet state to be 1.25% and triplet state lifetime of 92 μs. Barbara *et al.*[68] studied the interaction between triplet state and singlet state of MEH-PPV using a single molecule excitation intensity modulation spectroscopy technique. While triplet state itself does not emit any phosphorescence, they found that the triplet state can quench singlet state of MEH-PPV with a quenching rate of ~10^9-10^{10} s^{-1}. The quenching mechanism was thought to be Förster type quenching. This triplet state can also relax to the ground state with a reverse intersystem crossing rate of ~10^3 s^{-1}.

Scheblykin *et al.*[64] showed that the fluorescence of an isolated MEH-PPV chain can be modulated in the presence of electric field (Figure 14). Singlet exciton of MEH-PPV can undergo electron transfer with an electron acceptor in the surrounding matrix (e.g. carbonyl group of PMMA matrix) or intra chain contact, creating a hole polaron on the chain. Electric field then causes hole polaron to move alongside the chain, quenching other excited chromophores. As a comparison, electric field-assisted formation of hole polaron is strongly suppressed in polystyrene matrix because polystyrene does not possess any electron accepting group and MEH-PPV adopts an open chain conformation, reducing its intra chain contact. This effect is illustrated in Figure 17.

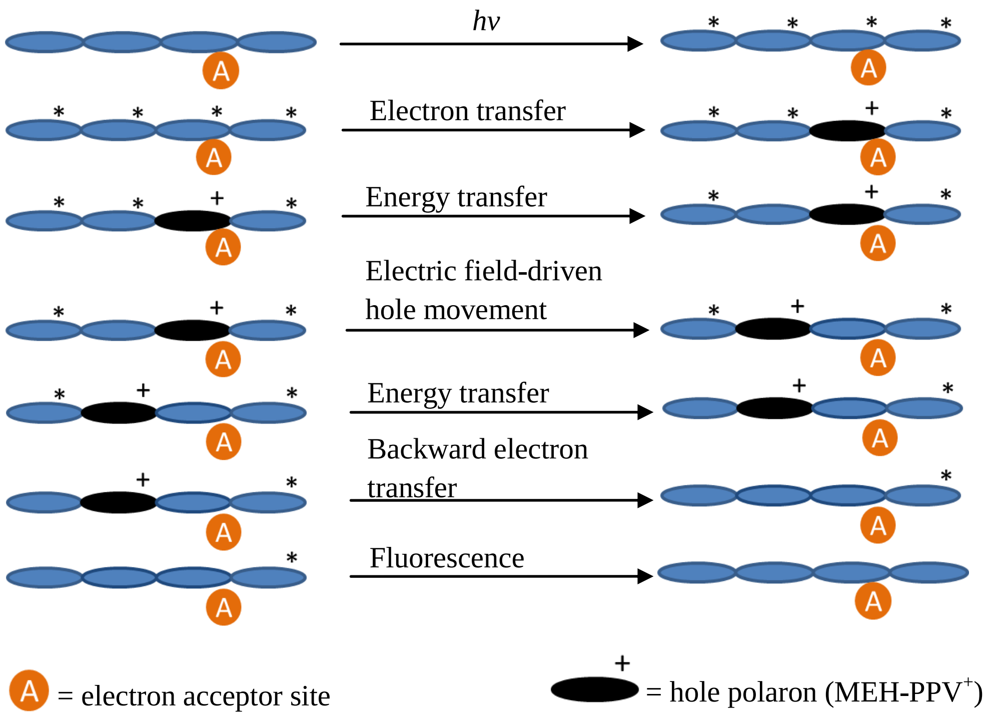
hv
Electron transfer
Energy transfer
Electric field-driven hole movement
Energy transfer
Backward electron transfer
Fluorescence
A = electron acceptor site
+ = hole polaron (MEH-PPV+)

Figure 17: Influence of electric field on the fluorescence of single MEH-PPV chain. Electron transfer from excited chromophore to the neighboring electron acceptor generates a hole polaron (MEH-PPV$^+$). Electric field causes hole polaron to move, quenching another excited chromophore. Backward electron transfer may restore the chromophore to a ground state. Overall, fluorescence of MEH-PPV is reduced.

The formation of hole polaron (MEH-PPV$^+$) can be described using the following equation:[64]

$$\text{MEH-PPV} + \text{acceptor} \underset{k_B}{\overset{k_F}{\rightleftharpoons}} \text{MEH-PPV}^+ + \text{acceptor}^- \;\ldots\ldots\ldots\ldots\ldots\ldots \quad (1.17)$$

The forward rate in this equation is expressed as

$$k_F = k_{exc}(I)\Phi_{cs}(E) \;\ldots\ldots\ldots\ldots\ldots\ldots\ldots\ldots\ldots \quad (1.18)$$

where $k_{exc}(I)$ is the intensity independent excitation rate and $\Phi_{cs}(E)$ is the electric field dependent quantum yield of charge separation. The backward rate is then simply equal to electric field dependent recombination rate

$$k_B = k_{rec}(E) \quad \text{..} \quad (1.19)$$

The equilibrium hole polaron concentration can be expressed as

$$[\text{MEH-PPV}^{+}] = k_F/(k_F + k_B) \quad \text{.................................} \quad (1.20)$$

At this point, Scheblykin *et al.* did not assign any value of forward and backward rates. Individually, different polymer chain responds differently when the electric field moving from ITO to Al and from Al to ITO. However, the averaged response of many single chains is the same, i.e. in average MEH-PPV responds symmetrically to the direction of electric field. It is worthy to note that electric field used in this study was higher (~0.7-1 MV/cm, ignoring the dielectric constant of the polymer layers and silicon dioxide) to induce charge separation and cause movement of hole polaron.

Barbara *et al.*[61] developed a method to induce asymmetric response of MEH-PPV with respect to the direction of electric field (Figure 13 above). Addition of hole transport layer TPD facilitates hole injection at positive bias and hole removal at negative bias. In this work, they could have carried out a control experiment in which no TPD was used. Presumably, in a device with no TPD, no fluorescence modulation would have been observed due to lower electric field in their work (~0.3 MV/cm, ignoring the dielectric constant). The singlet quenching rate by hole was determined to be ~10^{-9} cm^3 C^{-1} s^{-1}.

Finally, Barbara *et al.*[69] combined excitation intensity modulation spectroscopy technique with electric field-induced-hole injection to study the quenching of hole on triplet state and single state. The rate of singlet quenching by hole polaron was found to be ~10^6-10^{12} M^{-1} s^{-1}. This value is different from their earlier work[61] described above, probably because in this work the excitation intensity was modulated. However, the quenching efficiency was <100%. In contrast, the rate of triplet quenching by hole polaron was found to be ~10^7-10^9 M^{-1} s^{-1} and the efficiency was 100%. The rate of quenching of triplet by polaron was slower, probably because it was spin forbidden whereas the quenching of singlet was a spin allowed process. However, the efficiency of triplet quenching was higher as compared to that of singlet quenching because triplet state possesses longer lifetime than singlet state.

Gesquiere *et al.*[70] observed an interesting finding when they studied electric-field induced hole injection in the system of single P3HT:PCBM (Poly(3-hexylthiophene-2,5-diyl): [6,6]-phenyl C_{61} butyric acid methyl ester) nanoparticles in PVA matrix. Similar to Barbara *et al.*[61], Gesquiere *et al.* utilized TPD to facilitate hole injection to P3HT:PCBM. During application of positive potential bias (from 0 to +10V), the injected holes accumulate on the interface of TPD/nanoparticle (which acts as shallow hole trap) and PCBM (which acts as deep hole trap). Holes from shallow traps are removed when the potential bias is reduced from +10V to 0V. During application of reverse potential bias from 0V to -10V, holes are removed from deep traps and an excess electron is built up near nanoparticle/PVA interface which acts as deep electron trap. Detrapping and removal of electrons from deep traps occur during forward potential bias from -10V to +10V. The presence of deep hole and electron traps causes fluorescence of P3HT:PCBM to exhibit hysteresis in the presence of alternating electric field. This opens up possibility of application of P3HT:PCBM in memory devices.

1.5 Energy transfer in fluorescence using conjugated polymer nanoparticle system

In addition to undergoing various charge transfer process due to electric field, conjugated polymer may undergo energy transfer to a nearby energy acceptor. Energy transfer between conjugated polymer and acceptor can be carried out in film phase[71] or in solution phase, provided the acceptor can be permanently brought close enough to the donor (which can be done easily using nanoparticle system).[72]

There are two methods of synthesizing conjugated polymer nanoparticle. The first method is called miniemulsion. The polymer is dissolved in organic solvent which is immiscible with water, for example chloroform.[73,74] The organic solution is then injected into an aqueous solution containing surfactant. The whole mixture is then rigorously stirred or sonicated. Organic phase was then evaporated, resulting in a stable dispersion of nanoparticles in water. Increase in the amount of surfactant results in smaller nanoparticle size. The second method is called reprecipitation method. The polymer is dissolved in organic solvent which is miscible with water, for instance THF.[75] The organic solution is then poured into water under sonication or rigorous stirring. The organic phase is evaporated, resulting in aqueous nanoparticle dispersion. The mechanism of nanoparticle formation is due to hydrophobic effect: the polymer chains are insoluble in water and they fold into spherical spheres to minimize contact with water. Decrease in initial polymer concentration in THF will result in smaller nanoparticle size.

Conjugated polymer nanoparticle finds much application in the optoelectronic biomedical field.List *et al.*[74] showed that methyl substituted ladder type poly(p-phenylene) or m-LPPP nanoparticle could be used as an active layer in an OLED with slightly higher efficiency as compared to the corresponding film based OLED. This efficiency was attributed to enhanced electron injection from aluminum cathode which formed ‘stalactite’ structure during evaporation as a consequence of rough nanoparticle layer surface. Scherf *et al.*[76] utilized a blend of F8BT and PFB nanoparticles in photovoltaic devices with external quantum efficiency of 4% (PFB =poly(9,9-dioctylfluorene-2,7-diyl-*co*-bis-*N,N'*-(4-butyl phenyl)-bis-*N,N'*-phenyl-1,4-phenylenedi-amine). Moon *et al.*[77] demonstrated the use of PPE (poly(*p*-phenylene ethynylene)) nanoparticles in 2 photon imaging of live cells. PPE nanoparticle was found to be nontoxic to cells, making it superior to quantum dot which is toxic to cell despite its high 2 photon cross section.[78] In addition to that, conjugated polymer nanoparticle is generally easier to synthesize than quantum dots. The characteristic of conjugated polymer nanoparticle as an excellent light harvester and energy donor has been reported in a number of studies. McNeill *et al.*[79] developed a system of PDHF (poly(9,9-dihexylfluorene)) nanoparticle as energy donor with PtOEP (platinum (II) octaethyl porphine) as an energy acceptor. After being excited with 350 nm light, PDHF transferred its energy to PtOEP which will then emit phosphorescence. Since phosphorescence is quenched by oxygen, PDHF-PtOEP shows potential as an oxygen sensor in biological system. Xu *et al.*[80] synthesized donor-acceptor system of PFEMO:TPP (poly[9,9-dibromohexylfluorene-2,7-ylenethylene-*alt*-1,4-(2,5-dimethoxy)phenylene]: tetraphenylporphyrin) with CO-520 surfactant (polyoxyethylene nonylphenylether). PFEMO harvested excitation light and transferred its energy efficiently to TPP which was then able to change triplet oxygen to singlet oxygen more efficiently as compared to direct excitation of TPP alone. Hence, PFEMO:TPP:CO-520 presents a potential as photosensitizer in photodynamic therapy.

Conjugated polymer used in this study was MEH-PPV. In its native chain state in THF as solvent, MEH-PPV shows absorbance at around 499 nm due to π-π^* transition and this is generally referred to as singlet exciton. In a bulk level measurement, different conjugation lengths in each chain results in a broad absorption spectrum (Figure 18a, solid line). The fluorescence spectrum is centered at around 553 nm and shows vibronic feature (Figure 18b, solid line). The large Stoke shift (~50 nm) is caused by high energy exciton segment transferring energy to low energy exciton segment.[81] Absorption of MEH-PPV nanoparticle (~75 nm in size) differs from absorption of MEH-PPV in THF in 2 ways. First, the absorption maximum is blue shifted and located at ~490 nm (Figure 18a, dashed line). During nanoparticle formation, polymer chains are forced bend in a constrained volume. The kinks reduce the conjugation length, resulting in the blue shift.[82] Secondly, within the blue shifted absorption, the nanoparticle shows slight increase at around 575 nm. This 'red tail' feature is attributed to locally formed degrees of order. The emission spectrum of MEH-PPV nanoparticle is centered at 590 nm (Figure 18b, dashed line), red shifted to that MEH-PPV in THF. Kinks and bends may increase inter-chain interaction which gives rise to an even lower exciton segment. Energy transfer from high energy exciton to this much lower energy exciton may account for the much larger Stoke shift of MEH-PPV nanoparticle (~100 nm).[82,83] MEH-PPV nanoparticle was used as energy donor.

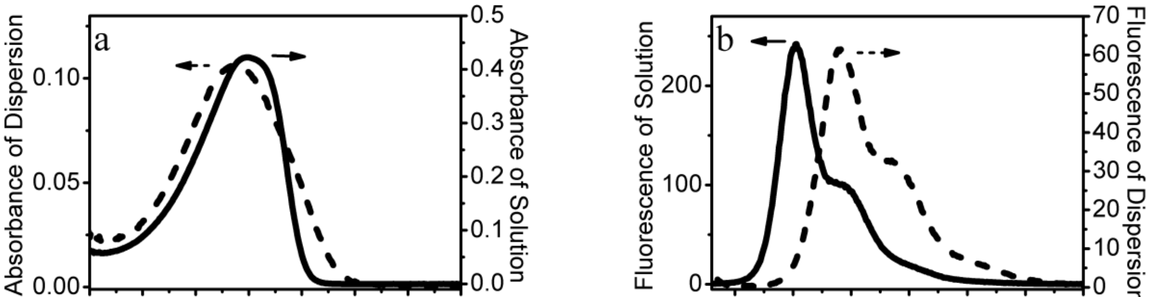

Figure 18: Absorbance (a) and fluorescence (b) of MEH-PPV in THF solution (bold line) and as nanoparticle dispersion (dashed lines). The concentration of MEH-PPV is 5×10^{-3} mg/ml and the nanoparticle size is ~75 nm. Excitation wavelength used to measure fluorescence was 470 nm.

Absorption of tetraphenylporphyrin (TPP) originates from the interaction of its four orbital.[84,85] The spectrum shows $S_0 \rightarrow S_2$ excitation at around 415 nm (also called Soret/B band ($B_{(0,0)}$) and $S_0 \rightarrow S_1$ excitation at around 550 nm (which is also called Q band). More specifically, the absorption bands at 512, 547, 590 and 646 nm can be attributed to $Q_{y(1,0)}$, $Q_{y(0,0)}$, $Q_{x(1,0)}$, $Q_{x(0,0)}$, respectively.[85,86] The internal conversion of $S_2 \rightarrow S_1$ is very rapid, hence S_2 emission is hardly observed. The emission spectrum shows 2 peaks at 650 and 717 nm which are attributed to $Q_{(0,0)}$ and $Q_{(0,1)}$, respectively.[86] The structure of TPP is shown in Figure 19. The absorbance and the emission of TPP in THF are given in Figure 20A and 20B (solid line), respectively.

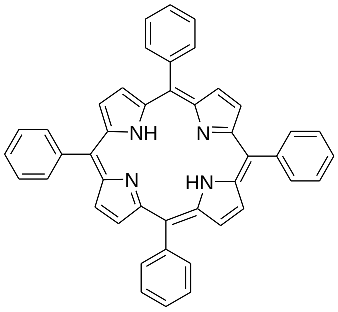

Figure 19: Chemical structure of TPP.

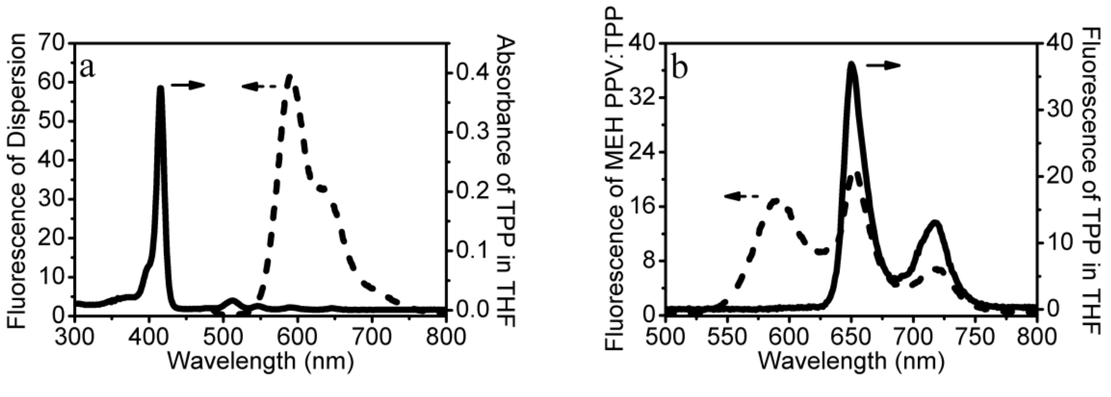

Figure 20: (a) Fluorescence of nanoparticle dispersion (470 nm excitation wavelength) and the absorbance of TPP in THF (5×10^{-4} mg/ml), showing a plausibility of energy transfer. (b) The fluorescence of TPP in THF (excitation wavelength of 415 nm) as compared to fluorescence of MEH-PPV nanoparticle doped with 1%TPP (~80 nm in size).

McNeill *et al.* demonstrated the use of TPP an energy acceptor with PDHF nanoparticle as an energy donor.[87] This work inspired us to use TPP as energy acceptor with MEH-PPV nanoparticle as an energy donor (in chapter 5 of this thesis). The fluorescence of MEH-PPV nanoparticle (Figure 20a, dashed line) overlaps with Q absorption bands of TPP. Fluorescence intensity of MEH-PPV nanoparticle doped with 1%TPP was quenched as compared to that of pure MEH-PPV nanoparticle (Figure 20b dashed line). Excitation wavelength of 470 nm was chosen as it is within the absorption of MEH-PPV nanoparticle and TPP shows negligible absorption in this region. The quenching mechanism was thought to be due to Förster Resonance Energy Transfer (FRET).

1.6 Förster Resonance Energy Transfer (FRET)

Förster Resonance Energy Transfer (FRET) is a process whereby an excited donor, instead of emitting its energy, transfers its energy to a nearby ground state acceptor. An excited acceptor then emits its energy. One will then observe a decrease in donor's emission (quenching) and an increase in acceptor's emission. During this process of energy transfer, the dipole of the excited donor resonates with the dipole of the acceptor. In FRET, the acceptor *does not* accept photon emitted by the donor. FRET is sensitive to the distance between donor and acceptor. Hence the technique is often called 'a spectroscopic ruler'.[88] FRET is routinely used in biological samples for example membrane,[89] nucleic acid,[90] and protein phosphorylation.[91] A mathematical way to calculate the rate of energy transfer is as follows:

$$k_T(r) = \frac{Q_D\kappa^2}{\tau_D r^6}\left(\frac{9000(\ln 10)}{128\pi^5 N n^4}\right)\int_0^\infty F_D(\lambda)\varepsilon_A(\lambda)\lambda^4 d\lambda \text{ ....} \quad (1.21)$$

where $k_T(r)$ is the distance r dependent energy transfer rate, Q_D is the quantum yield of energy donor without the presence of the acceptor, n is the refractive index of the environment, N is Avogadro's number, τ_D is the lifetime of donor without the presence of acceptor, $F_D(\lambda)$ is the fluorescence intensity in the range of l to $\lambda+\Delta\lambda$ whose area is normalized to unity, $\varepsilon_a(\lambda)$ is the extinction coefficient of acceptor at λ, and κ^2 is the orientation of transition dipole of donor relative to acceptor and is normally assumed to be 2/3 in an averaged-random orientation.

The calculation of orientation factor κ^2 is shown in Figure 21. Line r connects transition dipole moment of donor *D* with that of acceptor *A*. *D* and *r* are located on plane P_D whereas *A* and r on plane P_A. ϕ is the angle between P_D and P_A. The angle between D and r is $\theta_D$whereas the angle between *A* and r is θ_A. *A'* is the mirror vector of *A* when it stems from the same point of origin as *D*. *A'* forms an angle of θ_T with *D*.

The mathematical expression for κ^2 is as follows:

$$\kappa^2 = (\cos\theta_T - 3\cos\theta_D\cos\theta_A)^2 \quad (1.22)$$

$$\kappa^2 = (\sin\theta_D\sin\theta_A\cos\phi - 2\cos\theta_D\cos\theta_A)^2 \quad (1.23)$$

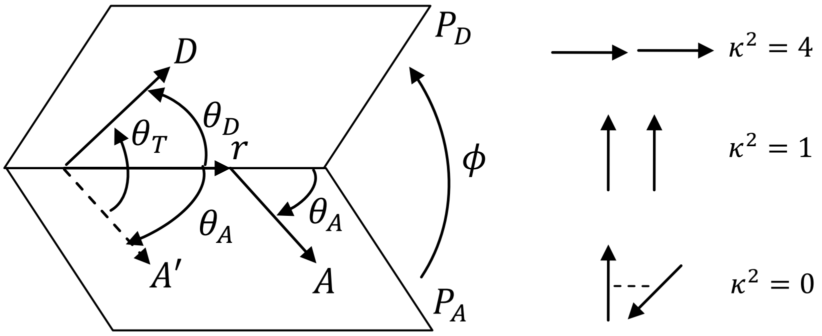

Figure 21: The calculation of orientation factor κ^2 based on transition dipole of donor *D* and acceptor *A*. Using equation 1.22 or 1.23, one arrives at $\kappa^2 = 4$ for collinear and parallel transition dipoles, $\kappa^2 = 1$ for parallel but not collinear dipoles and $\kappa^2 = 0$ when the dipoles are perpendicular to each other.

It is helpful to introduce another parameter $J(\lambda)$ which is defined as the overlap integral between the emission spectrum of donor (with normalized area to unity) and the extinction coefficient of the acceptor. The mathematical expression of overlap integral is

$$J(\lambda) = \int_0^\infty F_D(\lambda)\epsilon_A(\lambda)\lambda^4 d\lambda \quad \text{.................................} \quad (1.24)$$

Another commonly used parameter is Förster distance R_0 which is defined as the distance when the energy transfer rate is equal to inverse of lifetime of donor without the presence of acceptor. At this distance, half of the molecule relaxes through natural decay rate and the other half is quenched by the energy transfer. Förster distance is mathematically described as:

$$R_0 = \frac{Q_D\kappa^2 9000(\ln 10)}{128\pi^5 N n^4} J(\lambda) = 0.211[\kappa^2 n^{-4} Q_D J(\lambda)]^{1/6} \text{ (in Å)} \quad \text{...........} \quad (1.25)$$

And finally, the energy transfer rate (equation 1.21) can be expressed using a simpler term:

$$k_T(r) = \frac{1}{\tau_D}\left(\frac{R_0}{r}\right)^6 \quad \text{.......................................} \quad (1.26)$$

The efficiency of energy transfer E_r is quantitatively expressed as:

$$E_r = 1 - \frac{\tau_{DA}}{\tau_D} \quad \text{...} \quad (1.27)$$

$$E_r = 1 - \frac{F_{DA}}{F_D} \quad \text{...} \quad (1.28)$$

In equation (1.27), τ_{DA} is the lifetime of donor in the presence of acceptor. When either τ_{DA} or τ_D contains multi-exponential decay component, one should use average lifetime decay instead. In equation (1.28), F_{DA} is the fluorescence intensity of donor in the presence of acceptor. It is important to note that in calculating energy transfer efficiency, one should use the un-normalized emission spectrum.

1.7 Single molecule fluorescence microscopy

Single molecule fluorescence microscopy represents the ultimate analytical measurement as it only studies one molecule at one time. It is routinely achieved by combining small volume detection (~1 femto liter) and dilute concentration (~10^{-9}-10^{-10} M). The main advantage of this technique is to avoid averaging which is often encountered in ensemble level measurement. This advantage is illustrated in a system of molecule beacon (Figure 22). The fluorescent of the fluorophore is observed when the beacon is in open state and quenched when it is in closed state. The difference in open and closed state can be clearly seen in the fluorescence spectrum of each single molecule. The rate at which fluorescence is quenched or restored can then be correlated with the equilibrium between open and closed state. In contrast, in an ensemble fluorescence measurement whereby 50% of the beacons are open and 50% are closed, the fluorescence spectrum will not reveal much difference between open and closed state of molecular beacon.

Single molecule fluorescence microscopy has been used in biochemical field, for examples, to obtain the kinetics of cholesterol oxidase,[92] ATPase,[93] chaperonin protein[94] and to study the structural of Holliday junction in nucleic acid.[95] In this work, single molecule fluorescence microscopy was performed using a confocal fluorescence microscope (Micro Time 200, Pico Quant). The setup is depicted in Figure 23.

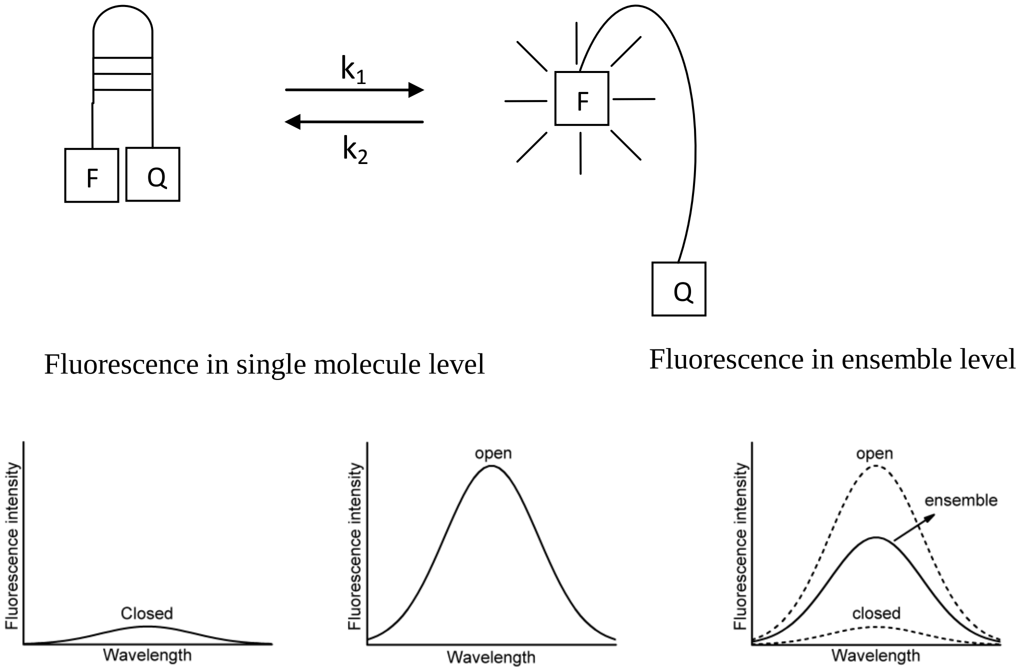
F
Q
k_1
k_2
F
Q
Fluorescence in single molecule level
Fluorescence in ensemble level
Fluorescence intensity
Closed
Wavelength
Fluorescence intensity
open
Wavelength
Fluorescence intensity
open
ensemble
closed
Wavelength

Figure 22: Fluorescence in single molecule level avoids signal averaging which often occurs in ensemble level measurement. F = fluorophore, Q = quencher.

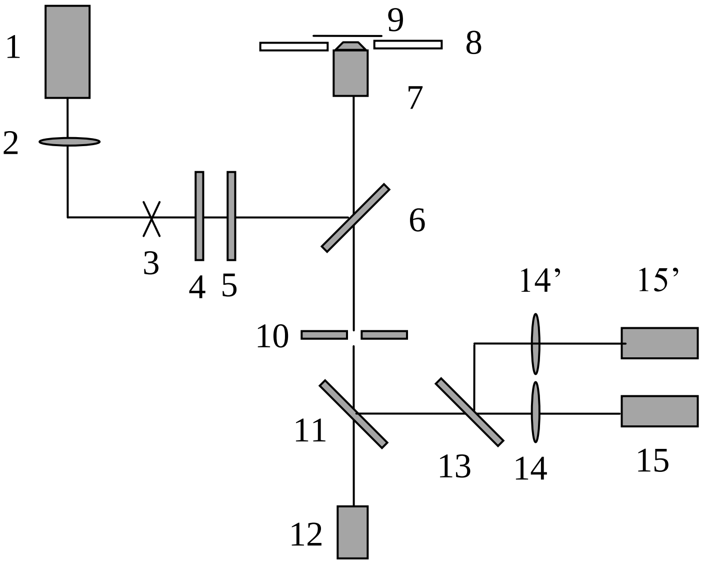

Figure 23: Time-resolved single molecule fluorescence microscopy set up. 1: laser source. 2: excitation filter. 3: shutter. 4: half-wave plate. 5: quarter-wave plate. 6: dichroic mirror. 7: objective lens. 8: piezo stage. 9: glass cover slip sample. 10: pinhole. 11 and 13: beam splitter. 12: charge coupled device (CCD) equipped with monochromator. 15 and 15’: emission filter. 16 and 16’: single photon avalanche diode (SPAD).

Excitation light from pulsed diode laser source is first filtered with an excitation filter. It passes through a shutter and then circularly polarized using a half wave plate and a quarter-wave plate. The light gets reflected by the dichroic mirror and excites the sample placed above the piezo stage. The emission light passes through the dichroic mirror. The out of focus light is rejected through the use of a pinhole. The emitted light can go through the beam splitter and is detected by charged coupled device (CCD) for spectrum analysis or it can be reflected by the beam splitter, passed through another beam splitter and emission filter and is finally detected by single photon avalanche diode (SPAD) for a photon counting analysis.

The resolution of single molecule fluorescence microscopy is determined by the diffraction limited spot *d*:

$$d \cong \frac{1.22\lambda}{NA} \quad \text{...} \quad (1.29)$$

Here, λ is the excitation wavelength and *NA* is the numerical aperture of the objective lens (*NA* = 1.4 for oil based objective lens). In this technique, each single molecule will appear as a bright spot with diameter *d*. Furthermore, this technique cannot distinguish 2 molecules when the distance between them is smaller than *d*. For 470 nm and 635 nm laser, the value of *d* will be 410 and 553 nm, respectively. An example of single molecule fluorescence microscopy image is given in Figure 24.

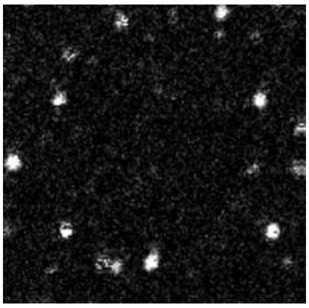

Figure 24: Image of single dye (ATTO547N) molecule represented as bright spots in a 10 µm ×10 µm area.

1.8 Outline of this thesis

This thesis is divided into 5 parts.

Chapter 1 contains the introduction and review of Raman scattering, the role of charge transfer in electrical device of OLED and capacitor, the influence of charge and energy transfer in the fluorescence of conjugated polymer and set up of single molecule fluorescence microscopy.

Chapter 2 investigates the mechanism of charge transfer in enhancing Raman spectra of nitrothiophenol isomers adsorbed onto TiO_2. Charge transfer from molecule to TiO_2 was deduced from the change in absorption spectra and from computational modeling.

Chapter 3 shows how short circuit in a capacitor-like device gave rise to artificial fluorescence modulation when the device was connected to alternating current. This was caused by the deformation of the device as evidenced from AFM image.

Chapter 4 combines the Raman spectroscopy technique with OLED device. Raman spectrum of PEDOT-PSS was affected by injection of hole from ITO. This was correlated with the change in the absorption spectrum of PEDOT:PSS in electrochemical environment.

Chapter 5 studies the influence of charge transfer on electric field-induced fluorescence modulation of MEH-PPV nanoparticle in a capacitor-like device. Energy transfer to from MEH-PPV to TPP was found to lower the degree of modulation.

1.9 References

(1) Siebert, F.; Hildebrandt, P. (2008) *Vibrational Spectroscopy in Life Science*. Weinheim: WILEY-VCH Verlag GmbH &Co. KGaA.Pp 28-29.

(2) Wustholz, K. L.; Brosseau, C. L.; Casadio, F.; Van Duyne, R. P. *Phys. Chem. Chem. Phys.* **2009**, *11*, 7350.

(3) Fleischmann, M. P.; Hendra, P. J.; Mcquillan, A. J. *Chem. Phys. Lett.* **1974**, *26*, 163.

(4) Jeanmaire, D. L.; Van Duyne, R. P. *J. Electroanal. Chem.* **1977**, *84*, 1.

(5) Albrecht, M. G.; Creighton, J. A. *J. Am. Chem. Soc.* **1977**, *99*, 5215.

(6) Etchegoin, P.G.; Lacharmoise, P. D.; Le Ru, E. C. *Anal. Chem.* **2009**, *81*, 682.

(7) Wustholz, K. L.; Brosseau, C. L.; Casadio, F.; Van Duyne, R. P. *Phys. Chem. Chem. Phys.* **2009**, *11*, 7350.

(8) Pieczonka, N. P. W.; Aroca, R. F. *Chem. Soc. Rev.* **2008**, *37*, 946.

(9) Khambampati, P.; Child, C. M.; Foster, M. C.; Campion, A. *J. Chem. Phys.* **1998**, *108*, 5013.

(10) Campion, A.; Kambhampati, P. *Chem. Soc. Rev.* **1998**, *27*, 241.

(11) Lombardi, J. R.; Birke, R. L.; Lu, T.; Xu, J. *J. Chem. Phys.* **1986**, *84*, 4174.

(12) Stiles, P. L.; Dieringer, J. A.; Shah, N. C.; Van Duyne, R. P. *Annu. Rev. Anal. Chem.* **2008**, *1*, 601.

(13) Moskovits, M. *J. Raman Spectrosc.* **2005**, *36*, 485.

(14) Dieringer, J. A.; McFarland, A. D.; Shah, N. C.; Stuart, D. A.; Whitney, A. C.; Yonzon, C. R.; Young, M. A.; Zhang, X.; Van Duyne, R. P. *Faraday Discuss.* **2006**, *132*, 9.

(15) Kennedy, B. J.; Spaeth, S.; Dickey, M.; Carron, K. T. *J. Phys. Chem. B* **1999**, *103*, 3640.

(16) Moskovitz, M. *J. Chem Phys.* **1982**, *77*, 4408.

(17) Alvarez-Puebla, R. A.; Dos Santos Jr, D. S.; Aroca, R. F *Analyst* **2004**, *129*, 1251.

(18) Erol, M.; Han, Y.; Stanley, S. K.; Stafford, C. M.; Du, H.; Sukhishvili, S.; *J. Am. Chem. Soc.* **2009**, *131*, 7480

(19) Michota, A.; Bukowska, J. *J. Raman Spectrosc.* **2003**, *34*, 21.

(20) Yoon, H. J.; Park, J. S.; Yoon, S. *Langmuir* **2009**, *25*, 12475.

(21) Xu, H.; Aizpurua, J.; Käll, M.; Apell, P. *Phys. Rev. E* **2000**, *62*, 4318.

(22) Blackie, E. J.; Le Ru, E. C.; Etchegoin P. G. *J. Am. Chem. Soc.* **2009**, *131*, 14466.

(23) Camden, J. P.; Dieringer, J. A.; Wang, Y.; Masiello, D. J.; Marks, L .D.; Shatz, G. C.; Van Duyne, R. P. *J. Am. Chem. Soc.* **2008**, *130*, 12616.

(24) Moskovits, M. *Rev. Mod. Phys.* **1985**, *57*, 783.

(25) Furtak, T. E.; Macomber, S. H. *Chem. Phys. Lett.* **1983**, *95*, 328.

(26) Hurst, S. J.; Fry, H. C.; Gosztola, D. J.; Rajh, T. *J. Phys. Chem. C* **2011**, *115*, 620.

(27) Wang, Y.; Ruan, W.; Zhang, J.; Yang, B.; Xu, W.; Zhao, B.; Lombardi, J. R. *J. Raman Spectrosc.* **2009**, *40*, 1072.

(28) Kumar, K.; Carey, P. R. *J. Chem. Phys.* **1975**, *63*, 3697.

(29) Osawa, M.; Matsuda, N.; Yoshii, K.; Uchida, I. *J. Phys. Chem.* **1994**, *98*, 12702.

(30) Lombardi, J. R.; Birke, R. L.; Lu, T.; Xu, J. *J. Chem. Phys.* **1986**, *84*, 4174.

(31) Lombardi, J. R.; Birke, R. L. *Acc. Chem. Res.* **2009**, *42*, 734.

(32) Yang, L.; Jiang, X.; Ruan, W.; Zhao, B.; Xu, W.; Lombardi, J. R. *J. Phys. Chem. C* **2008**, *112*, 20095.

(33) Kneipp, K.; Kneipp, H.; Itzkan, I.; Dasari, R. R.; Feld, M. S. *Chem. Phys.* **1999**, *247*, 155.

(34) Kamisuki, T.; Dudev, T.; Hirose, C. *J. Phys. Chem.* **1991**, *95*, 5845.

(35) Dudev, T.; Kamisuki, T.; Akamatsu, N.; Hirose, C. *J. Phys. Chem.* **1991**, *95*, 4999.

(36) Kamisuki, T.; Hirose, C. *J. Phys. Chem.* **1991**, *95*, 5003.

(37) Kamisuki, T.; Hirose, C. *J. Raman Spectrosc.* **1995**, *26*, 93.

(38) Nestor, J.; Spiro, T. G.; Klauminzer, G. K. *PNAS* **1976**, *73*, 3329.

(39) Dutta, K. P.; Dlinger, R.; Spiro, T. G. *J. Chem. Phys.* **1980**, *73*, 3580.

(40) Zou, K.; Hong, X.; Zhu, J. *Phys. Rev. B* **2011**, *84*, 085408.

(41) Enright, B.; Fitzmaurice D. *J. Phys. Chem*. **1996**, *100*, 1027.

(42) Wetzelaer, G. –J. A. H.; Kuik, M.; Olivier, Y.; Lemaur, V.; Cornil, J.; Fabiano, S.; Loi, M. A.; Blom, P. W. M. *Phys. Rev. B* **2012**, *86*, 165203.

(43) Xu, H.; Jiang, Y.; Li, J.; Ong, B. S.; Shuai, Z.; Xu, J.; Zhao, N. *J. Phys. Chem. C* **2013**, *117*, 6835.

(44) Pope, M.; Kallman, H. P.; Magnante, P. *J. Chem. Phys.* **2002**, *38*, 2042.

(45) Tang, C. W.; VanSlyke, S. A. *Appl. Phys. Lett.* **1987**, *51*, 913.

(46) Burroughes, J. H.; Bradley, D. D. C.; Brown, A. R.; Marks, R. N.; Mackay, K.; Friend, R. H.; Burns, P. L.; Holmes, A. B. *Nature* **1990**, *347*, 539.

(47) Grem, G.; Leditzky, G.; Ulrich, B.; Leising, G. *Adv. Mater.* **1992**, *4*, 36.

(48) Burn, P. L.; Holmes, A. B.; Kraft, A.; Bradley, D. D. C.; Brown, A. R.; Friend, R. H.; Gymer, R. W. *Nature* **1992**, *356*, 47.

(49) Gustafsson, G.; Cao, Y.; Treacy, G. M.; Klavetter, F.; Colaneri, N.; Heeger, A. K. *Nature* **1992**, *357*, 477.

(50) Braun, D.; Heeger, A. J. *Appl. Phys. Lett.* **1991**, *58*, 1982.

(51) Stössel, M.; Staudigel, J.; Steuber, F.; Simmerer, J.; Winnacker, A. *Appl. Phys. A* **1999**, *68*, 387.

(52) Andersson, A.; Johansson, N.; Bröms, P.; Yu, N.; Lupo, D.; Salaneck, W. R. *Adv. Mater.* **1998**, *10*, 859.

(53) Jang, J. W.; Oh, D. K.; Lee, C. H.; Lee, C. E.; Lee, D. W.; Jin, J. –II *J. Appl. Phys.* **2000**, *87*, 3183.

(54) Niu, Y. –H.; Liu, M. S.; Ka, J. –W.; Jen, A. K. –Y. *Appl. Phys. Lett.* **2006**, *88*, 093505.

(55) Ren, X.; Li, J.; Holmes, R. J.; Djurovich, P. I.; Forrest, S. R.; Thompson, M. E. *Chem. Mater.* **2004**, *16*, 4743.

(56) Yang, Y.; Pei, Q.; Heeger, A. J. *Appl. Phys. Lett.* **1996**, *79*, 934.

(57) Yim C.; McEvoy, N.; Kim, H. –Y.; Rezvani, E.; Duesberg, G. S. *ACS Appl. Mater. Interfaces* **2013**, *5*, 6951.

(58) Kumar, R.; Khare, N.; Bhalla, G. L.Kamalasanan, M. N. *Thin Solid Films* **2010**, *518*, e61.

(59) Vietmeyer, F.; Tchelidze, T.; Tsou, V.; Janko, B.; Kuno, M. *ACS Nano* **2012**, *6*, 9133.

(60) Teguh, J. S.; Kurniawan, M.; Wu, X.; Sum, T. Z.; Yeow, E. K. L. *Phys. Chem. Chem. Phys.* **2013**, *15*, 90.

(61) Gesquiere, A.; Park, S. –J.; Barbara, P. F. *J. Phys. Chem. B* **2004**, *108*, 10301.

(62) Hu, Z.; Gesquiere, A. J. *J. Am. Chem. Soc.* **2011**, *133*, 20850.

(63) Hania, P. R.; Scheblykin, I. G. *Chem. Phys. Lett.* **2005**, *414*, 127.

(64) Hania, P. R.; Thomsson, D.; Scheblykin, I. G. *J. Phys. Chem. B* **2006**, *110*, 25895.

(65) Barbara, P. F.; Gesquiere, A. J.; Park, S. –J.; Lee, Y. J. *Acc. Chem. Res.* **2005**, *38*, 602.

(66) Yu, Z.; Barbara, P. F. *J. Phys. Chem. B* **2004**, *108*, 11321.

(67) Burrows, H. D.; Seixas de Melo, J.; Serpa, C.; Arnau, L. G.; da G Miguel, M.; Monkman, A. P.; Hamblett, I.; Navaratnam, S. *Chem. Phys.* **2002**, *285*, 3.

(68) Gesquiere, A. J.; Lee, Y. J.; Barbara, P. F. *J. Phys. Chem. B* **2005**, *109*, 12366.

(69) Gesquiere, A. J.; Park, S. –J.; Barbara, P. F. *J. Am. Chem. Soc.* **2005**, *127*, 9556.

(70) Hu, Z.; Gesquiere, A. J. *J. Am. Chem. Soc.* **2011**, *133*, 20850.

(71) Morgado, J.; Cacialli, F.; Iqbal, R.; Moratti, S. C.; Holmes, A. B.; Yahioglu, G.; Milgrom, L. R.; Friend, R. H. *J. Mater. Chem.* **2011**, *11*, 278.

(72) Wu, C.; Zheng, Y.; Szymanski, C.; McNeill, J. *J. Phys. Chem. C* **2008**,*112*, 1772.

(73) Landfester, K.; Montenegro, R.; Scherf, U.; Güntner, R.; Asawapirom, U.; Patil, S.; Neher, D.; Kietzke, T. *Adv. Mater.* **2002**, *14*, 651.

(74) Piok, T.; Gamerith, S.; Gadarmaier, C.; Plank, H.; P. Wenzl, F.; Patil, S.; Montenegro, R.; Kietzke, T.; Neher, D.; Scherf, U.; Landfester, K.; List, E. J. W. *Adv. Mater.* **2003**, *15*, 800.

(75) Wu, C.; Syzmanski, C.; McNeill, J. *Langmuir* **2006**, *22*, 2956.

(76) Kietzke, T.; Neher, D.; Kumke, M.; Montenegro, R.; Landfester, K.; Scherf. U. *Macromolecules* **2004**, *37*, 4882.

(77) Rahim, N. A. A.; McDaniel, W.; Bardon, K.; Srinivasan, S.; Vickerman, V.; So, P. T. C.; Moon, J. H. *Adv. Mater.* **2009**, *21*, 3492.

(78) Derfus, A. M.; Chan, W. C. W.; Bhatia, S. N. *Nano Lett.* **2004**, *4*, 11.

(79) Wu, C.; Bull, B.; Christensen, K.; McNeill, J. *Angew. Chem. Int. Ed.* **2009**, *48*, 2741.

(80) Shen, X.; Li, L.; Wu, H.; Yao, S. Q.; Xu, Q. –H. *Nanoscale* **2011**, *3*, 5140.

(81) Schwartz, B. J. *Annu. Rev. Phys. Chem.* **2003**, *54*, 141.

(82) Syzmanski, C.; Wu, C.; Hooper, J.; Salazar, M. A.; Perdomo, A.; Dukes, A.; McNeill, J. *J. Phys. Chem. B* **2005**, *109*, 8543.

(83) Pecher, J.; Mecking, S. *Chem. Rev.* **2010**, *110*, 6260.

(84) Gouterman, M. *J. Chem. Phys.* **1959**, *30*, 1139.

(85) Ghosh, M.; Nah, S.; Hajra, A.; Sinha, S. *J. Lumin.* **2013**, *141*, 87.

(86) Wiglusz, Legendziewicz, J.; Graczyk, A.; Radzki, S.; Gawryszewska, Sokolnicki, J. *J. Alloy Compd.* **2004**, *380*, 396.

(87) Wu, C.; Zheng, Y.; Szymanski, C.; McNeill, J. *J. Phys. Chem. C* **2008**, *112*, 1772.

(88) Stryer, L. *Annu. Rev. Biochem.* **1978**, *47*, 819.

(89) Fung, B. K. K.; Stryer, L. *Biochemistry* **1978**, *17*, 5241.

(90) Tsuji, A.; Koshimoto, H.; Sato, Y.; Hirano, M.; Sei-Iida, Y.; Kondo, S.; Ishibashi, K. *Biophys. J.* **2000**, *78*, 3260.

(91) Sato, M.; Ozawa, T.; Inukai, K.; Asano, T.; Umezawa, Y. *Nature Biotechnol.* **2002**, *20*, 287.

(92) Lu, H. P.; Xun, L.; Xie, S. *Science* **1998**, *282*, 1877.

(93) Tokunaga, M.; Kitamura, K.; Saito, K.; Iwane, A. H.; Yanagida, T. *Biochem. Biophys. Res. Commun.* **1997**, *235*, 47.

(94) Taguchi, H.; Ueno, T.; Tadakuma, H.; Yoshida, M.; Funatsu, T. *Nature Biotechnol.* **2001**, *19*, 861.

(95) McKinney, S. E.; Déclais, A. -C.; Lilley, D. M. J.; Ha, T. *Nature Struct. Biol.* **2003**, *10*, 93.

CHAPTER 2

SURFACE ENHANCED RAMAN SPECTROSCOPY (SERS) OF NITROTHIOPHENOL ISOMERS CHEMISORBED ON TIO$_2$

This chapter is adapted from “Surface Enhanced Raman Spectroscopy (SERS) of Nitrothiophenol Isomers Chemisorbed on TiO$_2$, Teguh, J. S.; Fang, L.; Xing, B.; Yeow, E. K. L. *Chem. Asian J.* **2012**, *7*, 975-981.”

2.1 Introduction

Surface-enhanced Raman scattering (SERS) was discovered in 1974 and has since been an important analytical tool in several applications including biological sensing,[1,2] trace analysis,[3] and catalysis.[4] There are primarily two mechanisms that are responsible for the SERS effect. The first is the electromagnetic enhancement (EE) mechanism that occurs in probe molecules deposited on roughened noble metal (*e.g*., silver or gold) surfaces.[5] In this case, the incident light is used to excite the surface plasmon of a metallic substrate which creates a strong local electric field that is capable of interacting with the molecule and enhancing the Raman signal. A significant amount of research effort has been dedicated to investigate the EE mechanism since its enhancement factor is large (10^6 - 10^{14}) and easily detectable.[6-8] The second mechanism is the chemical enhancement (CE) which is linked to EE for probe molecules chemisorbed onto the surface of a metal (*e.g.* silver nanostructure). In the CE mechanism for a molecule on Ag, an optically driven charge-transfer (CT) transition from the highest occupied molecular orbital (HOMO) of the probe to the Fermi level of the metal or from the Fermi level to the lowest unoccupied molecular orbital (LUMO) of the probe results in a modest enhancement factor of ~10^2.[5,9-11] In order to fully understand the exact nature of the enhanced Raman signal of a molecule adsorbed on a metal surface, it is important to elucidate the roles of both EE and CE.[12]

An important factor that controls the working efficiency of a titanium oxide-based dye-sensitized solar cell is the charge-separation process between the dye molecule and *n*-type semiconductor. The CT dynamics from molecule to TiO_2 has been extensively studied using ultrafast spectroscopy[13] and single-molecule detection techniques.[14] Recently, Raman spectroscopy has been utilized to examine the interactions between molecules and metal oxides with the aim of understanding the driving force behind the observed SERS effect.[15-18] In particular, several models have been proposed to explain the enhanced Raman signal for a probe molecule adsorbed onto a TiO_2 surface, including a TiO_2-to-molecule CT,[15] and a molecule-to-TiO_2 CT.[16,17]

SERS is often used to predict the configuration of isomers adsorbed on metallic surfaces.[19-22] Using the EE surface selection rules, in which vibrational modes with transition dipole moments arranged normal to the metal surface are preferentially enhanced,[23,24] the arrangement of the molecule with respect to the substrate can be determined. So far, there are no reports in the literature on the use of SERS to study the CE effect for a family of isomers on TiO_2. In this work, the effect of CE on enhancing the Raman signal of *ortho*-nitrothiophenol (*o*-NTP), *meta*-nitrothiophenol (*m*-NTP) and *para*-nitrothiophenol (*p*-NTP) chemisorbed on the surface of TiO_2 nanocrystals will be investigated (Figure 1). The relationship between the electron withdrawing ability of the nitro group in each isomer and the CT process will be elucidated using both experimental SERS and density functional theory (DFT) calculations.

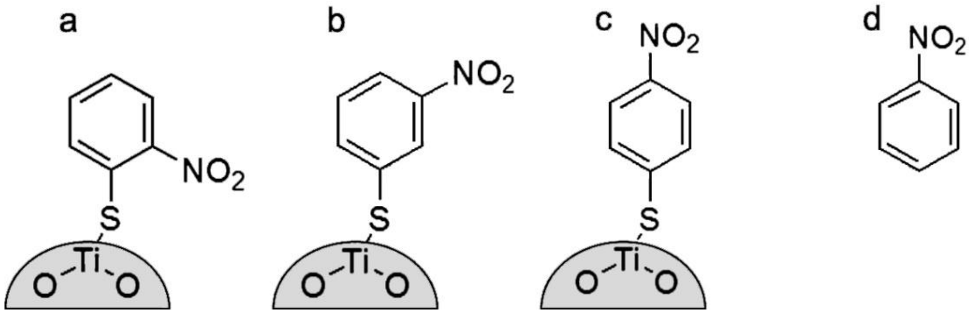

Figure 1: Schematic of the adsorption of *o*-NTP (a), *m*-NTP (b) and *p*-NTP (c) on the surface of TiO_2 *via* a S-Ti bond. The nitrobenzene (d) does not undergo chemisorption on TiO_2.

2.2 Experimental section

2.2.1 Materials

2-nitrobenzenesulfonyl chloride, 3-nitrobenzenesulfonyl chloride, titanium isopropoxide (99.999%), nitrobenzene, *p*-nitrothiophenol (tech, ≥80% RT, *p*-NTP), Ag nanopowder (<100 nm size, 99.5% metals basis) and tetrahydrofuran (spectrophotometric grade, THF) were purchased from Sigma Aldrich. Isopropanol and hydrochloric acid (37%, HCl) were purchased from Tedia and Panreac, respectively.

o-nitrothiophenol (*o*-NTP) was synthesized from 2-nitrobenzenesulfonyl chloride according to a reported method.[25] Briefly, a solution of arylsulfonyl chloride (10 mmol) in anhydride toluene (30 mL) in a round-bottom flask was cooled to 0^oC under ice bath, and Ph_3P (45 mmol) was added within 5 minutes. The reaction was stirred for 20 min at 0°C. H_2O (20 mL) was added and the mixture was stirred for 10 min. The aqueous layer was discarded and the organic layer was extracted with 2M NaOH (30 mL). The alkaline aqueous extract was washed with toluene (2 × 20 mL), acidified with 2M HCl and extracted with CH_2Cl_2 (2 × 20 mL). The organic layer was dried over Na_2SO_4 and condensed, purified with flash chromatography ethyl acetate/hexane (1:20) to afford *o*-NTP as a light yellow solid.[26] ^1H NMR (400MHz, $CDCl_3$) δ: 4.03 (s, 1H), 7.28-7.31 (m, 1H), 7.44-7.45 (m, 2H), 8.25-8.27 ppm (d, *J*=8.0 Hz, 1H). Mass spectrometry (EI): 155 M^+ observed.

m-nitrothiophenol (*m*-NTP) as a light yellow oil was synthesized from 3-nitrobenzenesulfonyl chloride according to the same method described above. ^1H NMR (400MHz, CDCl3) δ: 3.74 (s, 1H), 7.41 (t, *J*=8.0 Hz, 1H), 7.55-7.58 (m, 1H), 7.97-8.00 (m, 1H), 8.12 ppm (t, *J*=2.0 Hz 1H); ^{13}C NMR (100 MHz, CDCl3) 120.5, 123.5, 129.8, 134.0, 134.7, 148.5 ppm. Mass spectrometry (EI): 155 M^+ observed.

TiO_2 nanocrystal in the anatase phase was prepared according to a method described previously.[14,27] Briefly, titanium isopropoxide (0.4 mL) was added to isopropanol (2 mL). The mixture was then added slowly to a solution consisting of water (20 mL) and 37% HCl (200 μL) under vigorous stirring. The white colloidal solution was then stirred for 24 h and dried in an oven (90 ^oC). The resulting white solid was subsequently heated at 450 ^oC for 4 hours to yield TiO_2 anatase crystals.

2.2.2 Characterization of TiO_2

The diameter of the TiO_2 nanocrystal was determined to be *ca*. 12 nm using a TEM (JEM-1400, JEOL, Figure 2). The Raman spectrum of neat TiO_2 was recorded using a Raman microscope (LabRAM HR, Horiba). The spectrum (Figure 3) displays peaks at 143 cm^{-1}, 196 cm^{-1}, 396 cm^{-1}, 516 cm^{-1} and 641 cm^{-1} which are attributed to the E_g, E_g, B_{1g}, A_{1g}, and E_g stretching modes of anatase TiO_2.[28] The BET (Bruanuer, Emmett, Teller) surface area of the TiO_2 nanocrystal was obtained from the nitrogen adsorption/desorption isotherms measured using a static volumetric instrument (Autosorb-6b, Quanta Chrome).The outgas temperature was set at 200 ^oC and outgas time at 3 h.

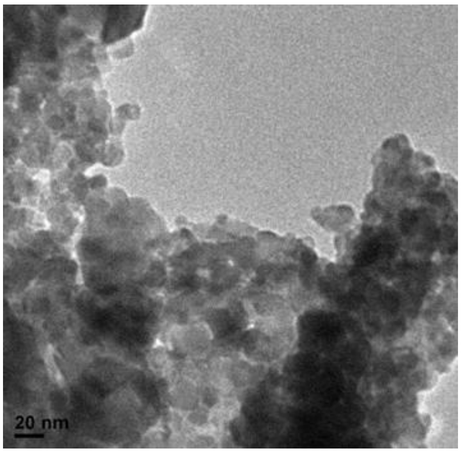

Figure 2: TEM image of TiO_2 nanocrystals.

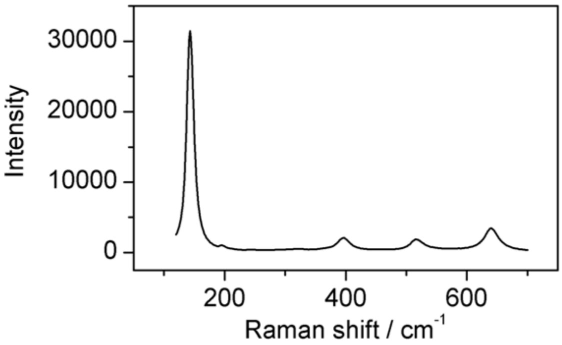

Figure 3: Raman spectrum of TiO_2 anatase crystal obtained using λ_{ex} = 633 nm. The laser power used was 850 μW and the integration time was 5s.

2.2.3 UV-Vis absorption and cyclic voltammetry

The absorption spectra of TiO_2 and NTP bound to TiO_2 were measured using an absorption spectrometer (Cary 100, Varian) equipped with a diffuse reflectance accessory.

Cyclic voltammetry measurement was carried out using a potentiostat (Metrohm Autolab PGSTAT302N) equipped with a 5 mL three-electrode cell and glass carbon as working electrode. Oxidation potentials of *m*-NTP (2.6 mM) and *p*-NTP (2 mM) in THF were determined in room temperature with a 0.2 M tetrabutylammonium hexafluoro-phosphate as electrolyte. Half wave potential of ferrocene was obtained under similar conditions. The energy of HOMO was estimated using the formula $E_{HOMO} = -e(E_{ox} + 4.8)$,[29] where E_{ox} is the oxidation potential of NTP.

2.2.4 Elemental analysis and Raman spectroscopy

The wt% of nitrogen on the surface of modified TiO_2 was determined using an elemental analyzer (Euro3000, EuroVector) with temperature of the front furnace set at 1020 °C. The delay time and run time for each sample were fixed at 8 s and 320 s, respectively. To ensure accuracy, at least 1 mg of sample was measured. Raman spectra of surface-modified TiO_2 deposited onto cleaned glass cover-slips were measured using a Raman microscope (LabRAM HR, Horiba). The excitation wavelengths of the irradiating light are 488 nm (Stellar-Pro-L Select 300 Ar laser, Modu-Laser), 633 nm (He-Ne laser, Melles Griot) and 785 nm (diode laser, Sacher Lasertechnik), and the Raman signals were collected using a 100× (NA = 0.9) objective lens. Raman spectra of NTP isomers in THF were acquired using the same excitation wavelengths and laser power. The detector used is an electron multiplying CCD (EMCCD) (DU970N, ANDOR) which has a classical front illuminated chip and does not show Etaloning effect. All spectra were corrected for fluorescence background using a polynomial baseline correction function (8 degree) found in the Raman analysis software LabSPEC 5 (Horiba Jobin Yvon) (Figure4).

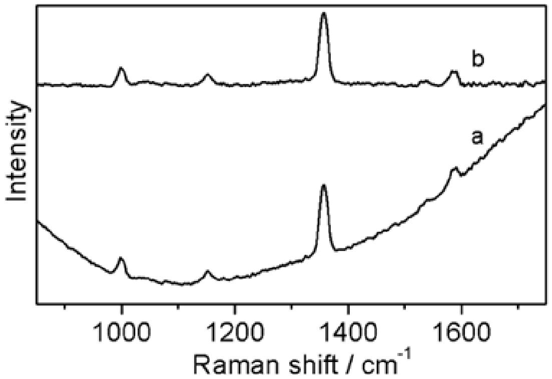

Figure 4: SERS spectrum of *m*-NTP chemisorbed onto TiO_2 before (a) and after (b) fluorescence background correction. I_{ex} = 488 nm. The baseline feature below 1000 cm^{-1} Raman shift is due to the TiO_2 broad stretching peak.

2.2.5 Density Functional Theory (DFT) calculation

Density functional theory-B3LYP (DFT-B3LYP) calculation in Gaussian 09[30] was carried out to simulate the Raman spectrum for each of the NTP isomer. The basis set used was 6-311G (d,p). DFT-B3LYP calculation with 6-311G+ (d,p) basis was conducted to obtain the optimized geometry and molecular orbital profiles of *p*-NTP and *m*-NTP bound to a $(TiO_2)_2$ cluster. Hydrogen atom was added to $(TiO_2)_2$ to balance the overall charge.

2.3 Result and discussion

2.3.1 Surface Enhanced Raman Spectrum (SERS)

Elemental analysis (EA) is employed to characterize the adsorption of NTP isomers and nitrobenzene on TiO_2 nanocrystals. In this case, the sample is prepared by first incubating TiO_2 (4 mg) in a solution made up of either a NTP isomer (1 mM) or nitrobenzene (10 mM) in tetrahydrofuran (THF) solvent. The TiO_2 is then rinsed with THF to remove any unadsorbed probe molecules. The wt% nitrogen on the surface of TiO_2, arising from N in the nitro group of the adsorbate, is determined from EA to be 0.131%, 0.223% and 0.257% for *o*-NTP, *m*-NTP and *p*-NTP, respectively. Even though the accuracy of EA is ± 0.5% and it seems large as compared to the measured percentage of nitrogen, we are not aware of other measurement technique to quantify the amount of molecule adsorbed onto TiO_2. It turned out that the calculation of enhancement factor based on the number of molecule detected by EA falls within reasonable range (as shown below). On the other hand, the wt% nitrogen found on TiO_2 treated with nitrobenzene is negligibly small. This indicates that the NTP isomers are adsorbed onto the surface of TiO_2 whereas nitrobenzene does not display any significant binding with the semiconductor after rinsing with THF (*i.e.*, nitrobenzene has been washed off). Due to the absence of adsorption of nitrobenzene on TiO_2, the binding between the nitro group and the metal oxide can be ignored and the association between NTP and TiO_2 is likely to be a chemical adsorption *via* the formation of a S-Ti bond as illustrated in Figure 1. The formation of S-Ti bond is proposed to be similar to the formation of S-Au when thiol adsorbs and forms a self-assembled-monolayer on Au film.[31] Even though the nature of S-Au bond is still a matter of ongoing investigation, the currently accepted model involves the deprotonation of sulfhydryl group, creating a thiyl radical ($RS^{\bullet}$) which will then form S-Au bond.[32] We believe that a similar mechanism occurs in our system. This proposal follows the model of the previous studies of SERS using semiconductor substrate, *e.g.* formation of S-Ti or S-Mo bond when 4-mercaptobenzoic acid adsorbs onto TiO_2 or MoO_3, respectively.[15,33] Furthermore, the SH stretching band of neat nitrothiophenol between 2500 cm^{-1} to 2600 cm^{-1} vanishes when the molecule is chemisorbed onto TiO_2; indicating the disappearance of the SH stretching mode when the thiol group is covalently attached onto the metal oxide surface (Figure 5).

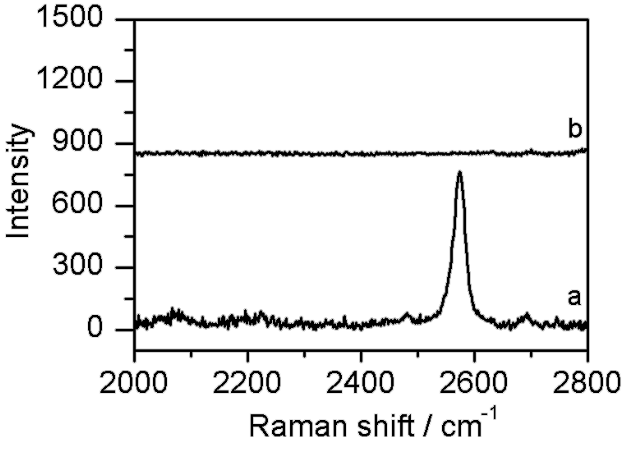

Figure 5: Raman spectrum of *m*-NTP excited with 633 nm light with the position of the SH stretching mode at 2574 cm^{-1} (a). Upon adsorption onto TiO_2, the SH stretching signal at 2574 cm^{-1} disappears due to the formation of a covalent bond with the metal oxide (b). The SERS spectrum of *m*-NTP adsorbed onto TiO_2 has been magnified 4 times.

The Raman spectra of neat *o*-NTP (powder), *m*-NTP (oil) and *p*-NTP (powder) obtained using an excitation wavelength (λ_{ex}) of 633 nm is presented in Figure 6. The intense Raman peak at 1338 cm^{-1}, 1348 cm^{-1} and 1333 cm^{-1} for *o*-NTP, *m*-NTP and *p*-NTP, respectively, corresponds to the NO_2 symmetrical stretching mode ($\nu_s(NO_2)$).[34,35] DFT calculations were performed to simulate the theoretical Raman spectra (Figure 6) which were subsequently used to assign the peaks observed in the experimental spectra. The frequencies and the corresponding vibrational assignments are summarized in Table 1(a)-(c). The calculated Raman spectra are consistently shifted to higher wavenumbers relative to the experimental. Calculated Raman spectra are based on single nitrothiophenol compound isolated in vacuum whereas experimental Raman spectra is based on nitrothiophenol compound in powder (for *o*-NTP and *p*-NTP) or oil (*m*-NTP) form. Quite possibly, the intermolecular interaction in powder or oil form causes narrowing in the vibrational energy levels. Hence, experimental Raman spectra shift to lower wavenumber as compared to calculated Raman spectra.

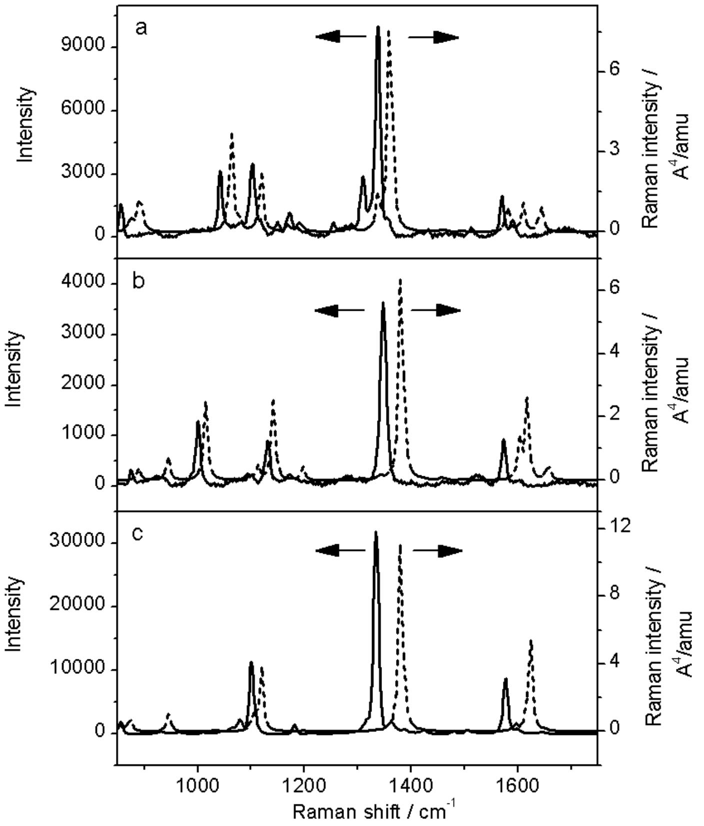

Figure 6: The experimental (solid) and DFT calculated (dash) spectra of neat *o*-NTP (a), *m*-NTP (b) and *p*-NTP (c). The experimental spectra were obtained using I_{ex} = 850 μW and 60 s integration time.

Table 1(a). Major peaks and the respective assignments in the Raman spectrum of *o*-NTP (in cm^{-1})

o-NTP (λ_{ex} = 633nm)[1]	*o*-NTP DFT-B3LYP 6-311G+ (d,p)[2]	Assignment[2]
1041	1064	CC stretching, SH bending
1102	1120	CS stretching
1310	1337	CC stretching, CH bending
1338	1358	NO_2 symmetrical stretching
-	1582	CC stretching, NO_2 asymmetric stretching, SH bending, CH bending
1569	1610	CC stretching, CH in-plane bending
1591	1645	CC stretching, NO_2 asymmetric stretching, CH bending

[1] From experimental spectrum of neat *o*-NTP obtained using excitation wavelength λ_{ex} = 633 nm (Figure 6a).

[2] From DFT calculations

Table 1(b). Major peaks and the respective assignments in the Raman spectra of *m*-NTP and *m*-NTP adsorbed on TiO_2 (in cm^{-1})

m-NTP (λ_{ex} = 633nm)[1]	*m*-NTP+TiO_2 (λ_{ex} = 633 nm)[2]	*m*-NTP DFT-B3LYP 6-311G+ (d,p)[3]	Assignment[3]
1001	997	1015	CC in plane bending, SH bending (disappears when adsorbed on TiO_2)
1132	1148	1141	in plane bending, CS stretching
1348	1355	1379	NO_2 symmetrical stretching
1573	1584	1617	CC stretching, CH in plane bending

[1] From experimental spectrum of neat *m*-NTP obtained using excitation wavelengthλ_{ex} = 633 nm (Figure 6(b))

[2] From experimental spectrum of *m*-NTP bound to TiO_2 obtained using λ_{ex} = 633 nm (Figure7(a))

[3] From DFT calculations

Table 1(c). Major peaks and the respective assignments in the Raman spectra of *p*-NTP and *p*-NTP adsorbed on TiO_2 (in cm^{-1})

p-NTP (λ_{ex} = 633 nm)[1]	*p*-NTP+TiO_2 (λ_{ex} = 633 nm)[2]	*p*-NTP DFT-B3LYP 6-311G+ (d,p)[3]	Assignment[4]
857	858	853	CH wagging
1101	1106	1106	CCC in plane bending, CS stretching
-	-	1120	CN stretching
1333	1353	1379	NO_2 symmetrical stretching
1577	1591	1624	CC stretching, CH in plane bending

[1] From experimental spectrum of neat *p*-NTP obtained using excitation wavelength λ_{ex} = 633 nm (Figure 6(c))

[2] From experimental spectrum of *p*-NTP bound to TiO_2 obtained using λ_{ex} = 633 nm (Figure 7(b))

[3] From DFT calculations

[4] From reference [35] of main text

Figure 7 shows the Raman spectra of *m*-NTP and *p*-NTP chemisorbed on TiO_2 using λ_{ex} = 633 nm and 488 nm. Upon binding with TiO_2, the $\nu_s(NO_2)$ peaks of *m*-NTP (1355 cm^{-1} and 1356 cm^{-1} for λ_{ex} = 633 and 488 nm, respectively, see Table 1) and *p*-NTP (1353 and 1356 cm^{-1} for λ_{ex} = 633 nm and 488 nm, respectively) are shifted to lower energy as compared to the corresponding neat compounds (Figure 6), indicating that the probe molecules are adsorbed onto TiO_2. In the case of *o*-NTP on TiO_2, strong fluorescence is detected which disallowed discernible Raman peaks to be recorded. It is worth mentioning that Perry *et al*. have also reported that *o*-nitrophenol on Ag nanostructure does not exhibit any detectable Raman signal at λ_{ex}= 633 nm.[21]

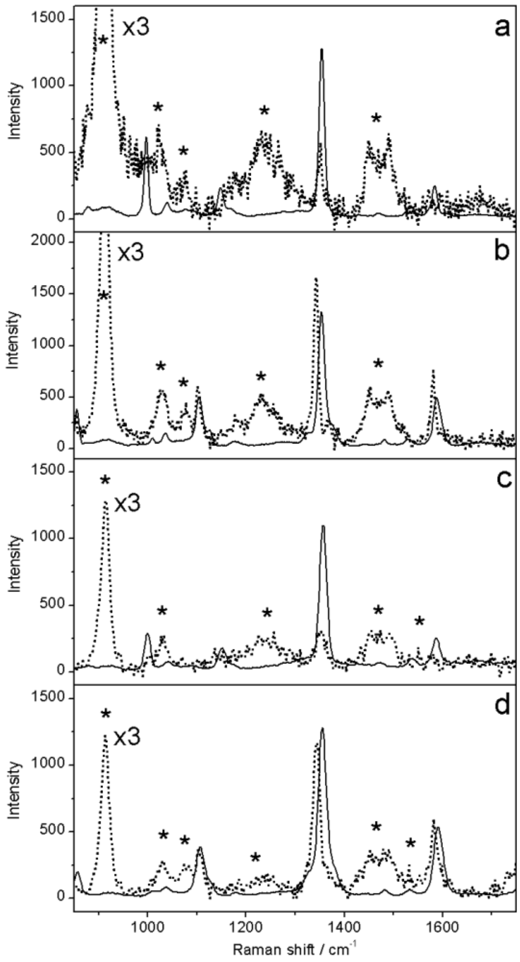

Figure 7: The SERS spectra (solid) of *m*-NTP (a) and *p*-NTP (b) adsorbed on TiO_2 recorded with λ_{ex} = 633 nm. The SERS of *m*-NTP (c) and *p*-NTP (d) adsorbed on TiO_2 recorded with λ_{ex} = 488 nm. The corresponding Raman spectra (dash) of 0.1 M of the neat nitrothiophenol isomer in THF recorded with λ_{ex} = 633 nm (a and b) and λ_{ex} = 488 nm (c and d) (magnified 3 times). The solvent peaks are indicated by *. Fluorescence background has been corrected for λ_{ex} = 488 nm. For λ_{ex} = 633 nm, the spectra were obtained using I_{ex} = 850 μW and 60 s integration time, and for λ_{ex} = 488 nm, I_{ex} = 280 μW and integration time is 30 s.

The Raman spectra of 0.1 M of *m*-NTP and *p*-NTP in THF were also recorded using similar laser power intensities (I_{ex}) employed to obtain the spectra of NTP isomers on TiO_2. The Raman peaks associated with *m*-NTP and *p*-NTP in THF at λ_{ex} = 633 nm (I_{ex} = 850 μW) are given in Figure 7 where it is noted that the intensity of the $\nu_s(NO_2)$ peak at ~1350 cm^{-1} is not affected by the solvent signal. Laser power intensity greater than 280 μW for λ_{ex} = 488 nm was avoided in order to prevent possible photodegradation of NTP on TiO_2. From Figure 7, it is clear that the $\nu_s(NO_2)$ peaks of *m*-NTP and *p*-NTP on TiO_2 are surface-enhanced with respect to the ones seen in THF solution.

The surface of the TiO_2 nanocrystals is not uniformly smooth (Figure 8 shows the raster scanning image) such that the NTP molecules are not homogeneously adsorbed throughout the semiconductor nanoparticles. The concentration of the probe molecules and hence the intensity of the $\nu_s(NO_2)$ peak, therefore, fluctuate with the location of analysis on the TiO_2 surface. Figure 9 shows the distribution of the $\nu_s(NO_2)$ peak intensities for both *m*-NTP and *p*-NTP on TiO_2 at 80 different locations (spots) for λ_{ex} = 633 nm. By fitting the histograms with a Gaussian function, the mean surface-enhanced Raman intensity of the $\nu_s(NO_2)$ peak (I_{SERS}) for the various NTP isomers on the metal oxide is obtained. For an example, for λ_{ex} = 633 nm, I_{SERS} = 1282±167 and 1331±306 for *m*-NTP and *p*-NTP, respectively. The I_{SERS} values of *m*-NTP and *p*-NTP therefore do not differ drastically from each other at both the excitation wavelengths used in this study as verified using Student's *t* test. The calculated *t* for *m*-NTP and *p*-NTP is 0.32 and 1.48, respectively, and both are lower than Student's *t* value at 99.9% confidence level with ∞ degrees of freedom ($t_{Student}$ = 3.291).

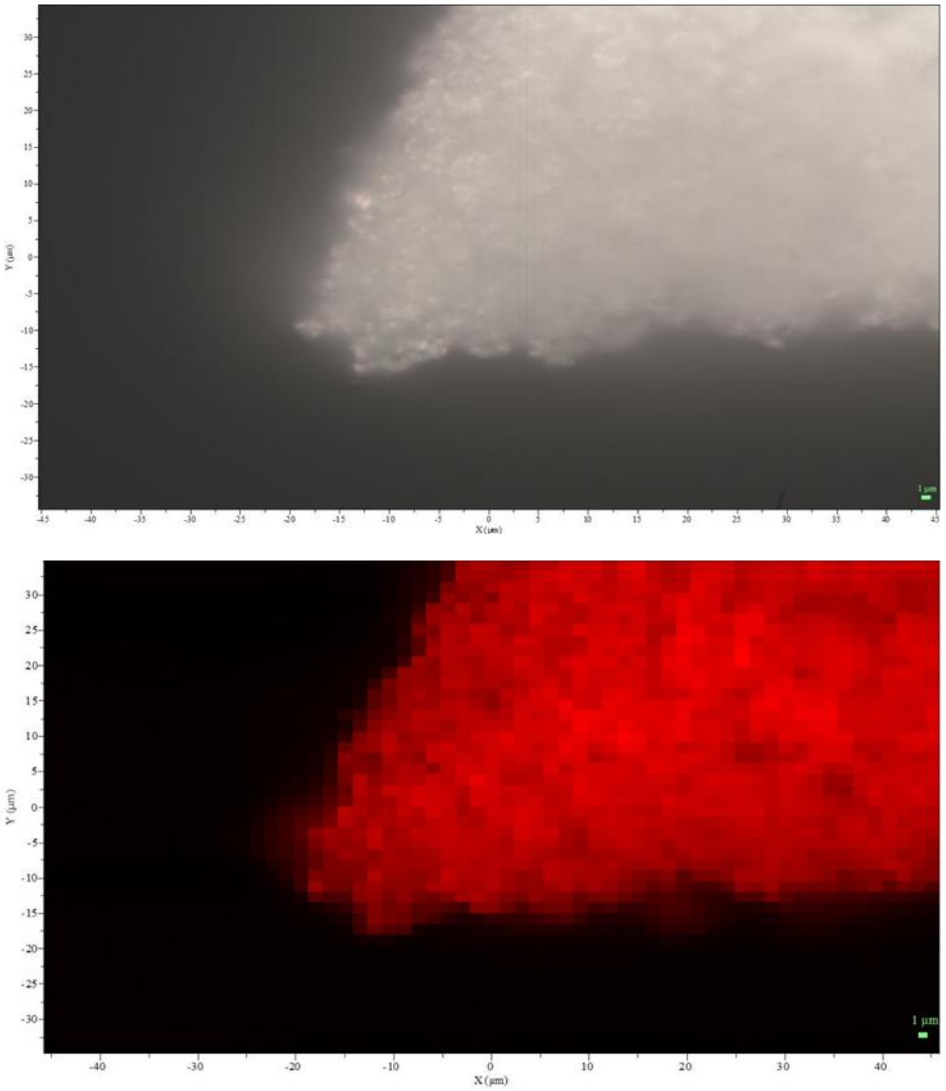
Y (µm)
30
25
20
15
10
5
0
-5
-10
-15
-20
-25
-30
1 µm
-45
-40
-35
-30
-25
-20
-15
-10
-5
0
5
10
15
20
25
30
35
40
45
X (µm)
Y (µm)
30
25
20
15
10
5
0
-5
-10
-15
-20
-25
-30
1 µm
-40
-30
-20
-10
0
10
20
30
40
X (µm)

Figure 8: An image of an aggregate of TiO_2 nanocrystals collected using white light (a), and by raster scanning with an excitation light of 633 nm and integration time per pixel of 0.5 s (b).

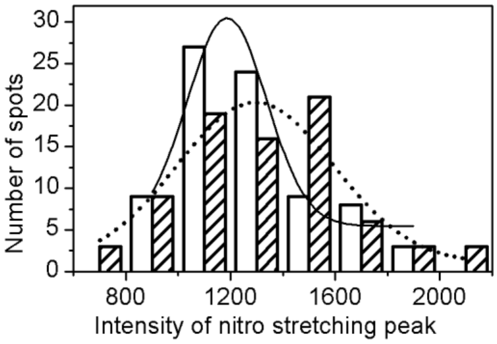

Figure 9: Distribution of the $\nu_s(NO_2)$ peak intensity for 80 different analysis spots for *m*-NTP (white bars) and *p*-NTP (stripe bars). The histograms are fitted to a Gaussian function (solid line for *m*-NTP and dotted line for *p*-NTP).

The SERS enhancement factor (*EF*) is calculated next using the following equation:

$$EF = (I_{SERS}/N_{SERS})/(I_R/N_R) \quad \text{......................................} \quad (1)$$

Where N_{SERS} and N_R are the numbers of NTP molecules excited by the laser light when adsorbed onto TiO_2 and dissolved in bulk (THF) solution, respectively, and I_R is the normal Raman intensity of the $\nu_s(NO_2)$ peak in THF. The detection volume of the Raman microscope is determined following the method described in references [33] and [36]. In this case, the radius of the diffraction-limited laser beam is obtained *via*

$$r = (0.61\lambda_{ex}/NA) \quad \text{...} \quad (2)$$

where *NA* is the numerical aperture of the objective, and the depth of the detection volume is calculated using

$$d = (2n\lambda_{ex}/NA^2) \quad \text{...} \quad (3)$$

where *n* is the refractive index of THF. For NTP in THF excited at 633 nm, the effective area of the laser beam $A = 0.58\ \mu m^2$, $d = 2.2\ \mu m$ and the detection volume (*V*), approximated using $V = A \times d$, is $1.3\ \mu m^3$, which is in line with previously reported values.[33,36] The number of *m*-NTP and *p*-NTP molecules in THF (0.1 M) that are effectively excited by the laser light is $N_R = 7.6 \times 10^7$.

A *minimum EF* value can be approximated by assuming that the probe molecules are tightly packed on the surface of the TiO_2 such that a uniformly distributed monolayer is formed.[33,36] The NTP molecules are taken to be oriented in an upright position due to the presence of intermolecular interaction (Figure 1). The number of adsorbed NTP molecules confined within a diffraction-limited area of TiO_2 for λ_{ex} = 633 nm is $N_{SERS} = 2.8 \times 10^6$ for *m*-NTP and $N_{SERS} = 3.7 \times 10^6$ for *p*-NTP, resulting in a minimum *EF* of 183±24 for *m*-NTP and 50±12 for *p*-NTP. The difference of N_{SERS} for *m*-NTP and *p*-NTP is due to nitro group: for *m*-NTP, the angle of *m*-NTP causes the molecule to occupy more space than *p*-NTP. When λ_{ex} = 488 nm, the minimum *EF* values for *m*-NTP and *p*-NTP are 224±34 and 53±10, respectively.

In order to better quantify the enhancement factor, the number of adsorbate molecules on TiO_2 is obtained from the EA results. Based on the BET surface area of the TiO_2 nanocrystals (*i.e.*, 55.2 m^2 g^{-1}) and assuming a uniform distribution of the probe molecules on the TiO_2 surface, $N_{SERS} = 1.0 \times 10^6$ for *m*-NTP and $N_{SERS} = 1.2 \times 10^6$ for *p*-NTP. The resulting *EF* is therefore 508±66 and 158±36 for *m*-NTP and *p*-NTP, respectively, for λ_{ex} = 633 nm. Using the same procedure, the *EF* values for *m*-NTP and *p*-NTP for λ_{ex} = 488 nm are 621±93 and 167±32, respectively. The *EF* values observed here are in line with those reported by Dong *et al.* who have determined an *EF* value in the order of 10^3 for the surface-enhanced Raman signal of *p*-mercaptobenzoic acid (*p*-MBA) on MoO_3 belt.[33] Yang *et al.* have also reported an *EF* ~ 1000 for 4-mercaptopyridine adsorbed onto ZnO.[36] We note that *m*-NTP exhibits a greater Raman signal enhancement as compared to *p*-NTP for both excitation wavelengths used such that the ratio of *EF* for *m*-NTP to *p*-NTP is *ca*. 3 to 4.

To improve the confidence the reported *EF* value, we repeated similar calculation for the peak around 1600 cm^{-1} and we obtained *EF* of 122±30 for *p*-NTP adsorbed onto TiO_2 excited with 633 nm which is close to calculated *EF* of 158±36 based on nitro stretching frequency at 633 nm. Furthermore, we calculated *EF* of to be 137±27 based on peak around 1600 cm^{-1} under 488 nm excitation wavelength which is close to calculated *EF* of 167±32 based on nitro stretching frequency at 488 nm. Unfortunately, we are unable to calculate *EF* of *m*-NTP based on 1600 cm^{-1} peak as the Raman peak from THF interferes with it.

We will discuss the possible SERS mechanism operating in the NTP-TiO_2 systems by first considering a recently proposed TiO_2-to-molecule CT process used to explain the enhanced Raman scattering of *p*-MBA on TiO_2.[15] In this model, electrons found in the valence band of TiO_2 are photoexcited into the surface state energy levels of the metal oxide before being transferred to the LUMO of the adsorbate. Therefore, the more electron withdrawing is the adsorbed probe molecule, the stronger is the SERS signal. We rule out this mechanism for the molecules considered here based on the following two observations.

Figure 10 shows the time-dependent SERS spectra of *p*-NTP adsorbed on silver powder (Ag) recorded with λ_{ex} = 633 nm and I_{ex} = 850 μW. It is seen that as the intensity of the $\nu_s(NO_2)$ peak at 1340 cm^{-1} decreases with time, several additional and distinct peaks emerge (*e.g.*, at 1142 cm^{-1}, 1392 cm^{-1} and 1442 cm^{-1}) which have been attributed to the vibrational modes of either *p*-aminothiophenol (*p*-ATP)[37,38] or *p,p′*-dimercaptoazobenzene (DMAB).[39,40] Since the Raman intensity of neat *p*-NTP remains relatively unchanged with time (Figure 10(c)), the time-dependent reduction in the $\nu_s(NO_2)$ peak intensity of *p*-NTP on Ag cannot be ascribed to the photodegradation of the adsorbate. Instead, when *p*-NTP is photoreduced to either *p*-ATP or DMAB upon electron transfer from Ag to *p*-NTP, a decrease in the $\nu_s(NO_2)$ peak intensity with time is observed.[37-40] On the other hand, the intensity of the SERS signal of *p*-NTP on TiO_2 is invariant with time when the sample is exposed to light (λ_{ex} = 633 nm and I_{ex} = 850 μW) for 180 s (Figure 10(b)). This clearly demonstrates that *p*-NTP does not undergo photoreduction on TiO_2 and electron transfer from the *n*-type semiconductor to NTP does not occur. Furthermore, based on the mesomeric effect, the -NO_2 group located *para*- to the thiol in *p*-NTP has a greater electron withdrawing ability as compared to the -NO_2 group located *meta*- to the thiol in *m*-NTP. In this case, a larger *EF* for *p*-NTP on TiO_2 is expected since the adsorbate has a greater ability to attract electron from the semiconductor. However, this is not observed experimentally which indicates that a TiO_2-to-molecule CT mechanism is not likely to be feasible in the NTP-TiO_2 systems studied here.

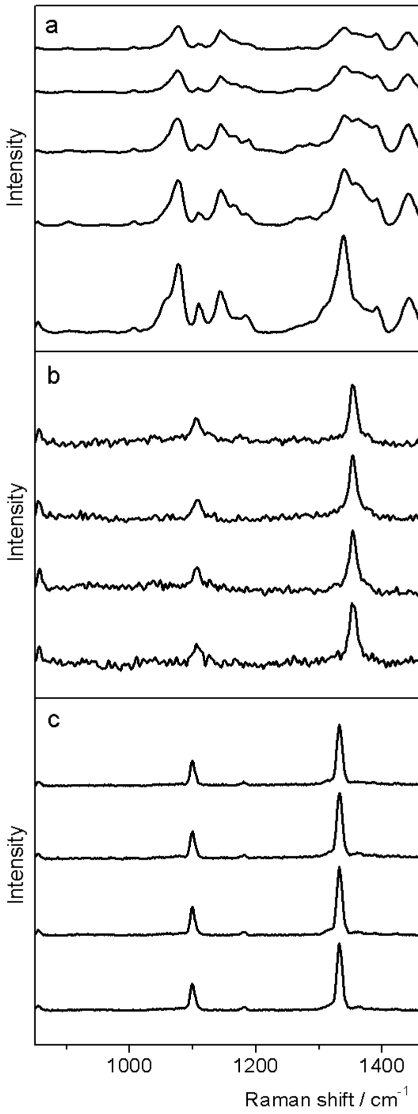

Figure 10: Time-dependent SERS spectra of *p*-NTP on Ag (a) and TiO_2 (b) and the Raman spectrum of neat *p*-NTP (c) recorded with λ_{ex} = 633 nm. The integration times for (a), (b) and (c) are 1 s, 10 s and 0.5 s, respectively.

In Figure 10a, we did not carry out the elemental analysis to quantify the amount of *p*-NTP adsorbed onto Ag as the enhancement factor on Ag substrate was not within the scope of this study. Nevertheless, another study carried out simple estimate of the number of molecules adsorbed onto the substrate by assuming a closely packed monolayer of molecules lying almost horizontal to the substrate surface.[33] Our computer simulation shows that *p*-NTP does adsorb horizontally onto Ag surface (Figure 11). The detection area is 0.58 μm^2 and each *p*-NTP molecule occupies an area of 0.48 nm^2. Hence, we estimate there are 1.2×10^6 *p*-NTP adsorbed onto Ag. We estimate there are 1.2×10^6 molecules of *p*-NTP adsorbed onto TiO_2 as determined from Elemental Analysis, detection area and BET surface area. The spectrum in Figure 10C was obtained by placing the powder form of neat *p*-NTP under microscope objective lens. The detection volume is 1.3 μm^3 and, from computer simulation, each *p*-NTP molecule will occupy a volume of 0.2 nm^3. Assuming a closely packed configuration, there will be 6.5×10^9 molecules of *p*-NTP.

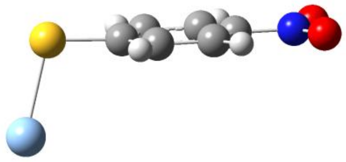

Figure 11: Adsorption of *p*-NTP onto Ag.

2.3.2 Absorbance spectrum

Another mechanism to consider is a SERS effect arising from a molecule-to-TiO_2 CT reaction.[17] We begin by presenting in Figure 12 the UV-vis absorption spectrum of *p*-NTP in THF solution (a), unmodified TiO_2 (b) along with the red-shifted absorption spectra of TiO_2 with *m*-NTP (c) and *p*-NTP (d) chemisorbed on the metal oxide surface. The absorption seen at the lower energy region of spectra c and d increases in absorbance with decreasing wavelength and resembles the absorption profile of unmodified TiO_2. Since the absorption of neat NTP isomers in solution occurs in the UV region, spectra c and d suggest that the effective bandgap of the molecule-TiO_2 system has a lower optical transition than that of the unmodified TiO_2 due to insertion of a charge-transfer transition.[39] This arises because of an appreciable interaction between adsorbate and semiconductor that drives a light-induced electron transition directly from the HOMO of the NTP isomer to the continuum conduction band (CB) of TiO_2 (Figure 13).[17,42] The excitation wavelengths used here are therefore in resonance with the CT transition.

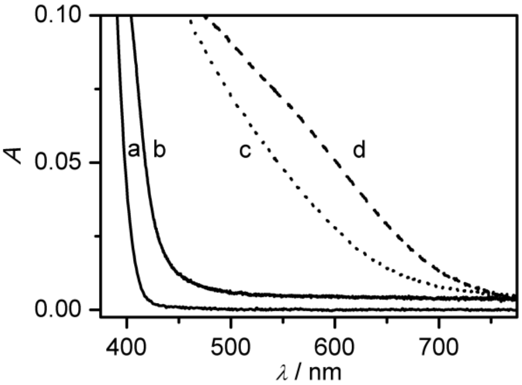

Figure 12. Absorption spectra of 70 μM *p*-NTP in THF solution (a), unmodified TiO_2 (b), TiO_2 with *m*-NTP (c) and *p*-NTP (d) adsorbed on the metal oxide surface. The amount of surface- modified TiO_2 exposed to the excitation light is different for *m*-NTP and *p*-NTP.

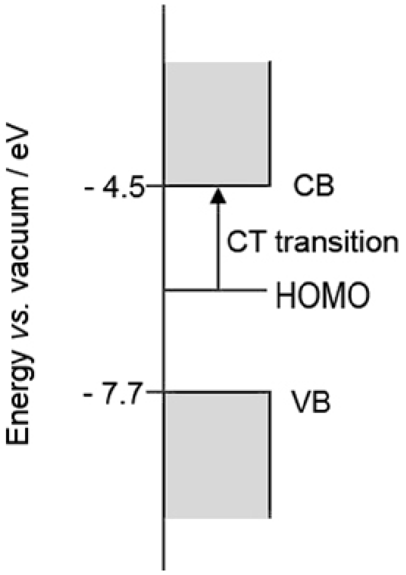

Figure 13: Energy level diagram depicting the energy of the CB and VB of TiO_2 and the HOMO of NTP. The energy gap between the HOMO of NTP and the CB of TiO_2 is ~1.5 eV.

2.3.3 Cyclic voltammetry

In order to further verify that such a CT transition is indeed energetically allowed, electrochemistry experiments (Figures 14 and 15) were conducted to determine the HOMO energy of *p*-NTP and *m*-NTP. Both of the HOMOs (-5.8 eV and -6.0 eV against vacuum for *p*-NTP and *m*-NTP, respectively) are located above the valence band (VB) edge of TiO_2 (-7.7 eV against vacuum, see Figure 13) and the energy gap between the HOMO and the edge of the CB of TiO_2 is *ca*. 1.5 eV (Figure 13). Clearly, the energy of the excitation light is sufficient to cause an electron to be injected from the HOMO of NTP into the CB of TiO_2.

Based on the above reasoning, we propose that the enhanced signal observed in Figure 7 arises from a surface-enhanced resonance Raman scattering (SERRS) effect from the surface complex. When the Raman signal of nitrothiophenol isomer on TiO_2 was recorded at a wavelength where the absorbance of the surface complex is low (*i.e.*, λ_{ex} = 785 nm, Figure 12), the Raman signal is significantly weaker than the one measured at λ_{ex} = 633 nm. Even when the laser power is increased from 850 μW to 1.5 mW, the Raman signal remains weak (Figure 16 for the case of *p*-NTP). This suggests that CE does not occur at the non-resonance excitation wavelength.

Since *p*-NTP is more electron withdrawing than *m*-NTP, electron-transfer from the former to TiO_2 is less efficient. Therefore, at resonance excitation, a smaller Raman signal enhancement is observed for *p*-NTP as compared to *m*-NTP. We note that the *EF* values for λ_{ex} = 488 nm and 633 nm are close to each other. However, a lack of knowledge about the exact nature of the damping parameter,[12] coupled with interferences from fluorescence on the Raman signal when λ_{ex} = 488 nm is used render a quantitative comparison between the *EF* values observed at the two excitation wavelengths difficult. Fluorescence is minimal for λ_{ex} = 633 nm which makes the *EF* values determined at this wavelength more reliable.

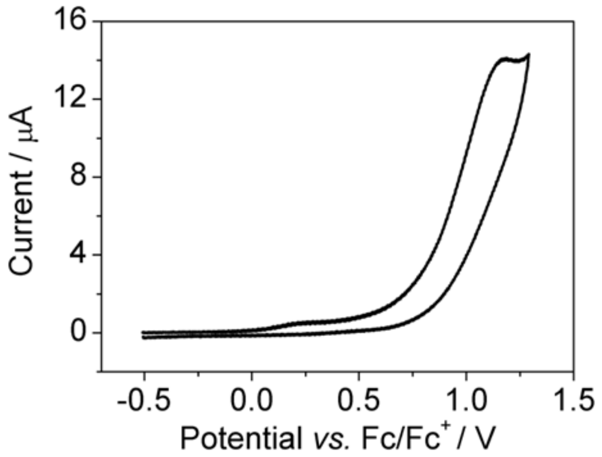

Figure 14: Cyclic voltammograms of *m*-NTP (2.6 mM in THF) against ferrocene (Fc) obtained with tetrabutylammonium hexafluorophosphate (0.2 M) as supporting electrolyte. The energy of the HOMO of *m*-NTP is calculated using the formula $E_{\mathrm{HOMO}} = -e(E_{\mathrm{ox}} + 4.8)$, where E_{ox} is the oxidation potential of *m*-NTP against ferrocene. From $E_{\mathrm{ox}} = 1.2$ V, the energy of the HOMO of *m*-NTP is -6 eV.

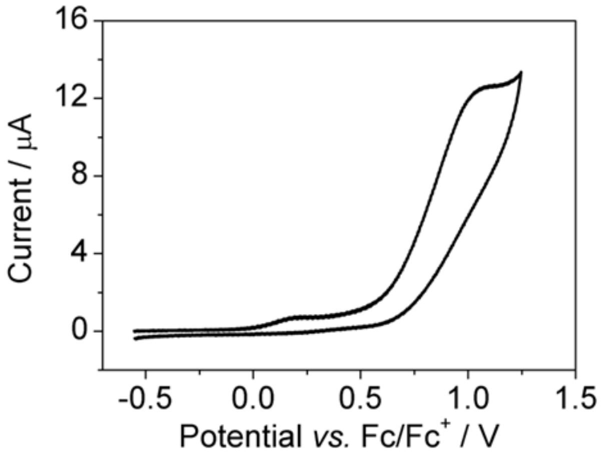

Figure 15: Cyclic voltammograms of *p*-NTP (2 mM in THF) against ferrocene (Fc) obtained with tetrabutylammonium hexafluorophosphate (0.2 M) as supporting electrolyte. The energy of the HOMO of *p*-NTP is calculated using the formula $E_{\mathrm{HOMO}} = -e(E_{\mathrm{ox}} + 4.8)$, where E_{ox} is the oxidation potential of *p*-NTP against ferrocene. From $E_{\mathrm{ox}} = 1$ V, the energy of the HOMO of *p*-NTP is -5.8 eV.

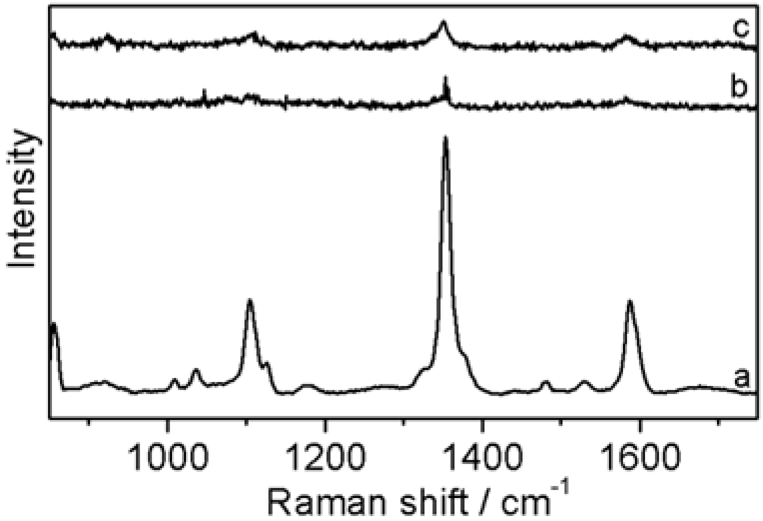

Figure 16: SERS of *p*-NTP chemisorbed onto TiO_2 obtained using (a) $\lambda_{ex} = 633$ nm and $I_{ex} = 850$ μW, (b) $\lambda_{ex} = 785$ nm and $I_{ex} = 850$ μW, and (c) $\lambda_{ex} = 785$ nm and $I_{ex} = 1500$ μW.

2.3.4 DFT calculations

To gain additional insights into the CT transition, DFT calculations were carried out on isolated NTP and NTP bound to a $(TiO_2)_2$ cluster.[43] The HOMO and LUMO images of the isolated and bound *p*-NTP and *m*-NTP are shown in Figure 17. It is observed that for *m*-NTP, the HOMO of the bound molecule matches the HOMO of the isolated molecule. For isolated *p*-NTP, the HOMO is localized towards the thiol end of the molecule. However, upon binding with a $(TiO_2)_2$ cluster, the HOMO becomes localized throughout the whole NTP and resembles the (HOMO – 1) of isolated *p*-NTP (Figure 18). This is because the latter has a better overlap, as compared to the *p*-NTP HOMO, with the *d*-orbital of Ti. It is clearly seen that for the bound *p*-NTP and *m*-NTP, the HOMO is completely localized on the adsorbate whereas the LUMO is localized entirely on the $(TiO_2)_2$ cluster. The DFT calculations therefore support our proposed model that CT transition takes place from the adsorbate to TiO_2 in the surface complex.

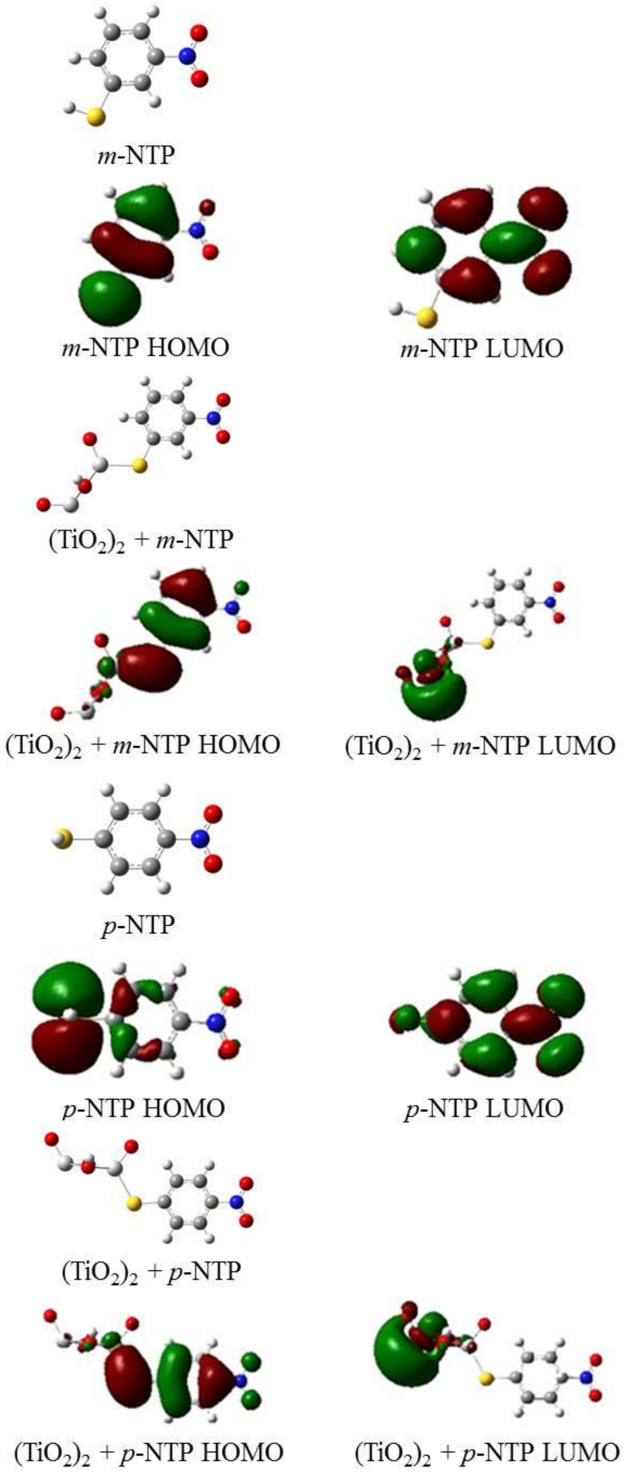
m-NTP
m-NTP HOMO
m-NTP LUMO
(TiO2)2 + m-NTP
(TiO2)2 + m-NTP HOMO
(TiO2)2 + m-NTP LUMO
p-NTP
p-NTP HOMO
p-NTP LUMO
(TiO2)2 + p-NTP
(TiO2)2 + p-NTP HOMO
(TiO2)2 + p-NTP LUMO

Figure 17: DFT calculated optimized geometry, HOMO and LUMO of isolated *m*-NTP and *p*-NTP and *m*-NTP and *p*-NTP bound to a $(TiO_2)_2$ cluster.

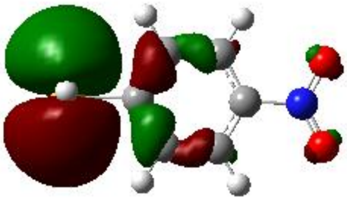

HOMO of isolated*p*-NTP

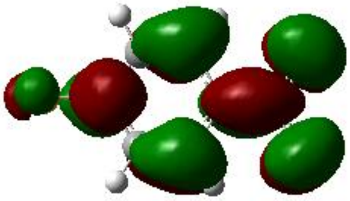

LUMO of isolated *p*-NTP

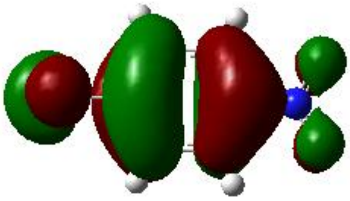

HOMO-1 of isolated *p*-NTP

Figure 18: Molecular orbital images of isolated *p*-NTP and *p*-NTP adsorbed onto a $(TiO_2)_2$ cluster.

The effect of EE contribution to the SERS of probe molecules on TiO_2 is not considered here. Pérez León *et al.* have reported a Raman signal, albeit weak, of a Ru-bpy dye on TiO_2 excited using an off-resonance visible light.[18] The authors have proposed that EE may be present due to an interaction with the surface plasmon resonances *via* the very rough surfaces of TiO_2.[44] Recently, Lombardi *et al.*[15] and Rajh *et al.*[17] have provided reasons for neglecting the EE factor when considering SERS of probe molecules chemisorbed on TiO_2. In particular, from the formula:

$$\omega_p = [4\pi n e^2 / m_e \varepsilon_\infty] \quad \ldots\ldots\ldots\ldots\ldots\ldots\ldots\ldots \quad (4)$$

where n is the electron carrier density and m_e is the effective electron mass, ε_∞ is optical dielectric constant (obtained as square of optical refractive index). The plasmon resonance frequency ω_p of metal oxides such as TiO_2 and ZnO are located in the infrared region[15,36] which is far away from the excitation wavelengths used in this study. Therefore, the effects of plasmon resonance and EE do not play a significant role in promoting the observed SERS of nitrothiophenol isomers on TiO_2.

The Herzberg-Teller effect consisting of the coupling term *h* and the $<i|Q|f>$ term, where *Q* is the normal mode,[12,45] should be non-zero for the system studied here. The $<i|Q|f>$ term implies that apart from totally symmetric modes (*e.g.*, the $\nu_s(NO_2)$ band), nontotally symmetric modes may also be allowed. The enhancement of the Raman intensity from a CT process occurs when the CT intensity borrows from some allowed molecular transitions *via* the coupling term *h*.[12] The experimental quantification of *h* is non-trivial,[45,46] however, it can be taken to be proportional to the polaron-coupling term α.[46] In the case of TiO_2, α is relatively large (*i.e.*, $\alpha = 3.6$),[47] implying that the Herzberg-Teller effect is non-negligible in SERS involving the TiO_2 semiconductor.[46]

For probe molecules on metallic Ag, an important parameter that controls the SERS intensity is the dipole transition moment for the metal-to-molecule or molecule-to-metal transition.[12,45] For Ag, the plasmon resonance produces an electric field perpendicular to the metal surface which then interacts favorably with a transition moment of the probe that is polarized perpendicular to the metal surface. The orientation of the molecule with respect to the Ag is therefore important.[45] In the case of TiO_2, the plasmon resonance effect is inactive and it is therefore not clear at the present moment how the surface selection rules used in metallic Ag apply, if at all, to charge-transfer enhancement in TiO_2-based systems. The theoretical treatment of this issue is beyond the scope of the present study. However, previous investigations have clearly shown that the electron donating/withdrawing ability of the adsorbate is important and affects the overall chemical enhancement of the Raman signal.[15] In particular, for a TiO_2-to-molecule CT process, the

CE of the Raman signal increases in the order of *p*-mercaptobenzoic acid > *p*-mercaptopyridine > *p*-aminothiophenol since the electron attracting ability of groups *para*-to –SH increases in the order C-COOH > N > C-NH_2.[15] A recent theoretical investigation by Zhao and Liang has also elucidated the effects of several factors governing electron transfer (*e.g.*, electronic coupling) on the Raman scattering of dye molecules on semiconductor.[48]

2.4 Conclusion

In conclusion, *m*-NTP and *p*-NTP exhibit enhanced Raman scattering when chemisorbed onto the surface of TiO_2 nanocrystals. The SERS effect arises from a CT transition from the HOMO of the adsorbate to the CB of TiO_2. Since *m*-NTP is a better electron donor than *p*-NTP, the observed SERS enhancement factor is larger for *m*-NTP.

2.5 References

(1) Kneipp, J.; Kneipp, H.; Kneipp, K. *Chem. Soc. Rev.* **2008**, *37*, 1052.

(2) Jarvis, R. M.; Goodacre, R. *Anal. Chem.* **2004**, *76*, 40.

(3) Mulvihill, M.; Tao, A.; Benjauthrit, K.; Arnold, J.; Yang, P. *Angew. Chem.Int. Ed.***2008**, *47*, 6456.

(4) Percot, A.; Leconte, S.; Vergne, J.; Maurel, M. C. *Biopolymers* **2009**, *91*, 384.

(5) Aroca, R. *Surface-Enhanced Vibrational Spectroscopy*, John Wiley & Sons, West Sussex, **2006**

(6) Etchegoin, P. G.; Lacharmoise, P. D.; Le Ru, E. C. *Anal. Chem.* **2009**, *81*, 682.

(7) Wustholz, K. L.; Brosseau, C. L.; Casadio, F.; Van Duyne, R. P. *Phys.Chem. Chem. Phys.* **2009**, *11*, 7350.

(8) Pieczonka, N. P.W.; Aroca, R. F. *Chem. Soc. Rev***. 2008**, *37*, 946.

(9) Kambhampati, P.; Child, C. M.; Foster, M. C.; Campion, A. *J. Chem. Phys.* **1998**, *108*, 5013.

(10) Campion, A.; Kambhampati, P. *Chem. Soc. Rev*. **1998**, *27*, 241.

(11) Lombardi, J. R.; Birke, R. L.; Lu, T.; Xu, J. *J. Chem. Phys*. **1986**, *84*, 4174.

(12) Lombardi, J. R.; Birke, R. L. *Acc. Chem. Res*. **2009**, *42*, 734.

(13) Anderson, N. A.; Lian, T. *Annu. Rev. Phys. Chem*. **2005**, *56*, 491.

(14) Wu, X.; Bell, T. D. M.; Yeow, E. K. L. *Angew. Chem. Int. Ed*. **2009**, *48*, 7379.

(15) Yang, L.; Jiang, X.; Ruan, W.; Zhao, B.; Xu, W.; Lombardi, J. R. *J. Phys. Chem. C* **2008**, *112*, 20095.

(16) Shoute, L. C. T.; Loppnow, G. *J. Chem. Phys*. **2002**, *117,* 842.

(17) Musumeci, A.; Gosztola, D.; Schiller, T.; Dimitrijevic, N. M.; Mujica, V.; Martin, D.; Rajh, T. *J. Am. Chem. Soc.* **2009**, *131*, 6040.

(18) Pérez León, C.; Kador, L.; Peng, B.; Thelakkat, M. *J. Phys. Chem. B* **2006**, *11*0, 8723.

(19) Tanaka, T.; Nakajima, A.; Watanabe, A.; Ohno, T.; Ozaki, Y. *J. Mol. Struct.* **2003**, *661-662*, 437.

(20) Ma, W.; Fang, Y. *J. Colloid Interface Sci*. **2006**, *303*, 1.

(21) Perry, D. A.; Son, H. J.; Cordova, J. S.; Smith, L. G.; Biris, A. S. *J.Colloid Interface Sci.* **2010**, *342*, 311.

(22) Perry, D. A.; Cordova, J. S.; Spencer, W. D.; Smith, L. G.; Biris, A. S. *J. Phys. Chem. C* **2010**, *114*, 14953.

(23) Moskovits, M. *J. Chem. Phys*. **1982**, *77*, 4408.

(24) Yoon, J, H,; Park, J. S.; Yoon, S. *Langmuir* **2009**, *25*, 12475.

(25) Bellale, E. V.; Chaudhari, M. K. Akamanchi, K. G. *Synthesis* **2009**, *19*, 3211.

(26) Kabalka, G.W.; Reddy, M. S.; Yao, M. -L. *Tetrahedron Lett*. **2009**, *50*, 7340.

(27) Wang, X.; Feng, Z.; Shi,, J.; Jia,, G.; Shen, S.; Zhou, J.; Li, C. *Phys. Chem. Chem. Phys.* **2010**, *12*, 7083.

(28) Shi, J.; Chen, J.; Feng, F.; Chen, T.; Lian, Y.; Wang, X.; Li, C. *J. Phys. Chem. C* **2007**, *111*, 693.

(29) Thelakkat, M.; Schmidt, H. –W. *Adv. Mater.* **1998**, *10*, 219.

(30) *Gaussian 09*, Revision A.02,Frisch, M. J.; Trucks, G. W.; Schlegel, H. B.; Scuseria,G. E.; Robb, M. A.; Cheeseman, J. R.; Scalmani,G.; Barone, V.; Mennucci, B.; Petersson, G. A.; Nakatsuji, H.; Caricato, M.; Li,, X.; Hratchian, H. P.; Izmaylov, A. F.; Bloino, J.; Zheng,, G.; Sonnenberg, J. L.; Hada, M.; Ehara, M.; Toyota, K.; Fukuda, R.; Hasegawa, J.; Ishida, M.; Nakajima, T.; Honda, Y.; Kitao,O.; Nakai, H.; Vreven, T.; Montgomery, J. A.; Peralta, Jr. J. E. Ogliaro, F.; Bearpark, M.; Heyd, J. J.; Brothers, E.; Kudin, K. N.; Staroverov, V. N.; Kobayashi, R.; Normand, J.; Raghavachari, K.; Rendell, A.; Burant, J. C.; Iyengar, S. S.; Tomasi, J.; Cossi, M.; Rega, N.; Millam, J. M.; Klene, M.; Knox, J. E.; Cross, J. B.; Bakken, V.; Adamo, C.; Jaramillo, J.; Gomperts, R.; Stratmann, R. E.; Yazyev, O.; Austin, A. J.; Cammi, R.; Pomelli, C.; Ochterski, J. W.; Martin, R. L.; Morokuma, K.; Zakrzewski, V. G.; Voth, G. A.; Salvador, P.; Dannenberg, J. J.; Dapprich, S.; Daniels, A. D.; Farkas, Ö.; Foresman,J. B.; Ortiz, J. V.; Cioslowski, J.; Fox, D. J. Gaussian, Inc., Wallingford CT, **2009**.

(31) Love, J. C.; Estroff, L. A.; Kribel, J. K.; Nuzzo, R. G.; Whitesides, G. M. *Chem. Rev.* **2005**, *105*, 1103.

(32) Häkkinen, H. *Nature Chem.* **2012**, *4*, 443.

(33) Dong, B.; Huang, Y.; Yu, N.; Fang, Y.; Cao, B.; Li, Y.; Xu, H.; Sun, M. *Chem. Asian. J*. **2010**, *5*, 1824.

(34) Skadtchenko, B. O.; Aroca, R. *Spectrochemica. Acta, Part A* **2001**, *57*, 1009.

(35) Futamata, M. *J. Phys. Chem*. **1995**, *99*, 11901.

(36) Wang, Y.; Ruan, W.; Zhang, J.; Yang, B.; Xu, W.; Zhao, B.; Lombardi, J. R. *J. Raman Spectrosc*. **2009**, *40*, 1072.

(37) Matsuda, N.; Sawaguchi, T.; Osawa, M.; Uchida, I. *Chem. Lett*. **1995**, 145.

(38) Kim, K.; Lee, Y. M.; Lee, H. B.; Park, Y.; Bae, T. Y.; Jung, Y. M.; Choi, C. H.; Shin, K. S. *J. Raman. Spectrosc*. **2010**, *41*, 187.

(39) Dong, B.; Fang, Y.; Xia, L.; Xu, H.; Sun, M. *J. Raman Spectrosc*. **2011**, *42*, 1205.

(40) Dong, B.; Fang, Y.; Chen, X.; Xu, H.; Sun, M. *Langmuir***2011**, *27*, 10677.

(41) Rajh, T.; Chen, L. X.; Lukas, K.; Liu, T.; Thumauer, M. C. Tiede, D. M. *J. Phys. Chem. B* **2002**, *106*, 10543.

(42) Duncan, W. R.; Prezhdo, O. V. *Annu. Rev. Phys. Chem*. **2007**, *58*, 143.

(43) Tarakeshwar, P.; Finkelstein-Shapiro, D.; Rajh,, T.; Mujica, V. *Int. J. Quantum Chem*. **2011**, *111*, 1659.

(44) Hugot-Le Goff, A.; Joiret, S.; Falaras, P. *J. Phys. Chem. B* **1999**, *103*, 9569.

(45) Lombardi, J. R.; Birke, R. L. *J. Phys. Chem. C* **2008**, *112*, 5605.

(46) Lombardi, J. R.; Birke, R. L. *J. Chem. Phys.* **2007**, *126*, 244709.

(47) Yahia, J. *Phys. Lett*. **1966**, *23*, 425.

(48) Zhao, Y.; Liang, W. Z. *J. Chem. Phys*. **2011**, *135*, 044108.

CHAPTER 3

OTHER ORIGINS FOR THE FLUORESCENCE MODULATION OF SINGLE DYE MOLECULES IN OPEN-CIRCUIT AND SHORT CIRCUIT DEVICES

This chapter is adapted from "Other Origins for the Fluorescence Modulation of Single Dye Molecules in Open-Circuit and Short-Circuit Devices, Teguh, J. S.; Kurniawan, M.; Wu, X.; Sum, T. C.; Yeow, E. K. L. *Phys. Chem. Chem. Phys.* **2013**, *15*, 90-93."

3.1 Introduction

Photoexcited single dye molecules,[1,2] quantum dots[3] and conjugated polymers[4,5] display fluorescence intensity modulation when subjected to an external electric field (EF). For dye molecules, such as squaraine-derived rotaxane, the emission intensity of single chromophores varies with the amplitude of the modulating EF.[1,2] It has been proposed that this arises from an EF-induced change in the electron transfer efficiency between molecules and traps found in the surrounding nano-environment (*e.g.*, polymer film).[1,2] Furthermore, single dye molecules in a spectroelectrochemical cell coupled to a microscope undergo reversible redox reaction to form weakly emitting species, such that the observed fluorescence modulates with the cyclic voltammetric potential scan.[6] Apart from the influence of EF, electric current (EC) has also been shown to cause fluorescence fluctuation for single dye molecules (*e.g.*, 1,1′-dioctadecyl-3,3,3′,3′-tetramethyl indodicarbocyanine) on indium tin oxide (ITO) in a short-circuit device.[7] A plausible reason for this behavior is the adjustment of the Fermi level of ITO by the applied EC which leads to a change in the interfacial electron transfer dynamics between the two moieties.[7]

The majority of single-molecule fluorescence detection experiments are conducted on a scanning confocal fluorescence microscope where the excitation light is focused by an objective lens to a tight spot on a molecule located at the focal plane, and the fluorescence is subsequently collected using the same objective lens. Therefore, an out-of-focus illuminating light will result in a decrease in the recorded emission intensity. In this communication, the effects of an applied EF and EC on the focus of an excitation light in an open-circuit device and a short-circuit device, respectively, are investigated. Before understanding the roles played by intrinsic photophysical processes (*e.g.*, charge transfer) in single-molecule fluorescence modulation, it is necessary to first elucidate any possible contributions from EF- or EC-induced out-of-focus excitation light on the emission intensity change.

In this study, two types of devices were constructed as shown in Figure 1. The short-circuit device was prepared by painting a thin U-shaped silver (Ag) electrode on top of a glass cover slip, and single dye molecules were subsequently deposited at the centre of the cover slip (see Figure 1a). The open-circuit device, shown in Figure 1b, was prepared by spin coating in sequence polystyrene (PS) film on an ITO-coated glass cover slip, thin polyvinyl alcohol (PVA) film containing single Atto647N molecules (Figure 2), and a poly(methyl methacrylate) (PMMA) film. An aluminium (Al) electrode was then deposited on top of the PMMA film by thermal evaporation. The device structure is similar as the one described in the literature[5] with the exception of thick polystyrene layer being used in the place of silicon dioxide. The two parallel arms of the electrode in the short-circuit device and the ITO and Al electrodes in the open-circuit device were connected to a power generator that provided a sinusoidal voltage at 0.1 Hz.

3.2 Experimental section

3.2.1 Materials

Glass cover slips (20 × 20 mm^2, thickness #1, mass of 0.14 g) and quartz cover slips (20 × 20 mm^2, thickness #1, mass of 0.18 g) were purchased from Menzel-Gläser and Trade 21, respectively. Polystyrene (PS, average M_n 130000, average M_w 290000), poly(methylmethacrylate) (PMMA, average M_w 120000), and toluene (spectrophotometric grade) were obtained from Sigma Aldrich. Polyvinyl alcohol (PVA, average M_w 57000-66000) was purchased from Alfa Aesar. Silver paint, indium tin oxide (ITO) coated glass cover slips (20 × 20 mm^2, thickness #1, resistance 8-12Ω) and Atto647N dyes (see Figure 2) were purchased from RS Components, SPI Supplies and ATTO-TEC GmbH, respectively.

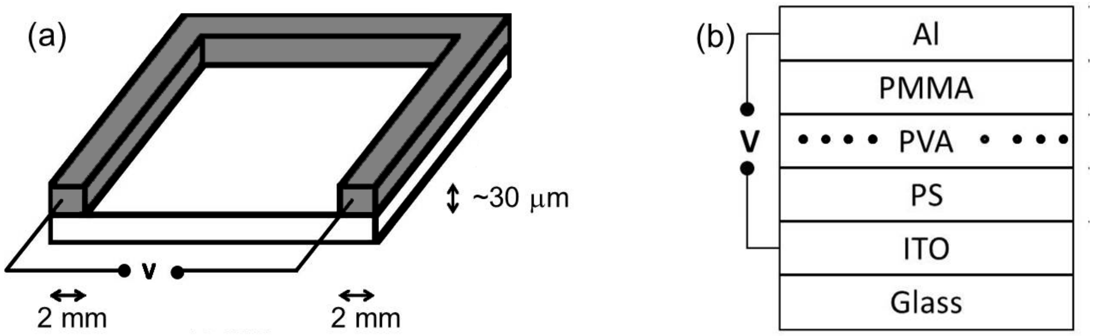

Figure 1: (a) A short-circuit device fabricated by painting a U-shaped silver paste (grey) on top of a glass cover slip and single Atto647N molecules are deposited at the center of the device, and (b) an open-circuit device where the thicknesses of the polystyrene PS, polyvinyl alcohol PVA, poly(methyl methacrylate) PMMA and Al layers are 450, 30, 55 and 100 nm, respectively. Single Atto647N molecules are embedded in the PVA matrix (● = Atto647N molecule). The width and thickness of the Ag electrode are 2 mm and ~30 μm, respectively.

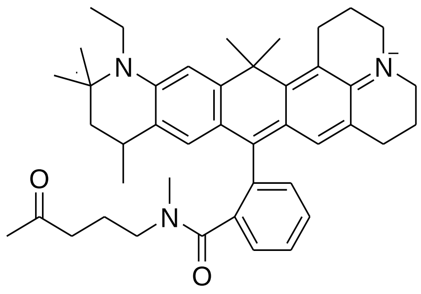

Figure 2: Chemical structure of ATTO 647N.[8]

3.2.2 Short-circuit device

For a short circuit device (Figure 1a), a U-shaped silver electrode with a width of ~2 mm was painted on either a cleaned glass cover slip, quartz cover slip or glass petri dish (mass of 107 g). The device was then heated at 120 ^{o}C for 30 mins to achieve maximum conductivity. The thickness of the electrode was measured using a surface profiler (Dektek 150, Veeco). Single dye molecules and a bulk concentration of Atto647N molecules were deposited onto the center of the device by spincoating an aqueous solution of Atto647N of ~10^{-11} M and ~10^{-6} M, respectively.

3.2.3 Open-circuit device

For an open-circuit device (Figure 1b), 450 nm PS layer was deposited onto an ITO coated cover slip by spincoating 150 μL toluene solution of PS (50 mg/mL). Subsequently, PVA layer (30 nm) containing single Atto647N molecules was prepared by spincoating 150 μL aqueous solution of dye/PVA (10 mg/mL PVA, and ~10^{-11} M dye) onto the PS film. PMMA film (55 nm) was then deposited from a 150 μL toluene solution of PMMA solution (10 mg/mL), followed by thermal evaporation (KCR-480S Evaporation Coating System) of an aluminum electrode (100 nm). The busbars on the ITO coated cover slip were protected using sticky tapes during the deposition of the polymer layers and Al electrode and the tapes were subsequently removed during measurements). The electric field experienced by the single molecules was defined as the ratio of the applied voltage to the separation between the two opposite electrodes (ignoring the dielectric constant of the polymer layers). Aluminum film used in device study remained electrically conductive throughout the study, indicating minimum oxidation of aluminum to become electrically insulating aluminum oxide. Oxidation of aluminum may occur during thermal evaporation when the pressure in the chamber is high enough. Hence, we prevent oxidation of aluminum by pumping the chamber pressure down to ~3×10^{-4} Pa. Alternatively, the minimum formation of insulating aluminum oxide prevented further oxidation of aluminum.

The two parallel arms of the electrode in the short-circuit device and the ITO and Al electrodes in the open-circuit device were carefully connected *via* wires to a function generator (TG550, Thurlby Thandar Instruments) that provided a sinusoidal voltage at 0.1 Hz. A digital multimeter (Mode1009, Kyoritsu) was used to determine if a device was short-circuited.

3.2.4 Single molecule spectroscopy

The device was held in place in a home-made sample holder by using sticky tape at the four corners, and then mounted onto a time-resolved confocal microscope (MicroTime 200, Pico Quant GmbH) equipped with an inverted microscope (IX71, Olympus). Excitation light from a pulse laser diode (635 nm, LDH-P-C-635B, PicoQuant) was passed through an excitation filter (Z636/10, Chroma) and focused through either an oil objective lens (1.4 numerical aperture, 100× magnification, Olympus) or air objective lens (0.9 numerical aperture, 60× magnification, Olympus). The fluorescence from single dye molecule was passed through a dichroic mirror (Z638rpc, Chroma) and an emission filter (HQ685/70, Chroma) before being detected by a single-photon avalanche diode (SPCM-AQR-15, Perkin Elmer). The backscattered excitation light was recorded by removing the emission filter before detection and the corresponding beam spot was captured using a CCD camera (GANZ ZC-F10C2). A confocal fluorescence image of single fluorescent Atto647N molecules from an open-circuit device (Figure 1b) is given in Figure 3.

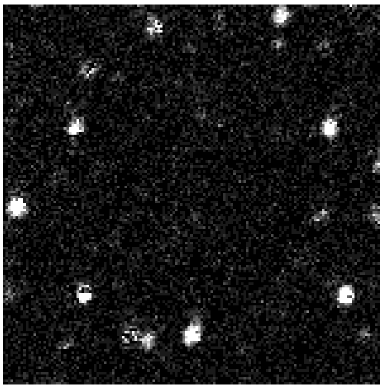

Figure 3: A confocal fluorescence image of single fluorescent Atto647N molecules from an open-circuit device (Figure 1b).

3.2.5 Ellipsometry and AFM

Refractive index measurement was done using a spectroscopic ellipsometer (Auto SE, Horiba Jobin Yvon).The integration time was set to be 60 s in each measurement. The thicknesses of the polymer films were determined using an atomic force microscope AFM (D3100V, Veeco Digital Instruments. The displacement of the device with respect to the objective lens was quantified using an AFM in a non-contact mode (Nanosurf easyScan 2).

3.3 Result and discussion

3.3.1 Short-circuit device

Typical fluorescence intensity time traces of single Atto647N molecules in a short-circuit device (Figure 1a) are provided in Figure 4b for an external sinusoidal potential (at frequency of 0.1 Hz) ranging from (i) +2 V to -2 V (maximum EC of 0.06 A generated), and (ii) +3 V to -3 V (maximum EC of 0.09 A). We note that the fluorescence intensity of the single molecules decreases when a voltage is initially applied at 10 s (Figure 4b). The

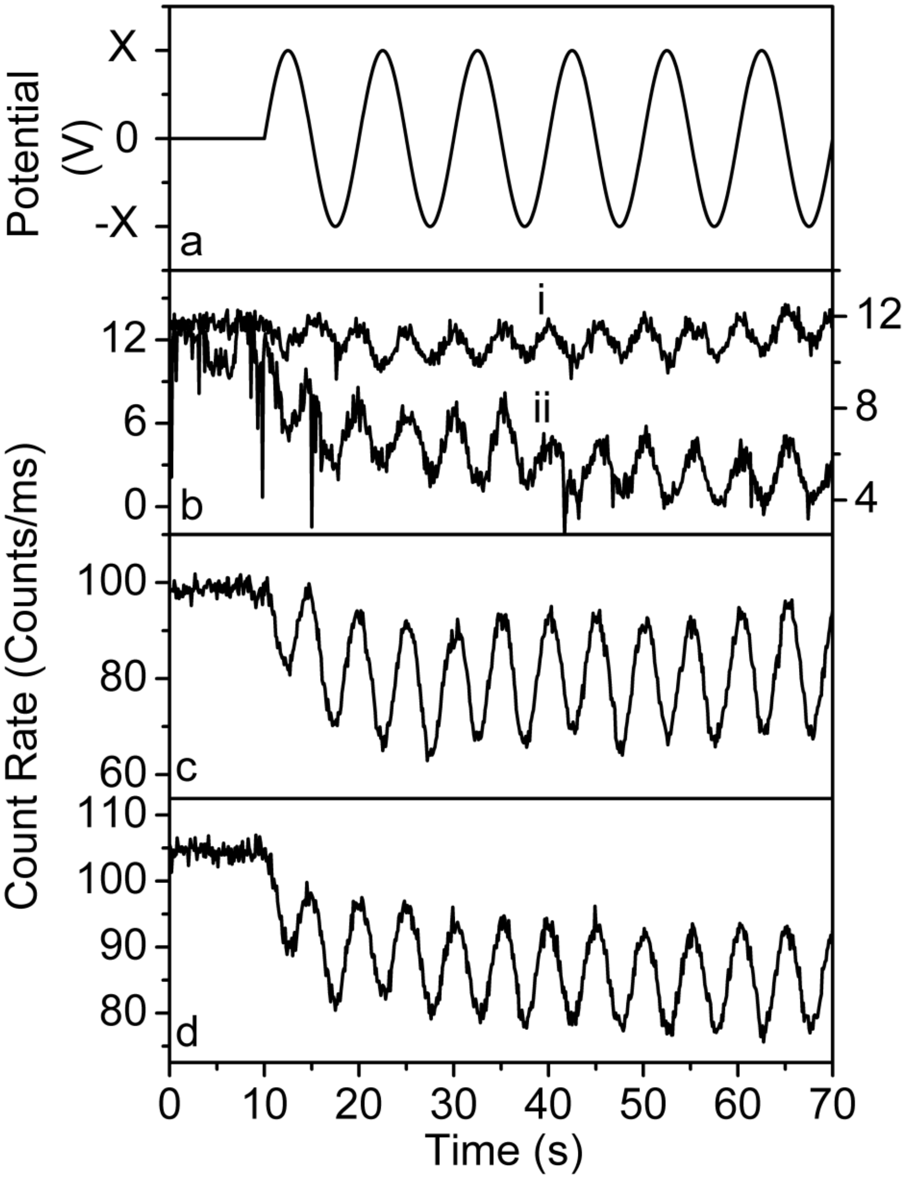

Figure 4: (a) Sinusoidal external potential (frequency of 0.1 Hz) applied to a short-circuit device. (b) Fluorescence intensity time trace of a single molecule in a short-circuit device subjected to a potential ranging from (i) +2 V to -2 V (left-axis) and (ii) +3 V to -3 V (right-axis). (c) Fluorescence intensity time trace of a bulk concentration of Atto647N and (d) BEL intensity of a short-circuit device subjected to a potential ranging from +3 V to -3 V. The external potential was applied 10 s after the start of the measurements and an oil objective lens was used.

emission intensity time trace subsequently displays a sinusoidal oscillation at a frequency of 0.2 Hz. Minimum fluorescence (*i.e.*, trough of the wave) is observed when either a +2 V/+3 V or -2 V/-3 V voltage is applied; corresponding to an EC flow of 0.06/0.09 A in the electrode. The fluorescence intensity increases when the EC decreases and reaches a maximum (*i.e.*, crest of the wave) at zero potential (*i.e.*, zero EC). Similar oscillatory behaviour in the fluorescence intensity time trace of an ensemble of Atto647N molecules in a short-circuit device is also observed (Figure 4c). Since the dye molecules are not in contact with the Ag electrode, their photophysical properties such as fluorescence quantum yield are not influenced by the alternating EC.

The effects of EC on the focus of the excitation light were investigated by recording the backscattered excitation light (BEL) intensity and corresponding beam spot image from a short-circuit device. For potential ranging from +3 V to -3 V, the intensity of the BEL undergoes a sinusoidal modulation at a frequency of 0.2 Hz (Figure 4d). Minimum (trough) and maximum (crest) intensities are observed at +3 V/-3 V and 0 V, respectively; similar to the single-molecule fluorescence modulation seen in Figure 4b. In addition, the beam spot image of the BEL changes its shape pattern according to the amount of applied potential (see Figure 5 and the accompanying Movie 1). In particular, the beam spot pattern is most diffused at voltages +3 V (t = 6.5 s in Figure 5) and -3 V (t = 11.5 s in Figure 5), and regains sharpness whenever the voltage approaches zero. This clearly shows that the excitation light becomes increasingly out-of-focus with respect to the focal plane (*i.e.*, in the z-direction) when the intensity of the EC increases, and regains focus when the EC is reduced to zero. Therefore, the fluorescence modulation observed in Figure 4b is ascribed to changes in the focus of the excitation beam. The modulation in the BEL was observed when using both oil and air objective lens.

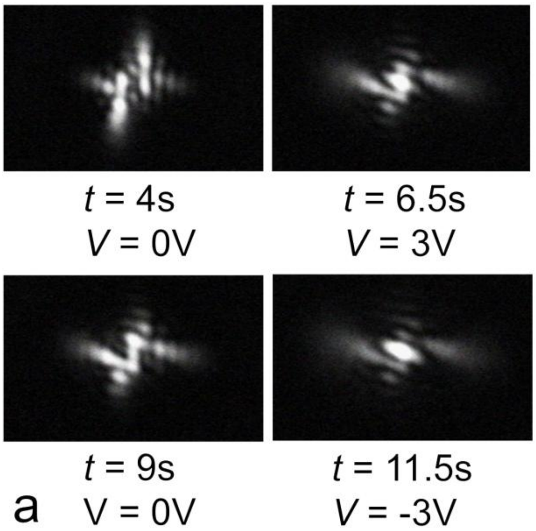

Figure 5: (a) Beam spot images from the BEL from a short-circuit device subjected to a sinusoidal potential ranging from V = +3 V to – 3V. The time when the potential is first applied after the start of the experiment is t = 4 s.

We next discuss the possible reasons for the out-of-focus excitation light when an EC flows in a short-circuit device. From ellipsometry measurements, the refractive index of the glass substrate (1.537) does not change before and after the application of an external potential. This means that an EC in the Ag electrode does not influence the refractive index of the glass substrate. Another plausible explanation for the out-of-focus excitation beam is the displacement of the device away from the objective lens when a current is flowing in the electrode. We propose that when an EC is generated, a mechanical jerk in the electrode lifts the whole device upwards and away from the objective lens. The device subsequently relaxes back to a position closer to the focused position when the EC reduces to zero. At high potential bias, there is a significant drop in the BEL intensity when the voltage is initially applied (*e.g.*, +3 V in Figure 4d and +10 V in Figure 6b), and the intensity does not return to its original value recorded before the application of the potential; suggesting the presence of a relatively large initial displacement position by the

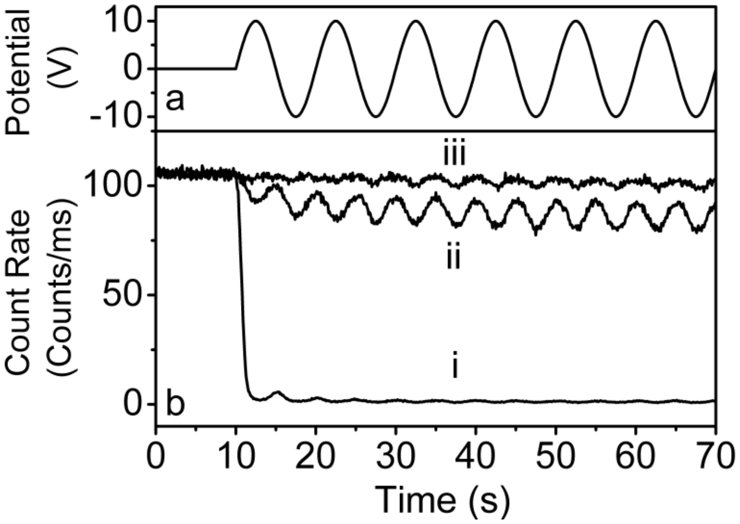

Figure 6: (a) Sinusoidal external potential (frequency of 0.1 Hz) applied to a short-circuit device, as depicted in Scheme 1a. (b) BEL intensity time traces of a short-circuit device fabricated from (i) glass cover slip, (ii) quartz cover slip and (iii) glass petri dish and subjected to a potential ranging from +10 V to -10 V. The BEL intensity time traces were measured using an oil objective lens

large Ag electrode. A control experiment, conducted using a short-circuit device fabricated from a significantly heavier glass substrate (*i.e.*, base of a petri dish), did not show any drastic drop in the BEL intensity (Figure 6b) when a potential is applied; indicating that the mechanical jerk was not strong enough to cause a large displacement of the heavy glass substrate. A device fabricated using a quartz cover slip with a significantly lower thermal expansion coefficient ($\alpha = 0.59 \times 10^{-6}$ /^{o}C at 20 ^{o}C) showed a smaller degree of initial drop in the BEL intensity and hence displacement when compared to a normal glass cover slip ($\alpha = 9\times 10^{-6}$ /^{o}C at 20 ^{o}C) (Figure 6b). We note that quartz coverslips are slightly heavier (0.18 g) than glass coverslips (0.14 g). However, this difference in mass cannot explain the smaller degree of initial drop in BEL intensity for quartz (~15%) as compared in for glass

(~99%). In a given short circuit system, the electrical current flows through low resistance path and it delivers high energy in short amount of time. The electrical power (*P*) is equal to potential (*V*) multiplied with current (*I*). The associated electrical energy (*W*) is equal to power (*P*) multiplied with time (*t*). We believe this electrical energy can convert into heat. A heat-induced mechanical jerk in the electrode due to current flow and thermal expansion of the upper surface of the glass substrate in contact with the electrode may collectively aid in displacing the whole device.

From AFM measurements, we note that the initial displacement of the device increases as the maximum EC generated increases (Figure 4b and Figure 7). We observed that for a short-circuit device, an initial upward displacement of 235 nm from the original focused position before application of an external potential) occurs when a sinusoidal potential ranging from +3 V to -3 V is applied (Figure 7c). The device does not return to its original position at zero current, and the displacement between the positions of the device at maximum EC (at +3 V/-3 V) and zero current (at 0 V) during the application of a modulating potential is ~150 nm (Figure 7c); which is in agreement with the results of Figures 4b, 4c and 4d.

The initial upward movement in AFM in image in Figure 7 is related to the drop in initial intensity in Figure 4b, 4c and 4d. We discount the rapid bleaching of weakly fluorescent impurities as the source of this drop as care was taken to ensure the device did not contain any fluorescent impurity. In addition, had the device contained any impurities, any weakly fluorescence impurities would have caused continuous drop from the start of the measurement (not initial drop 10 s after the start of measurement).

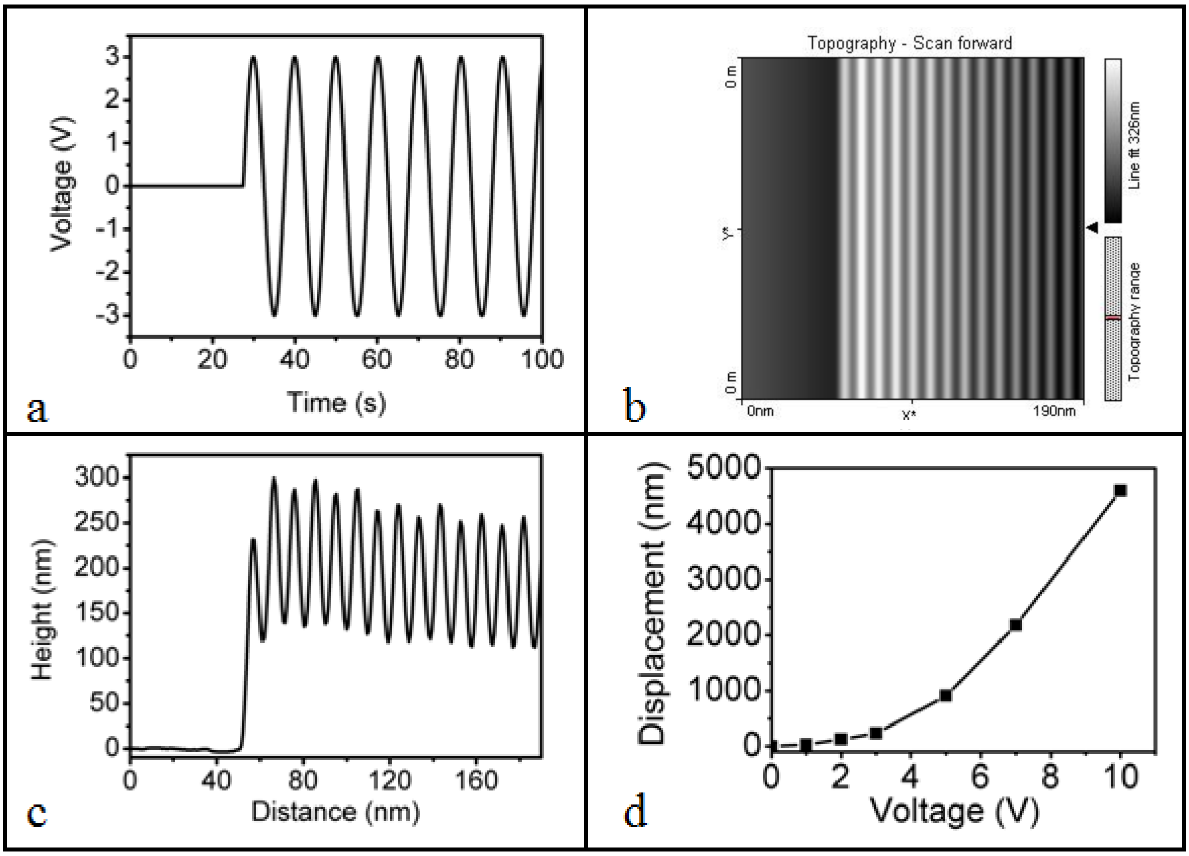

Figure 7: (a) Sinusoidal external potential ranging from +3 V to -3 V (at 0.1 Hz) is applied to a short-circuit device at ~27 s after the start of the AFM scan. (b) AFM image of a single scan (100 s) across 190 nm of the glass substrate and (c) corresponding height profile which correlates with the applied potential. During the application of a sinusoidal potential bias, the grey strips in (b) correspond to a lower height and occur at zero current (at 0 V) whereas the white strips correspond to a higher height and occur at maximum EC (at +3 V/-3 V). (d) Plot of initial displacement of device from the focused position, measured using AFM, *vs*. maximum applied voltage.

3.3.2 Open-circuit device

A typical fluorescence intensity time trace of a single Atto647N molecule in an open-circuit device (Figure 1b) that is subjected to a sinusoidal potential (at 0.1 Hz) ranging from +10 V to -10 V is presented in Figure 8b. The molecule experiences a maximum EF of 1.9×10^5 V/cm when the voltage is adjusted to +10 V/-10 V. The emission intensity of the molecule does not modulate with the EF and is similar to those previously reported for single Atto647N molecules immobilized on a glass substrate[9,10]and PVA matrix.[11] Furthermore, the BEL intensity does not show any significant variation with the applied potential (Figure 8e) and is not EF-dependent. Varying the EF does not cause a sinusoidal-type modulation of either the excitation light focus or dye fluorescence.

The multi-layer open-circuit device in Figure 1b is easily converted to a short-circuit device (*i.e.*, defective device) when the polymer layers between the ITO and Al electrodes are lightly scratched to allow contact between the two electrodes. Single-molecule fluorescence modulation is again observed as illustrated in Figure 8c for an Atto647N molecule in a defective device that is subjected to a sinusoidal potential ranging from +5 V to -5 V. In this case, an alternating EC from 0 to 0.14 A flows across the device at areas where the two opposite electrodes are in contact. Both the fluorescence intensity time trace (Figure 8c) and BEL intensity (Figure 8f) display a sinusoidal modulation with minimum (trough) and maximum (crest) intensities occurring at the highest and zero EC, respectively. Out-of-focus excitation light is thus responsible for the EC-dependent modulation of the single molecule’s fluorescence in a defective device. Furthermore, the fluorescence and BEL intensities are restored at zero potential (or zero EC) to values that are close to those measured before the application of the potential bias (*i.e.*, when the device is in a focused position).

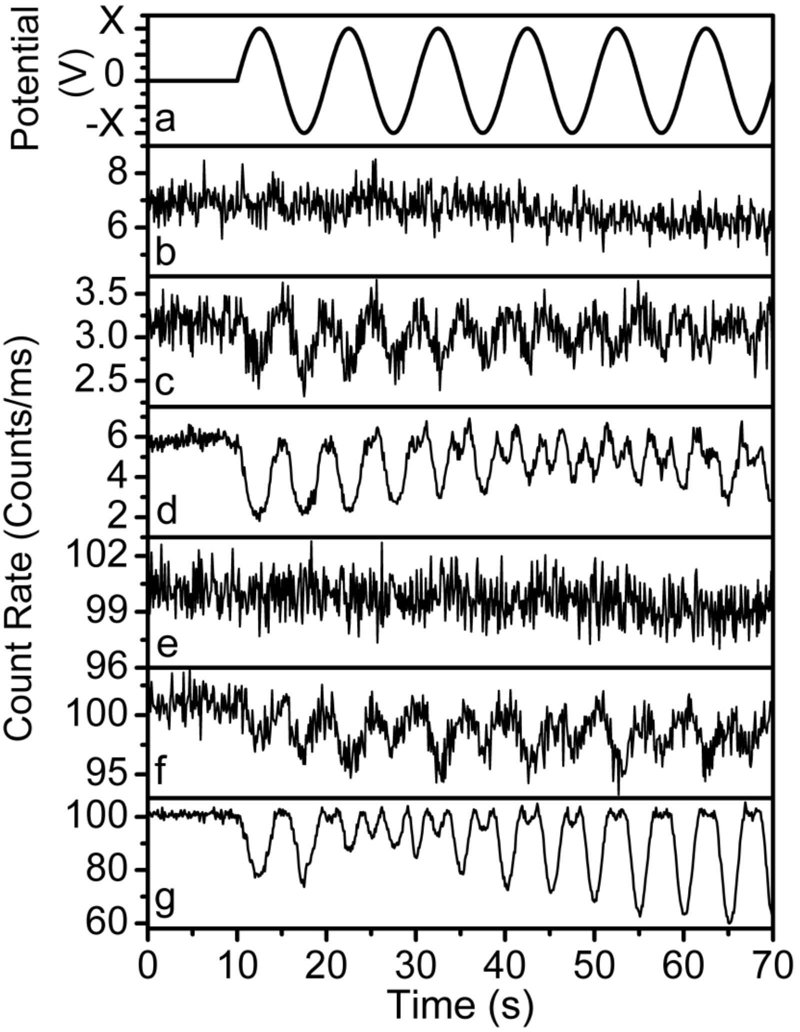

Figure 8: (a) Sinusoidal external potential (frequency of 0.1 Hz) applied to an open-circuit device (b and e) and a defective device (c, d, f and g). (b) Fluorescence and (e) BEL intensity time traces of a single molecule in an intact open-circuit device subjected to a potential ranging from +10 V to -10 V. Fluorescence and BEL intensity time traces of a single molecule in a defective device subjected to a potential ranging from +5 V to -5 V (c and f, respectively) and +10 V to -10 V (d and g, respectively). The external potential was applied 10 s after the start of the measurements and an oil objective lens was used.

This means that the relatively *small* areas of contact between the ITO and Al electrodes are not sufficiently large to cause a significant initial displacement of the defective device.

The fluorescence and BEL intensity time traces of a defective device with an applied voltage ranging between +10 V and -10 V exhibit complex behavior (Figures 8d and 8g). For the first 30 s of the measurement, the fluorescence intensity of the single Atto647N molecule in Figure 8d shows consistent behaviour (*i.e*., crest of intensity trace at zero potential and trough at +10 V/-10V potential). However, a dip in the emission intensity at zero EC is observed at 35 s. The intensity at zero EC gradually decreases over the next few cycles (*i.e*, at 40 s, 45 s, 50 s, etc.) whereas the intensity at +10 V and -10 V increases, such that after 50 s, the trough and crest of the modulating fluorescence intensity time trace correspond to zero and +10 V/-10 V, respectively. This means that an enhancement in the fluorescence intensity is now observed when the maximum EC (0.3 A) is flowing in the electrode relative to the fluorescence at zero current. Similar behavior was observed in the BEL intensity (Figure 8g) where the intensity undergoes a transition from being minimum to maximum at zero potential after 30 s. In this case, the excitation beam becomes out-of-focus at zero current and restores its focus at maximum EC. Several mechanisms such as opposite mechanical movements at zero and maximum currents and types of electrode maybe responsible for this behavior. Future work will focus on elucidating the exact nature of the phenomenon observed here.

3.4 Conclusion

In this chapter, we have unambiguously demonstrated that the drop in the detected fluorescence intensity of single dye molecules in either a short-circuit device (Figure 1a) or a defective device, caused by damaging an open-circuit device (Figure 1b), is due to an out-of-focus excitation beam arising from a displacement of the device away from its focused position by the generated EC in the electrode. For an open-circuit device such as the one depicted in Figure 1b, it is often very easy to damage the thin polymer/active layers so that the two opposite electrodes come into contact with each other. For an example, we have found that an open-circuit device can readily lose its integrity during fabrication and when connecting wires from the generator to the electrodes; hence causing current leaks and out-of-focus excitation to occur. When studying the EF-induced fluorescence modulation of single fluorescent systems, it is imperative to ensure that the open-circuit device remains intact during fabrication, and before and after application of a potential bias. This is necessary to avoid any possible misinterpretation of results in the event that the device is found to be defective. Furthermore, experiments aimed at examining the effects of EC on the fluorescence of single molecules should also be carefully designed to ensure the absence of an out-of-focus beam.

3.5 Movie caption

Movie 1: Backscattered excitation light beam spot pattern with applied potential for a short-circuit device (Figure 1a) that is subjected to a sinusoidal potential (at 0.1 Hz) ranging from +3 V to -3 V. The potential was applied after 4 s.

3.6 References

(1) Zhang, F.; Zhang, G.; Chen, R.; Wang, X.; Siao, L.; Jia, S. *Phys. Scr.* **2012**, *82*, 055303.

(2) Chen, R.; Zhang, G.; Gao, Y.; Siao, L.; Jia, S. *App. Phys. Lett.* **2012**, *100*, 203118.

(3) Park, S. –J.; Link, S.; Miller, W. L.; Gesquiere, A.; Barbara, P. F. *Chem. Phys.* **2007**, *341*, 169.

(4) Hania, P. R.; Scheblykin, I. G. *Chem. Phys. Lett.* **2005**, *414*, 127.

(5) Hania, P. R.; Thomsson, D.; Scheblykin, I. G. *J. Phys. Chem. B* **2006**, *110*, 25895.

(6) Lei, C.; Hu, D.; Ackerman, E. J. *Chem. Commun.* **2008**, 5490.

(7) Zhang, G.; Xiao, L.; Chen, R.; Gao, Y.; Wang, X.; Jia, S. *Phys. Chem. Chem. Phys.* **2011**, *13*, 13815.

(8) Eggling, C.; Ringemann, C.; Medda, R.; Schwarzmann, G.; Sandhoff, K.; Polyakova, S.; Belov, V. N.; Hein, B., von Middendorff, C.; Schönle, A.; Hell, S. W. *Nature* **2009**, *457*, 1159.

(9) Wu, X.; Xing, G.; Tan, S. L.; Webster, R. D.; Sun, T. C.; Yeow, E. K. L. *Phys. Chem. Chem. Phys.* **2012**, *14*, 9511.

(10) Wu, X.; Bell, T. D. M.; Yeow, E. K. L. *Angew. Chem. Int. Ed.* **2009**, *48*, 7379.

(11) Clifford, J. N.; Bell, T. D. M.; Tinnefeld, P.; Heilemann, M.; Melnikov, S. M.; Hotta, J.; Sliwa, M.; Dedecker, P.; Sauer, M.; Hofkens, J.; Yeow, E. K. L. *J. Phys. Chem. B* **2007**, *111*, 6987.

CHAPTER 4

EFFECT OF CHARGE ACCUMULATION ON THE STABILITY OF PEDOT:PSS DURING DEVICE OPERATION

This chapter is adapted from “Effect of Charge Accumulation on the Stability of PEDOT:PSS During Device Operation, Teguh, J. S.; Sum, T. C.; Yeow, E. K. L. *Chem. Phys Lett.*. **2014**, *607*, 52-56.”

4.1.Introduction

Polyethyelenedioxythiophene:polystyrene sulphonic acid (PEDOT:PSS, structure given in Figure 1a) is widely used as a hole transport layer in photovoltaic cells,[1,2] transistors,[3] and organic light emitting diodes (OLEDs).[4,5] Unfortunately, a major drawback of using PEDOT:PSS in OLED is the formation of non-emissive black spots during device operation which is attributed to the reduction of PEDOT.[4] It has been proposed that trace amounts of water that have entered the device or oxidation of the metal cathode results in the creation of reduced PEDOT and a decrease in the effective active area of the device.[4] In another study by Sakamoto *et al.*,[5] the reduced state of PEDOT:PSS is observed in an OLED with a Li-Al/PF8:F8BT blend/PEDOT:PSS/ITO configuration after operation, where PF8 is poly(9,9-dioctylfluorene), F8BT is poly(2,7-(9,9-dioctylfluorene)-*alt*-benzothiadiazole) and ITO is indium tin oxide. The authors have suggested that a portion of electrons injected into the active PF8:F8BT blend from the Li-Al cathode escape into the PEDOT-PSS layer; causing the PEDOT chains to be reduced. Some of the injected electrons from the cathode therefore do not recombine with the injected holes from anode, causing accumulation of electrons and a reduction process to occur in the PEDOT layer.

Many studies have been dedicated to enhance device performances by improving the conductivity of PEDOT:PSS; for example, by ultraviolet irradiation[1] or the addition or solvent treatment.[6,7] Ouyang *et al*. have shown that by treating PEDOT:PSS with ethylene glycol (EG), the conductivity of the polymer increases by nearly 100-fold.[7] This is because EG induces PEDOT chains to undergo transformation from benzoid to quinoid structures where the latter is known to have a higher conductivity. In addition, several studies have also reported the transformation of PEDOT from its quinoid to benzoid structures in an electrochemical environment.[8-10]

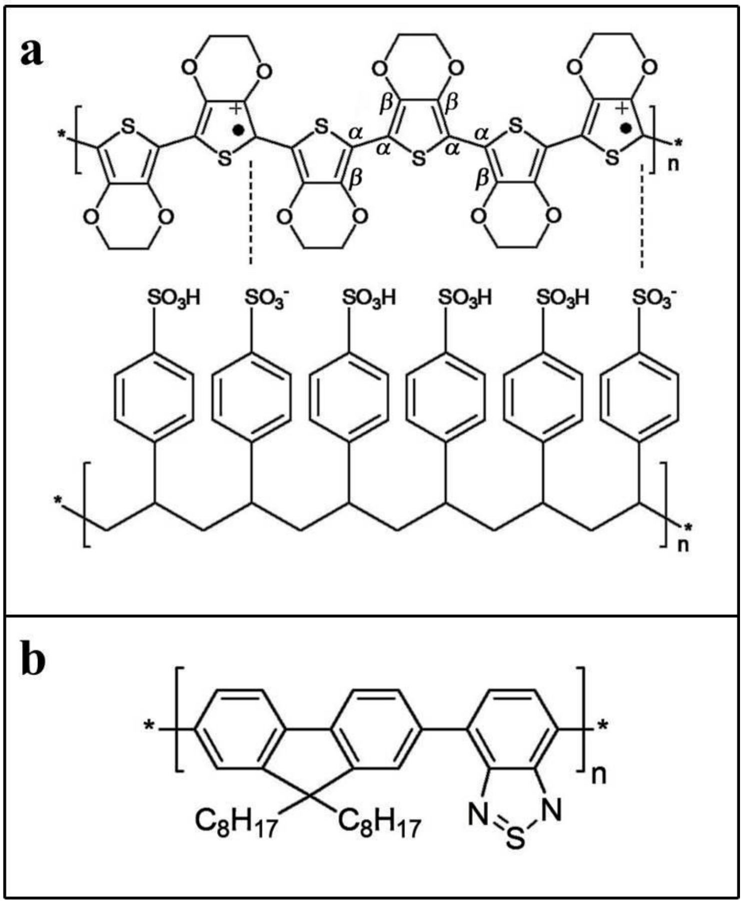

Figure 1: Chemical structure of PEDOT:PSS (a) and F8BT (b)

In this study, we will investigate the effect of charge imbalance (i.e. accumulation of holes in the PEDOT layer) on the stability of PEDOT in 2 devices, device **1** and **2** in Figure 2a, before, during and after device operation using Raman spectroscopy. Device **1** has a simple Al/PEDOT:PSS/ITO configuration whereas device **2** has an Al/F8BT/ PEDOT:PSS/ ITO configuration, where F8BT is emitting polymer (structure given in Figure 1b). The energy diagram of each device is illustrated in Figure 2b. In both devices, ITO is chosen to be anode because of its high electrical conductivity and optical transparency. The experimental time-resolved Raman peaks show that oxidation of

PEDOT occurs when a positive bias is applied. When the voltage is suspended, PEDOT returns back to its (less oxidized) as prepared-state. Since oxidized PEDOT (in its benzoid form) exhibits poorer conductivity than reduced PEDOT (in its quinoid form),[1,7] the conductivity of the hole transporting layer may be compromised during device operation. The conversion between the quinoid and benzoid form of PEDOT during device operation is illustrated in Figure 3.

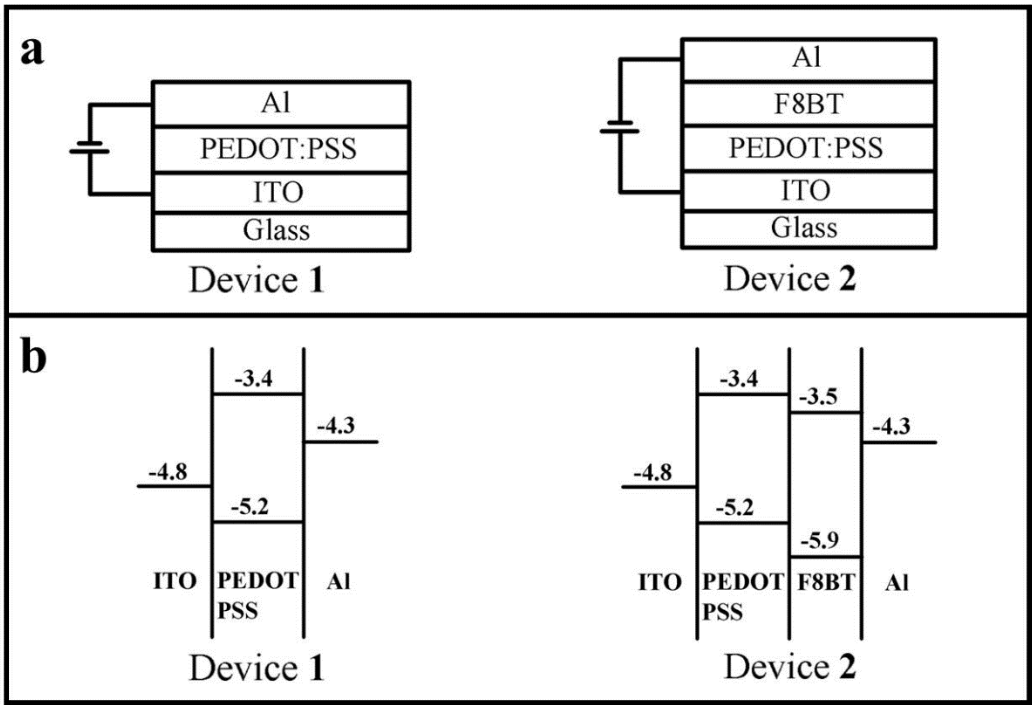
a
Al
PEDOT:PSS
ITO
Glass
Device 1
Al
F8BT
PEDOT:PSS
ITO
Glass
Device 2
b
-3.4
-4.3
-4.8
-5.2
ITO
PEDOT PSS
Al
Device 1
-3.4
-3.5
-4.3
-4.8
-5.2
-5.9
ITO
PEDOT PSS
F8BT
Al
Device 2

Figure 2: Configuration (2) and energy diagram of (b) of device **1** and device **2**.

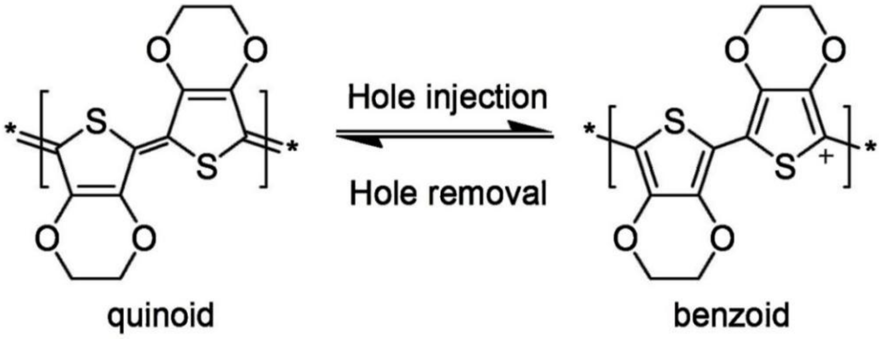
Hole injection
Hole removal
quinoid
benzoid

Figure 3: Reversible conversion between quinoid and benzoid form of PEDOT due to hole injection and removal during device operation.

4.2.Experimental section

4.2.1. Materials

Polyethyelenedioxythiophene:polystyrene sulphonic acid (PEDOT:PSS, 1.3 weight %), tetrabutylammonium hexafluorophosphate and poly[(9,9-di-n-octylfluorenyl-2,7-diyl)-alt-(benzo[2,1,3]thiadiazol-4,8-diyl)] (F8BT, *Mn* 10000-20000) were obtained from Sigma Aldrich. Isopropanol (HPLC/Spectro grade) was purchased from Tedia. Silver paint, indium tin oxide (ITO) coated glass cover slips (20 × 20 mm^2, thickness #1, resistance 8-12 Ω) were purchased from RS Components and SPI Supplies, respectively. Hydrochloric acid (37%) was purchased from Honeywell (Seelze, Germany). Ultrapure water (resistivity 18.2 MΩ.cm, MiliQ) was used.

4.2.2. Device fabrication

Two types of devices were fabricated as shown in Figure 2a. ITO electrode was first patterned using wet-etching method. A sticky tape was used to protect some part of ITO. Subsequently, the substrate was immersed in the mixture of water:HCl (9:1) at 50°C for ~5 minutes to remove unprotected ITO layer. The patterned ITO was rinsed and cleaned using the following steps: baking at 400°C for 1 hour, sonication for 5 minutes in isopropyl alcohol and 5 minutes in water, treating with plasma for 5 minutes and exposure to UV for 15 minutes. In device **1**, 60 nm PEDOT:PSS film was deposited onto ITO covered glass *via* spincoating (SCS G3-8) and was dried at 100°C for 15 minutes. Subsequently, 60 nm of aluminum electrode was deposited through the use of shadow mask via thermal evaporation (KCR-480S Evaporation Coating System) at the rate of ~1Å/s at a pressure ~3×10^{-4} Pa. In device **2**, a PEDOT:PSS film (60 nm) and a F8BT film (60 nm) were deposited in sequence onto an ITO substrate by spin-coating. An Al electrode (60 nm) was subsequently deposited on top of F8BT film by thermal evaporation. The thickness of polymer and aluminum was determined using an atomic force microscope AFM (D3100V, Veeco Digital Instruments). The top view of the device is illustrated in Figure 4. The device area is estimated to be around ~ 4 mm^2.

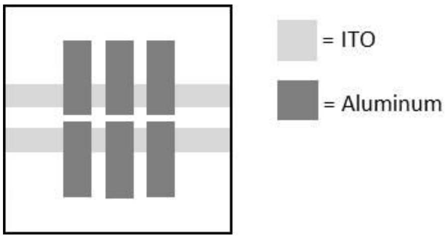

Figure 4: Top view of the device used in this study.

4.2.3. Device characterization and spectroelectrochemistry

Current-voltage (*I*-*V*) characteristic was the device was measured in an argon-filled glovebox with O_2 concentration <10 ppm. The potential (-5V to 5V) was provided by a generator Agilent B2920A and the compliance current was set at 3 mA. The linear response of ln *I* was fitted to Shockley ideal diode equation

$$I = I_s e^{(\frac{V_D}{nV_t})} \ldots\ldots\ldots\ldots \quad (1)$$

where I_s is the saturation current at reverse bias, V_D is the potential across the diode, *n* is the ideality factor and V_T is the thermal voltage (0.026V at 298K).

Spectroelectrochemistry experiments were conducted on a UV-VIS spectrometer (SEC2000, ALS). For the spectroelectrochemical cell, a PEDOT-PSS film (160 nm) on an ITO substrate, Pt and Ag/Ag^+ were used as a working electrode, counter electrode and reference electrode, respectively. The potential difference was provided by a potentiostat (μAuto Lab, Metrohm) and the data was analyzed using GPES Manager software. The spectroelectrochemical experiment was done in acetonitrile with 0.1M tetrabutylammonium hexafluorophosphate as an electrolyte. The solution was purged with nitrogen gas before measurement.

4.2.4. Raman spectroscopy

Raman spectra of device **1** and device **2** during operation were measured using a confocal Raman microscope (LabRAM HR, Horiba). The excitation wavelength used was 633 nm (He-Ne laser, Melles Griot) and the Raman signal was collected using a 50× long working distance objective lens (Olympus LMPlanFLN). The integration time for each spectrum was 60 s and 500 μm pinhole size was used. Since upright microscope configuration was used, the device was mounted with the glass surface facing up and aluminum electrode facing down. The detector used was an electron-multiplying CCD (EMCCD, DU970N, ANDOR) which has classical front-illuminated chip and does not show etaloning effect. All Raman spectra was analyzed using LabSpec 5 software (Horiba Jovin Yvon) and the fluorescence baseline was removed using 2 degrees polynomial function. Throughout the experiment, the laser power and applied external potential were kept minimum to avoid the formation of bubble, black spot and possible photodegradation products.To achieve a positive bias, the ITO anode of the device was connected to the positive terminal of a DC generator (GPC-1850D, Instek) and the Al cathode to the negative terminal.

4.3.Result and discussion

4.3.1. Device characterization and spectroelectrochemistry

The relationship between current *I* and applied bias voltage *V* (-5 to +5 V),and the corresponding semi-ln plot of the *I-V* curves (0 to +5V) for devices **1** and **2** are provided in Figure 5a and 5b, respectively.

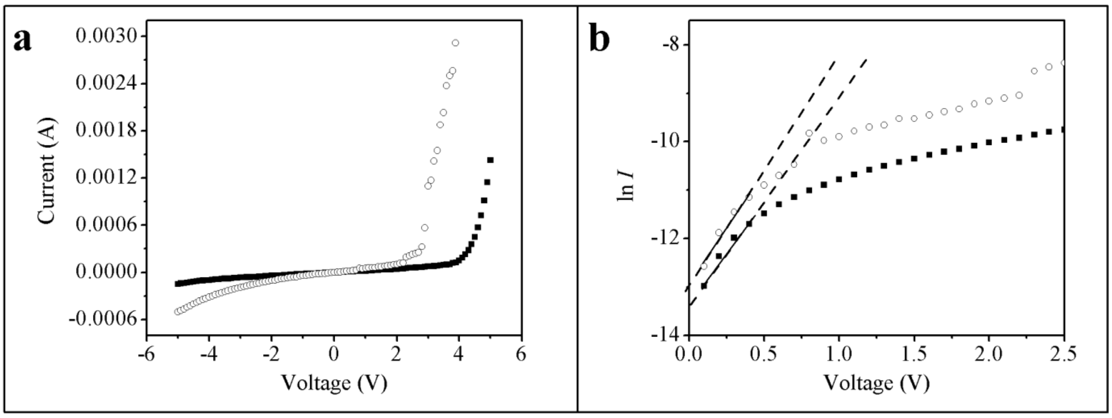

Figure 5: *I-V* characteristics of device **1** (filled square) and **2** (unfilled circle) in the range of -5 to +5V (a) and the corresponding ln *I* vs *V* plots for device **1** (filled square) and device **2** (unfilled circle) (b) The linear response up to +0.4V (dashed lines) was fitted to Shockley diode equation.

A linear relationship between ln *I* and *V* at sufficiently low voltage (up to 0.4 V) suggests that the current increases exponentially with applied potential which is a typical behavior of diodes. Deviation from linearity at higher voltage arises when charge transport is dominated by bulk, rather than interfacial properties.[11] When the linear response of ln *I* is fitted to the Shockley diode equation, an ideality factor of n = 8.8 and 8.1 are obtained for device **1** and device **2**, respectively which is in agreement with the n values reported for other diodes.[11] Therefore, a direct contact between Al and ITO is absent in our devices[12] which function as proper diodes..

The UV-VIS spectroelectrochemical spectra of the PEDOT:PSS used in this study are given in Figure 6. The absorption intensity of electrochemically oxidized PEDOT (applied potential V = +1 V) is lower than that of the as-prepared polymer (V_1= 0 V). When the applied potential is turned off after 5 s, the absorption spectrum collected (V_2 = 0 V) is identical to the as-prepared spectrum observed before application an external bias (*i.e.*, V_1= 0 V). This suggests that the oxidized PEDOT converts back to its natural state when the oxidation reaction is stopped. Upon electrochemical reduction at V = -1 V, the absorbance of PEDOT increases and a new π-π* absorption peak at around 640 nm is observed.[5, 8-10]

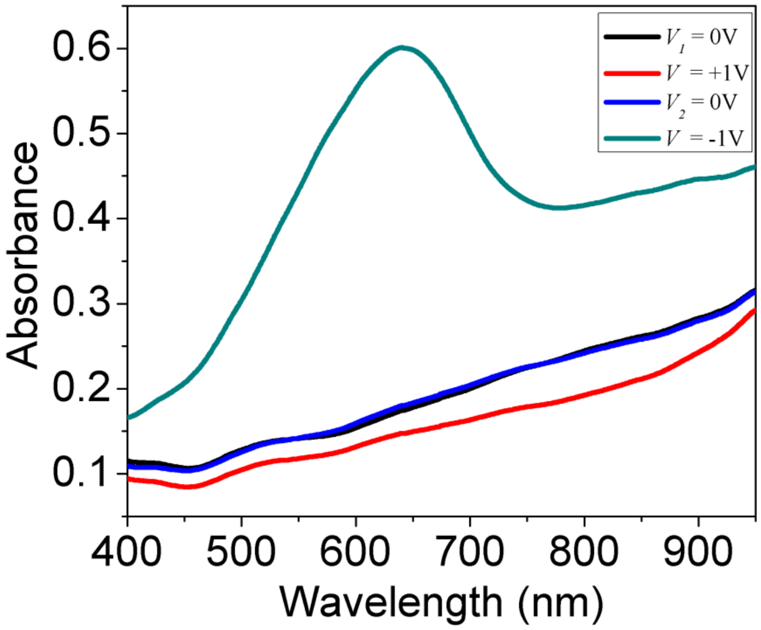

Figure 6: The absorption spectrum of as prepared film of PEDOT:PSS shows broad and featureless spectrum between 400 and 950 nm (V_1= 0V, black line). Absorption of PEDOT:PSS drops upon oxidation (V = 1V red line) and returns to initial intensity when the applied potential is removed (V_2 = 0V, blue line). Absorption spectrum of PEDOT:PSS shows a new π-π* transition peak upon reduction(V = -1V, green line).

UV-vis measurement condition does not tally with Raman measurement condition since the sample preparation was different in both studies. For UV-vis measurement, PEDOT:PSS film was deposited onto ITO as a working electrode and the measurement was done in an aqueous electrochemical environment. For Raman measurement, PEDOT:PSS film was included in a device setting and the measurement was done in a dry condition. Due to these differences, we believe there is no need to standardize the experimental condition. Furthermore for UV-vis measurement, we tried to apply higher voltage or longer wait time. However, the spectrum was not fully reversible, indicating instability of PEDOT:PSS at higher voltage or longer wait time in an electrochemical environment.

4.3.2. Raman spectroscopy

In the Raman spectroscopy experiment, an external potential is applied 5 minutes after the start of the measurement for a duration of 5 minutes before the voltage is turned off. The time-dependent Raman spectra of PEDOT:PSS for device **1** at applied potentials $V = +1.5$ V and +2 V are given in Figure7a and 7b, respectively. We found that PEDOT:PSS layer in device **1** was stable under 1V during 15 minutes measurement. However, since there was no change in the spectrum, we did not further investigate the effect of 1V applied voltage to device **1**. Furthermore, we believe Raman spectrum of PEDOT:PSS is not enhanced since plasmon resonance of aluminum is in deep UV region.

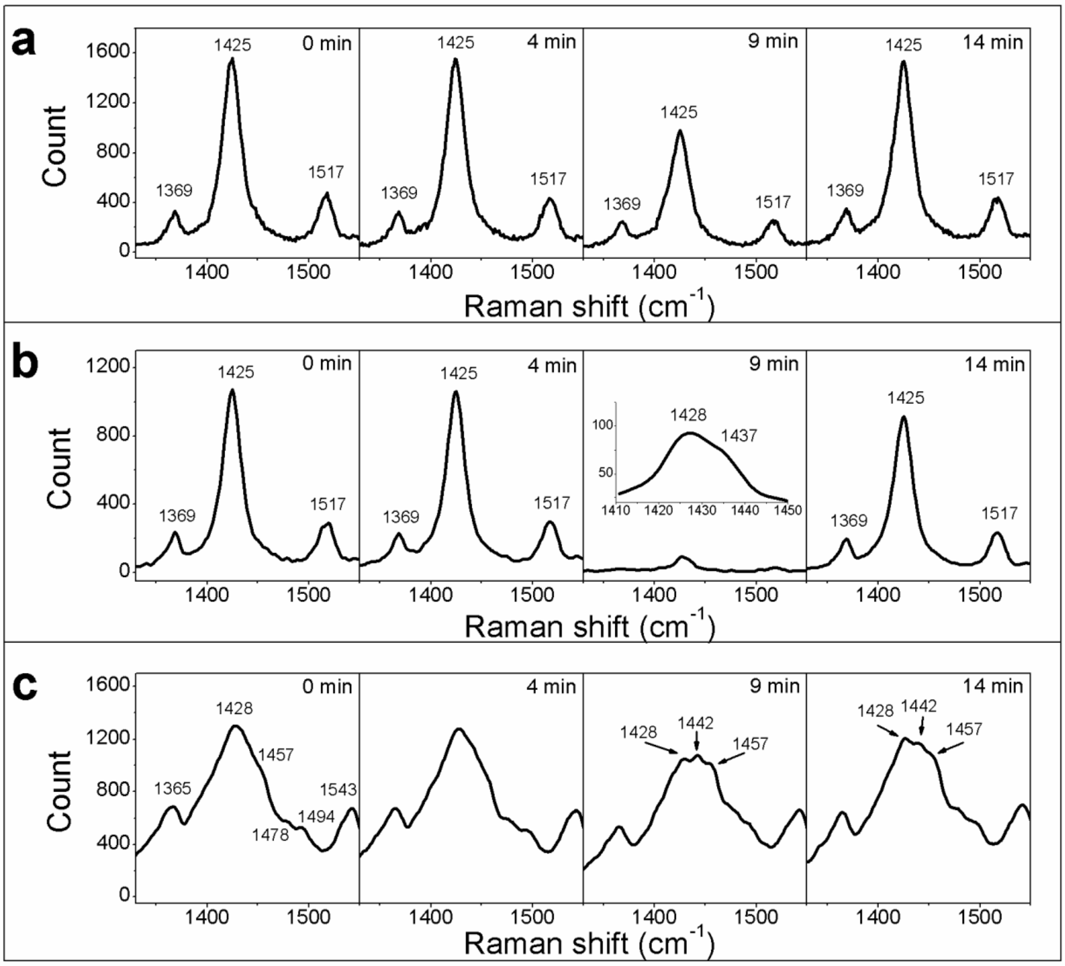

Figure 7: Time dependent-Raman spectra of device **1** at the applied potential of +1.5V (a) and +2V (b) and of device **2** at the applied potential of +3V (c).Spectra were collected at the start of the experiment (0 min, 1st panel) and 4 min later (2nd panel). A spectrum is collected 4 min after during the application of an external potential (3rd panel) and 4 min after the voltage is turned off (4th panel). Raman spectrum of device **1** ((a) and (b)) shows peaks at 1369, 1425 and 1517 cm^{-1} before application of external potential. Application of +1.5V potential induces a decrease in the intensity of 1425 cm^{-1} peak whereas application of +2V induces peak broadening to higher wavenumber (1428 cm^{-1} and 1427 cm^{-1}, inset) in addition to further decrease in intensity. Similar peak broadening is observed for device **2** under the application of +3V potential with the appearance of a new peak at 1442 cm^{-1}.

A low laser power (~ 1.9 μW) is sufficient to yield discernible Raman bands. When no external potential is present, three distinct bands are clearly seen in the 1300–1600 cm^{-1} region: 1369 cm^{-1}, 1425 cm^{-1} and 1517 cm^{-1} peaks are assigned to C_β-C_β stretching, symmetrical C_α=C_β stretching and asymmetric C=C stretching of PEDOT, respectively.[9-10] The Raman signal of PSS is not detected because of its poor conjugation and low Raman cross section. The Raman spectra of at least 10 different spots are recorded for each device and the intensities obtained are consistently uniform (see the Raman spectra collected at 3 different spots in Figure 8). To ensure reproducibility, we have fabricated at least three devices **1** and **2** and we observed reproducible Raman spectra in all devices.

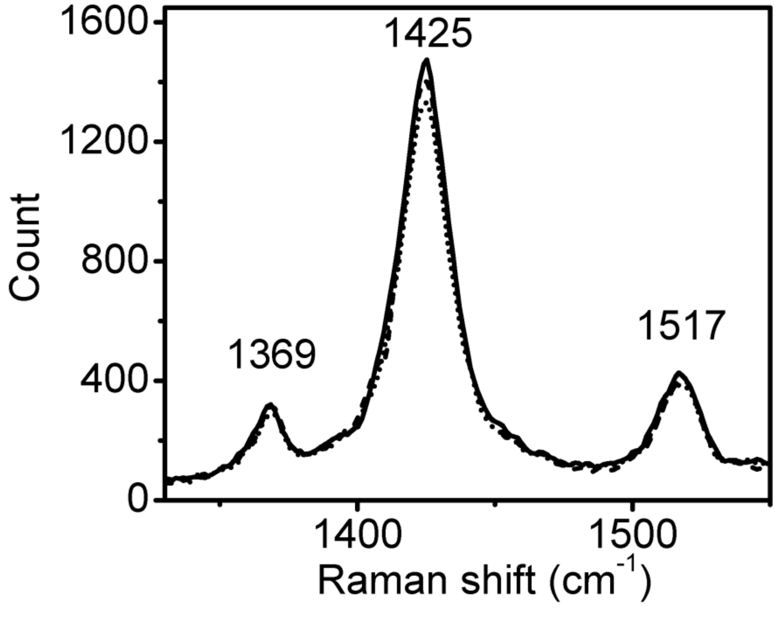

Figure 8: The Raman spectra of device **1** recorded at 3 different spots on the device in the absence of an applied potential.

The position and intensity of the bands collected at the start of the measurement (*i.e.*, 0 min) and 4 min later (with an integration time of 60 s) do not differ significantly.

On the other hand, the Raman bands observed when a forward bias is applied show drastic drop in the signal (Figure 7a and 7b). In particular, a 37% and 91% decrease in the intensity of the 1425 cm^{-1} peak occurs when V = +1.5 V and +2 V are applied for 4 min (*i.e.*, 9 min after the start of the measurement), respectively. Furthermore, in the case of V = +2 V, the band at 1425 cm^{-1} broadens and shifts to higher wavenumber with a peak at 1428 cm^{-1} and a shoulder at 1437 cm^{-1}. This broadening has been observed in study of electropolymerized PEDOT film on ITO and has been ascribed to oxidation of PEDOT:PSS to form a benzoid structure.[9] An interesting observation is the recovery of the Raman signal when the applied external potential is turned off. For example, the intensity of the peak at 1425 cm^{-1} recorded 4 min after the external potential V = +1.5 V is suspended (*i.e.*, 14 min after the start of the measurement) completely recovers back to its original intensity Figure 7a. When the applied potential V = +2 V is turned off, the intensity of the symmetric C=C stretching band is restored to 85% of the original intensity and the peak position returns to 1425 cm^{-1} (Figure 7b).

The as-prepared PEDOT chains exist as a mixture of reduced (quinoid) and oxidized (benzoid) PEDOT.[1,7] It has previously been reported that the principal band located between 1420 to 1430 cm^{-1} for dedoped PEDOT is shifted to higher wavenumber (*i.e.*, between 1440 to 1450 cm^{-1}) for the doped polymer.[9,10,13] From spectro-electrochemistry, we note that the UV-VIS absorption of oxidized PEDOT at the laser excitation wavelength (633 nm) is significantly lower than that for the as-prepared polymer (Figure 6). Therefore, the relatively intense 1425 cm^{-1} peak observed for the as-prepared polymer in Figure 7a and 7b arises from excitation of an electronic transition in the quinoid structure. When a forward bias is applied, holes from the ITO anode are injected into the PEDOT:PSS layer to oxidize the PEDOT polymer (*i.e.*, more benzoid structures are created). The resonance Raman effect is thus inhibited as oxidation reaction takes place and the intensity of the Raman peaks decreases.[14] When a relatively higher potential is applied (*e.g.*, $V = +2$ V), more PEDOT chains undergo oxidation resulting in a larger drop in the Raman signal intensity. In addition, the shoulder at 1437 cm^{-1} observed in the broadened band for $V = +2$ V can be assigned to the $C_{\alpha}=C_{\beta}$ symmetric stretch of the oxidized PEDOT.[10] In device **1**, the work function of ITO (-4.8 eV) is close to the HOMO of PEDOT:PSS (-5.2 eV) whereas a relatively large energy gap exists between the work function of Al cathode (-4.3 eV) and the LUMO of PEDOT:PSS (-3.4 eV) (see Figure 2b). Since the energetic barrier for hole injection (0.4 eV) is smaller than that of electron injection (0.9 eV), the accumulation of holes in the PEDOT:PSS layer and charge imbalance is noted.

When the applied potential is suspended and at sufficiently low excitation power, the majority of unstable benzoid moieties undergo conversion back to the quinoid form, leading to the observed recovery of the Raman signal.[14] This is in agreement with the observed recovery of the UV-VIS absorption spectrum upon stopping the electrochemical oxidation reaction (Figure 6). The re-conversion from oxidized benzoid to reduced quinoid form can be rationalized as follows: the as-prepared PEDOT:PSS consists of quinoid and benzoid PEDOT chains with some positive charges along the PEDOT chains which are balanced by negatively charged PSS chains. During hole injection process, quinoid chains are converted to oxidized benzoid chains, resulting in the excess of positive charge on PEDOT chains which cannot be balanced by the negatively charged PSS. Due to this instability, PEDOT chains reconvert to the reduced form. External voltages higher than +2 V and +3 V are not used in device **1** and device **2**, respectively, as they result in degradation and bubbles forming in the devices.

The Raman spectroscopy of the light emitting device **2** is studied next. In this case, a higher laser power (~ 105 μW) is employed. A standing wave is formed when the excitation light coming from the glass substrate combines with the reflected light from the Al film. Constructive interference gives rise to the Raman intensity observed in typical OLEDs as reported by Friend *et al.*[15] and Sakamoto *et al.*[5] Several plausible reasons may be used to rationalize the lower laser power needed in device **1** such as PEDOT interacting with the excitation and reflected light, location of PEDOT along the optical path or a more homogeneous layer between the glass substrate and Al electrode as compared to device **2**. It is worth mentioning that the exact reason is still unclear at the present moment. A higher applied voltage, compared to the one used in device **1**, is utilized to induce detectable Raman signal changes for the thicker device **2**. Before an external potential is applied, the Raman spectrum of device **2** (Figure 7c), recorded at the start of the measurement (*i.e.*, 0 min) and 4 min later, displays distinct peaks and shoulders at 1365 cm^{-1} (C_β-C_β stretch of PEDOT),[9] 1428 cm^{-1} (C_α=C_β(-O) symmetric stretch of PEDOT in *quinoid* form),[9] 1457 cm^{-1} (C_α=C_β(-H) symmetric stretch of PEDOT),[14] 1478 cm^{-1} (C_α=C_β asymmetric stretch of PEDOT),[16] 1494 cm^{-1} (C_α-C_β asymmetric stretch of PEDOT)[14] and 1543 cm^{-1} (benzothiadiazole ring stretch of F8BT).[4] After an external voltage of +3 V is applied for 4 min, the 1428 cm^{-1} peak is weakened (by ~ 20%) and a concomitant growth of a peak at 1442 cm^{-1},corresponding to the C_α=C_β(-O) symmetric stretch of PEDOT in *benzoid* form,[9] is observed (Figure 7c). This clearly demonstrates that PEDOT undergoes oxidation, probably by holes injected from the ITO anode during operation. In device **2**, the LUMO of F8BT is located at -3.5 eV (Figure 2b), creating an energetic barrier of 0.8 eV at the F8BT/Al interface. Holes are therefore injected at a faster rate as compared to electrons and the accumulation of holes results in the oxidation of the PEDOT layer. When the external potential is turned off, the peak at 1428 cm^{-1} regains intensity which clearly indicates the reversed conversion of benzoid to quinoid structures (see the spectrum collected 14 min after the start of the experiment in Figure 7c).

4.4. Conclusion

The current study shows that the stability of the hole transporting layer PEDOT:PSS is compromised during device operation due to charge imbalance. Holes injected from the ITO anode oxidize the polymer (doping) which causes both a weakening of the principal peak at around 1420 - 1430 cm^{-1}(C_{α}=C_{β}(-O) symmetric stretch of PEDOT) and a band broadening cum shift to higher wavenumber. This behavior is assigned due to transformation of quinoid (dedoped) structure of PEDOT to benzoid (doped) structure of PEDOT. Upon suspending the external applied potential, the oxidized PEDOT converts back to its natural as-prepared state. Future work involves designing experiments, albeit non-trivial, to examine how the conductivity of PEDOT:PSS is perturbed before and during device operation.

4.5. References

(1) Tang, F.-C., Chang, J., Wu, F. –C., Chong, H.-L., Hsu, S. L.-C., Chen, J. –S., Chou, W. –Y.*J. Mater. Chem.* **2012**, *22*, 22409.

(2) Wu, B., Oo, T. Z., Li, X., Liu, X., Wu, X., Yeow, E. K. L., Fan, H. J., Mathews, N., Sum, T. C.*J. Phys. Chem. C* **2012**, *116*, 14820.

(3) Sirringhaus, H., Kawase, T., Friend, R. H., Shimoda, T., Inbasekran, M., Wu, W., Woo, E. P.*Science* **2000**, *290*, 2123.

(4) Kim, J. -S., Ho, P. K. H., Murphy, C. E., Baynes, N., Friend, R. H.*Adv. Mater.* **2002**, *14*, 206.

(5) Sakamoto, S., Okumura, M., Zhao, Z., Furukawa, Y.*Chem. Phys. Lett.* **2005**, *412*, 395.

(6) Kim, J. Y., Jung, J. H., Lee, D. E. Joo, J.*Synth. Met.* **2002**, *126*, 311.

(7) Ouyang, J.; Xu, Q.; Chu, C. –W.; Yang, Y.; Li, G.;Shinar, J. *Polymer* **2004**, *45*, 843.

(8) Lapkowski, M.; Prón, A. *Synth. Met.* **2000**, *110*, 79.

(9) Garreau, S., Louarn, G., Buisson, J. P., Froyer, G., Lefrant, S. *Macromolecules* **1999**, *32*, 6807.

(10) Garreau, S.; Duvail, J. L.; Louarn, G. *Synth. Met.* **2002**, *125*, 325.

(11) Kumar, R,; Khare, N.; Bhalla, G. L.; Kamalasanan, M. N. *Thin Solid Film* 2010, **518**, e61.

(12) Teguh, J. S.; Kurniawan, M.; Wu, X.; Sum, T. C.; Yeow, E. K. L. *Phys. Chem. Chem. Phys.* **2013**, *15*, 90.

(13) Stavytska-Barba, M.; Kelly, A. M. *J. Phys. Chem. C* **2010**, *114*, 6822.

(14) Taylor, D. M.; Morris, D.; Cambridge, J. A. *Appl. Phys. Lett.* **2004**, *85*, 5266.

(15) Kim, J. –S.; Ho, P. K. H.; Murphy, C. E.; Seeley, A. J. A. B.; Grizzi, I.; Burroughes, J. H.; Friend, R. H. *Chem. Phys. Lett.* **2004**, *286*, 2.

(16) Farah, A. A.; Rutledge, S. A.; Schaarschmidt, A.; Lai, R.; Freedman, J. P.; Helmy, A. S. *J. Appl. Phys.* **2012**, *112*, 113709.

CHAPTER 5

FLUORESCENCE INTENSITY MODULATION OF MEH-PPV NANOPARTICLE IN THE PRESENCE OF ELECTRIC FIELD AND ENERGY TRANSFER

5.1 Introduction

Organic semiconductors possess advantages over inorganic semiconductors such as lower production cost and flexibility in synthetic route. One class of widely used organic semiconductors are conjugated polymers. Conjugated polymers find application in chemical sensors,[1] light emitting devices[2] and photovoltaic systems.[3] Various conjugated polymers have been synthesized and studied:polyacetylene, polyaniline and polypyrrole due to their conductivity properties whereas polyfluorenes, polyphenylenes, and polythiophenes due to their electrooptical and photoluminescence properties.[4] Since operation of optoelectronic device requires application of electric field, it is then of great importance to understand the behavior of conjugated polymer in the absence and presence of electric field.

Much study has been dedicated to investigate the properties of conjugated polymers in solution, in thin film and even single polymer chains. In contrast, there are fewer studies on the properties of conjugated polymer nanoparticle (CPN).[4] CPN is typically synthesized via emulsion or precipitation technique. Since CPN is a multichromophoric material, it is many times brighter than quantum dot of similar size.[5] As compared to conventional organic dyes, CPN is less likely to photobleach and blink.[5] Unlike a quantum dot, a CPN is non-toxic in nature, making it suitable as biological probe.[6-8]

CPNs find application in optoelectronic devices. List *et al.* showed that CPN of methyl-substituted ladder-typepoly(*para*-phenylene) could be used as an active layer in an OLED with slightly higher efficiency as compared to the corresponding film based conjugated polymer OLED.[9] This efficiency was attributed due to enhanced electron injection from aluminum cathode which formed ‘stalactite’ structures during evaporation as a consequence of rough nanoparticle layer surface. Scherf *et al.* utilized a blend of two types of CPN (poly(9,9-dioctylfluorene-2,7-diyl-*co*-bis-*N,N'*-(4-butylphenyl)-bis-*N,N'*-phenyl-1,4-phenylenediamine) and poly-(9,9-dioctylfluorene-2,7-diyl-*co*-benzothia diazole)) in photovoltaic devices with external quantum efficiency of 4%.[10] CPN also proved to be an excellent energy donor due to its broad absorption and emission spectra. McNeill *et al.* developed a system of CPN (poly(9,9-dihexylfluorene) and poly(9,9-dioctylfluorene)) as an energy donor with PtOEP (platinum (II) octaethyl porphine) as an energy acceptor.[11] After being excited, CPN transferred its energy to PtOEP which will then emit phosphorescence. Since phosphorescence is quenched by oxygen, this system shows potential as an oxygen sensor in biological system. Xu *et al.* synthesized donor-acceptor system of CPN (poly(9,9-dibromohexylfluorene-2,7-yleneethylene-*alt*-1,4-(2,5-dimethoxy)phenylene)):porphyrinwith surfactant.[12] CPN harvested excitation light and transferred its energy to porphyrin which was then able to change triplet oxygen to singlet oxygen more efficiently as compared to direct excitation of porphyrin alone. Hence, this system holds potential as a photosensitizer in photodynamic therapy against cancer.

In this study, the conjugated polymer MEH-PPV (poly[2-methoxy-5-(2'-ethylhexyloxy)-p-phenylene vinylene]) was used (structure shown in Figure 1a).The optical response of MEH-PPV in the absence of electric field has been studied in bulk and single molecule level. Dilute MEH-PPV solution in tetrahydrofuran (THF) shows maximum absorbance and emission at around 500 and 550 nm, respectively. This large Stokes shift is due to high energy exciton segment transferring energy to low energy segment.[13] MEH-PPV is proposed to adopt a folded conformation in toluene and open conformation in chloroform.[14] A folded conformation increases inter chain contacts and π stacking which will then give rise to low energy segment. Low temperature single MEH-PPV chain fluorescence spectroscopy has been carried out to detect emission from high and low energy segment.[15] In the presence of electric field, the singlet exciton of MEH-PPV film has been suggested to dissociate into charge carriers which will then decrease the fluorescence lifetime.[16] In a single polymer chain study, this charge carrier can respond to electric field by moving along the chain to quench the fluorescence intensity.[17]

We investigated the optical properties of MEH-PPV nanoparticles in the absence and presence of energy donor TPP (tetraphenylporphyrin, structure given in Figure 1b) in bulk and single particle level. In particular, the fluorescence intensity of these systems in the presence of an electric field will be further investigated.

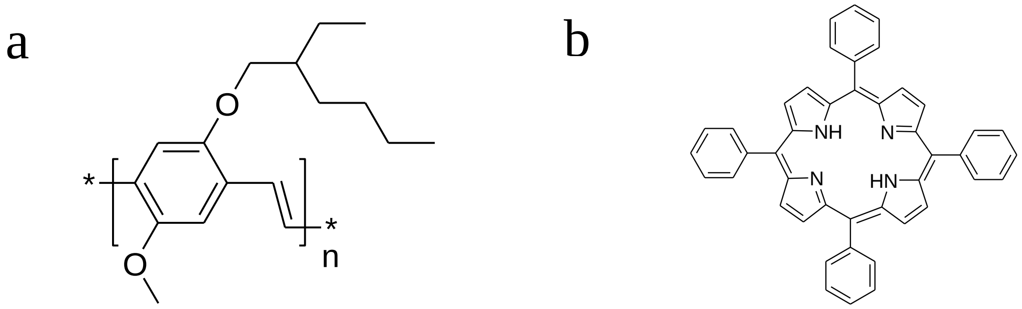

Figure 1: Chemical structure of MEH-PPV (a) and TPP (b)

5.2 Experimental section

5.2.1. Materials

MEH-PPV (*Mn* 200000, *Mw*/*Mn* =4) was purchased from Polymer Source. TPP (≥99%), polyvinyl alcohol (PVA, *Mw* 130000), polystyrene (PS,*Mn* 130000, *Mw* 290000) and THF (HPLC grade)were obtained from Sigma Aldrich Singapore. Ultrapure water(resistivity 18.2 MΩ.cm, MiliQ) was used throughout the experiment. ITO glass cover slips (20×20 mm^2, thickness #1, resistance 8-12 Ω) were purchased from SPI Supplies.

5.2.2. Polymer purification

PS was dissolved in hot toluene under stirring. After cooling down, PS was precipitated via the addition of methanol under sonication. Toluene-methanol mixture was removed and the precipitate was dissolved in hot toluene again. This procedure was repeated several times. PS was then spincoated on a cleaned glass cover slips and was then mounted on confocal fluorescence microscope image. The cleanliness of PS was confirmed from the absence of impurity in the confocal scanning image.

PVA was dissolved in hot water under stirring. After cooling down, PVA was precipitated via the addition of acetone under sonication. After removal of water and acetone mixture, the precipitate was washed with THF under sonication. After removal of THF, the precipitate was re-dissolved in hot water. This cleaning step was repeated several times. The cleanliness of PVA was confirmed using the same step described for PS.

5.2.3. Synthesis of nanoparticles

1 ml solution of MEH-PPV (0.02 mg/ml) in THF was mixed with 2 ml of water under sonication for 20s. THF was then removed from the mixture via vacuum evaporation. Similarly, 1 ml of solution of MEH-PPV (0.02 mg/ml) and 1% TPP (0.0002 mg/ml) in THF was mixed with 2 ml of water under sonication for 20s. THF was then removed from the mixture via vacuum evaporation.

5.2.4. Characterization and bulk spectroscopy

The size of nanoparticle was characterized via the use of scanning electron microscope (SEM, JSM-7600F, JEOL). Absorbance spectrum of nanoparticle was measured using an absorption spectrometer (Cary 100, Varian). For all samples, the concentration was adjusted such that the absorbance was 0.1 at 470 nm. The fluorescence spectrum of nanoparticle was measured using a fluorescence spectrometer (Cary Eclipse, Varian) with 470 nm excitation wavelength.

5.2.5. Device fabrication

An insulating layer of SiO_2 (~230 nm) was deposited via electron beam evaporation system (Edwards). ~40 nm PS film was deposited on top of SiO_2 layer. ~120 nm PVA layer was deposited from a mixture PVA and dilute nanoparticle. Finally, 100 nm aluminum was deposited via thermal evaporation system (KCR-480S Evaporating Coating System). The structure of the device is represented in Figure 2. The device was then connected to a function generator (TG550, Thurlby Thandar Instruments) supplying sinusoidal voltage at 0.1 Hz frequency. The potential was swapped from -10V to +10V. The strength of electric field is estimated to be 2.6×10^5V/cm (ignoring the dielectric constant of the polymer and SiO_2 layers).

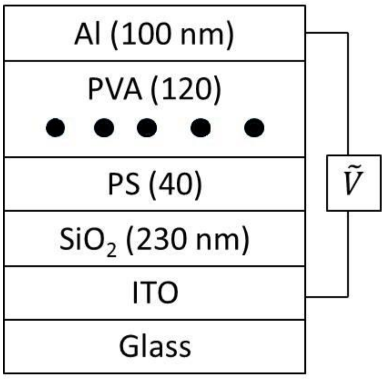

Figure 2: The structure of the device used in this study (● = nanoparticle).

5.2.6. Single particle spectroscopy

The device was held in place at the four corners using a tape in a home-made sample holder and then mounted on a time-resolved confocal microscope (Micro Time

200, Pico Quant GmbH) equipped with an inverted microscope (IX71, Olympus). Excitation light from a pulsed laser diode (470 nm, LDH-P-C-470B, PicoQuant) was passed through dichroic mirror (Z470rdc, Chroma) and focused through oil objective lens (1.4 numerical aperture, 100× magnification, Olympus). Fluorescence signal was passed through an emission filter (HQ570/100M, Chroma) and 100 μm pinhole before being detected by a single-photon avalanche diode (SPCM-AQR-15, Perkin Elmer). Laser power density was adjusted to be 6.33 mW/cm^2.

5.3 Result and discussion

5.3.1. Characterization and bulk spectroscopy

Precipitation technique was utilized in the nanoparticle synthesis. Due to hydrophobic interaction, sudden mixing from good solvent (THF) to poor solvent (water) causes polymer chains to collapse and form spherical surface to lower the surface area.[18] From SEM image, the nanoparticle synthesized here has an average diameter of 75 nm and 81 nm for pure MEH-PPV and MEH-PPV:TPP-1%, respectively (Figure 3). A test was conducted to determine whether TPP was within the nanoparticle or existed as free TPP molecules in the solution. The sample was concentrated using centrifugal concentrator (*Mw* cut off 30000, Pall Corp). Absorption and fluorescence from the filtrate was negligible, indicating that TPP was indeed located within nanoparticle.

The absorption spectrum of MEH-PPV nanoparticle shows maxima at around 490 nm (Figure 4a) whereas normal absorption spectrum of MEH-PPV in THF shows maxima at 499 nm. During nanoparticle formation, polymer chains are forced to bend/collapse in a constrained volume. This may account for such blue shift.[19] The fluorescence spectrum of MEH-PPV nanoparticle shows maxima at around 590 nm (Figure 4b) whereas normal fluorescence spectrum of MEH-PPV in THF shows maxima at around 553 nm. Kink and bends during nanoparticle formation may increase inter chain interaction which gives rise to exciton segment with an even lower energy as compared to free MEH-PPV in THF.

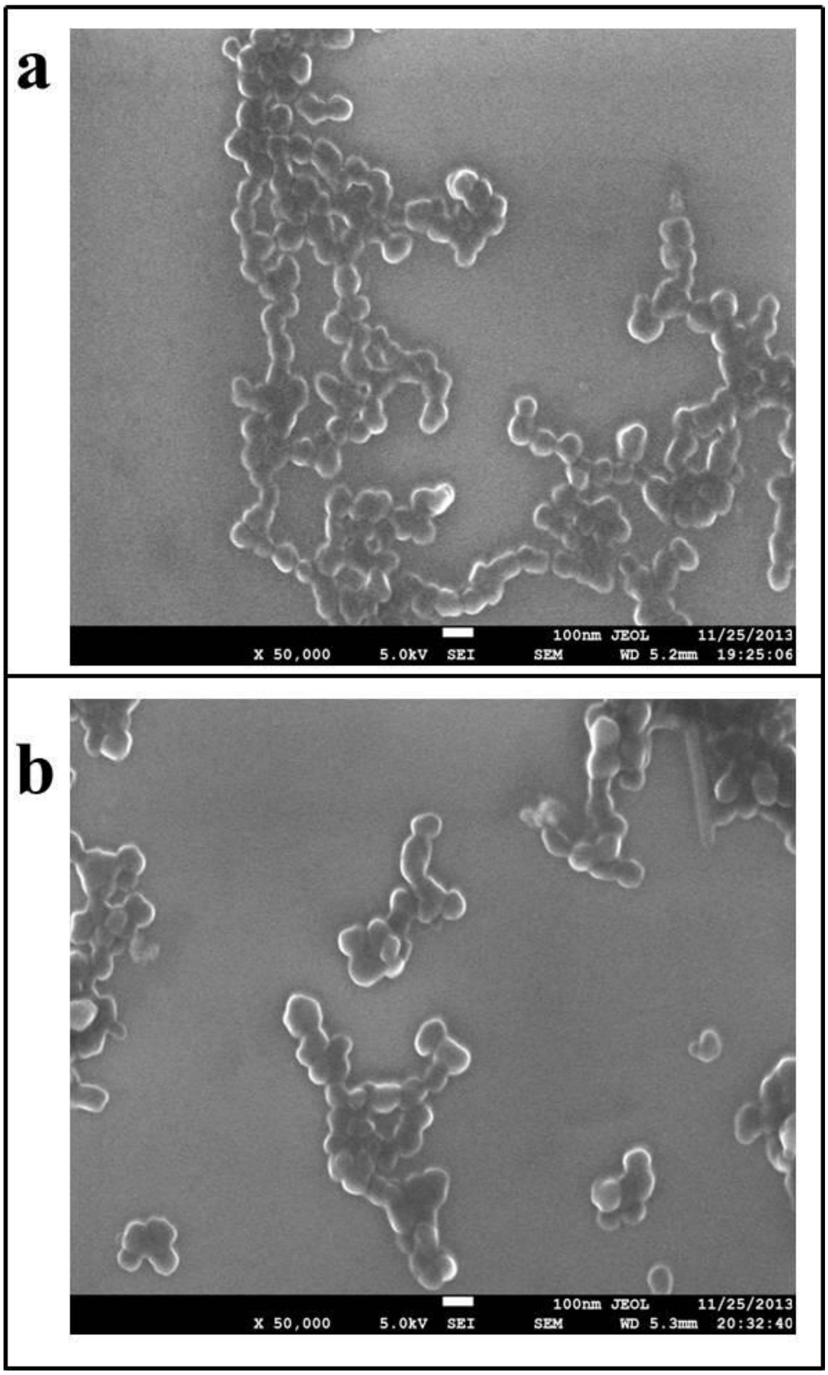
a
100nm JEOL 11/25/2013
X 50,000 5.0kV SEI SEM WD 5.2mm 19:25:06
b
100nm JEOL 11/25/2013
X 50,000 5.0kV SEI SEM WD 5.3mm 20:32:40

Figure 3: SEM image of ~75 nm MEH-PPV nanoparticle (a) and ~81 nm MEH-PPV:TPP-1% nanoparticle (b). The scale bar is 100 nm.

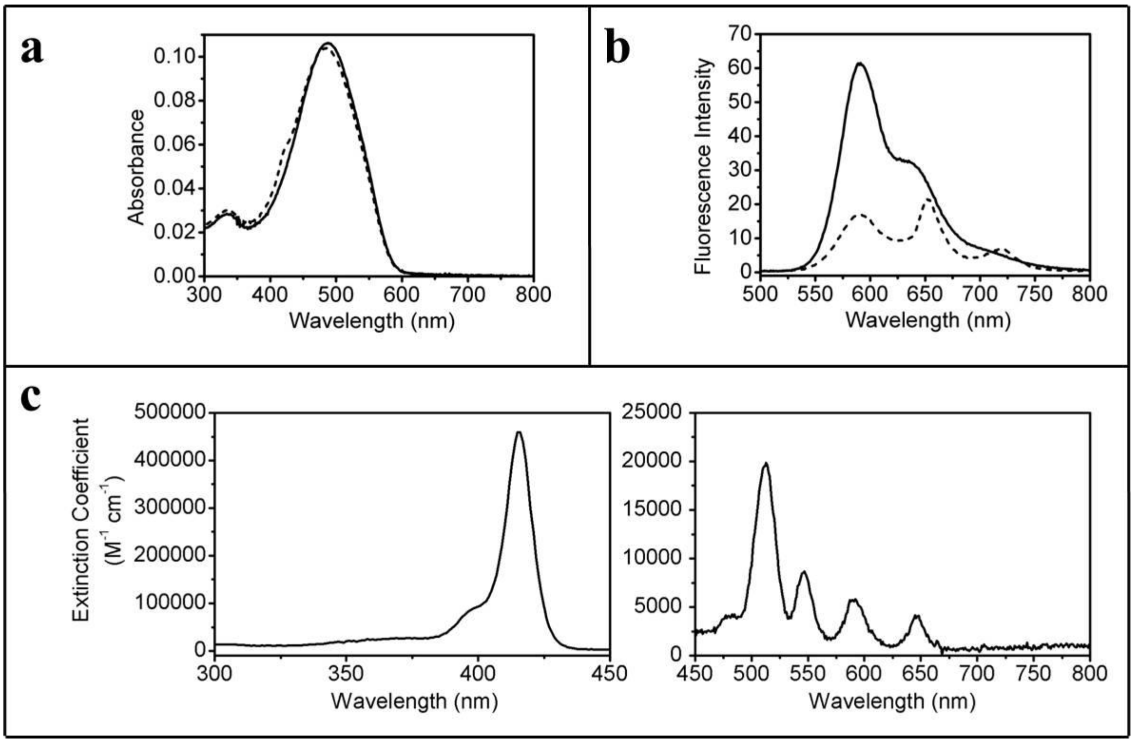

Figure 4: Absorption (a) and fluorescence (b) spectrum of MEH-PPV nanoparticle (solid line) and MEH-PPV:TPP-1% nanoparticle (dashed line). Extinction spectrum of TPP is shown as a comparison (c).

The presence of 1% TPP does not influence the absorbance spectrum to a large extent (Figure 4a, dashed line), except there is weak shoulder at around 420 nm which comes from TPP itself ($S_0 \rightarrow S_2$ transition). On the other hand, 1%TPP quenches the fluorescence of MEH-PPV by ~ 70% (Figure 4b, dashed line). Extinction coefficient of TPP at 470 nm is negligible (Figure 4c) and hence TPP does not fluoresce under excitation light of 470 nm. However, due to efficient energy transfer from MEH-PPV to TPP, emission of TPP can be observed at 650 ($Q_{(0,0)}$ transition) and 717 nm ($Q_{(0,1)}$ transition). We assume quenching occurs via Förster energy transfer mechanism. The efficiency of energy transfer using the formula efficiency (E):

$$E = 1 - F_{DA}/F_D \quad \text{...} \quad (1)$$

where F_{DA} and F_D are the fluorescence of donor in the presence and absence of acceptor, respectively. We calculate energy transfer efficiency of ~ 70% when 1% TPP is attached to MEH-PPV nanoparticle.

5.3.2. Single particle spectroscopy

Single particle spectroscopy was used to study the fluorescence behavior of each nanoparticle in the presence of an applied electric field. Each bright spot in a 10 μm ×10 μm confocal scanning image represents a single nanoparticle (Figure 5a). By focusing laser on each bright spot, one obtains the fluorescence intensity time trace. Typical fluorescence time trace of single MEH-PPV nanoparticle is illustrated in Figure 5c. The external electric field was found to modulate the fluorescence intensity. By combining graph 5B and 5C, one may plot the fluorescence intensity against applied external potential and average it over many cycles (Figure 5e). Modulation of fluorescence intensity (M) can be quantified using the formula:

$$M = (I_{max} - I_{min})/I_{max} \quad \text{..} \quad (2)$$

where I_{max} and I_{min} are the maximum and minimum fluorescence intensity of the molecule during the application of electric field. Modulation of fluorescence intensity is found to be 39% (Figure 5e).

Fluorescence intensity time trace of single MEH-PPV:TPP-1%nanoparticle and its modulation are given in Figure 5d and 5f. We observed that the presence of TPP reduces the modulation of fluorescence intensity of MEH-PPV (M = 29% in Figure 5f). We obtained more than 150 fluorescence time traces of single nanoparticle of MEH-PPV and MEH-PPV:TPP-1% and we calculated the distribution of modulation. The result is presented in Figure 6. From the fitted Gaussian, we found the modulation of fluorescence intensity time trace of MEH-PPV nanoparticle is 36% which is higher than that of MEH-PPV:TPP-1% nanoparticle (23%).

As a comparison, Scheblykin *et al.* observed modulation of 50-100% in the system of single MEH-PPV chain.[17] A possible reason is the stronger electric field they used in their investigation (~1 MV/cm) than in our investigation (~0.27 MV/cm). Lower modulation of MEH-PPV in the presence of TPP can be understood as the effect of energy transfer to single exciton. Presumably, singlet exciton experiences competition between transferring energy to TPP and donating electron to a nearby electron acceptor. It is interesting to compare the fluorescence intensity of single nanoparticle before and after the application of electric field. Electric field seems to enhance or quench the fluorescence emitted from a number of single nanoparticles. This behavior is observed in the absence of TPP (Table 1). In contrast, the presence of TPP significantly reduces the possibility of fluorescence enhancement.

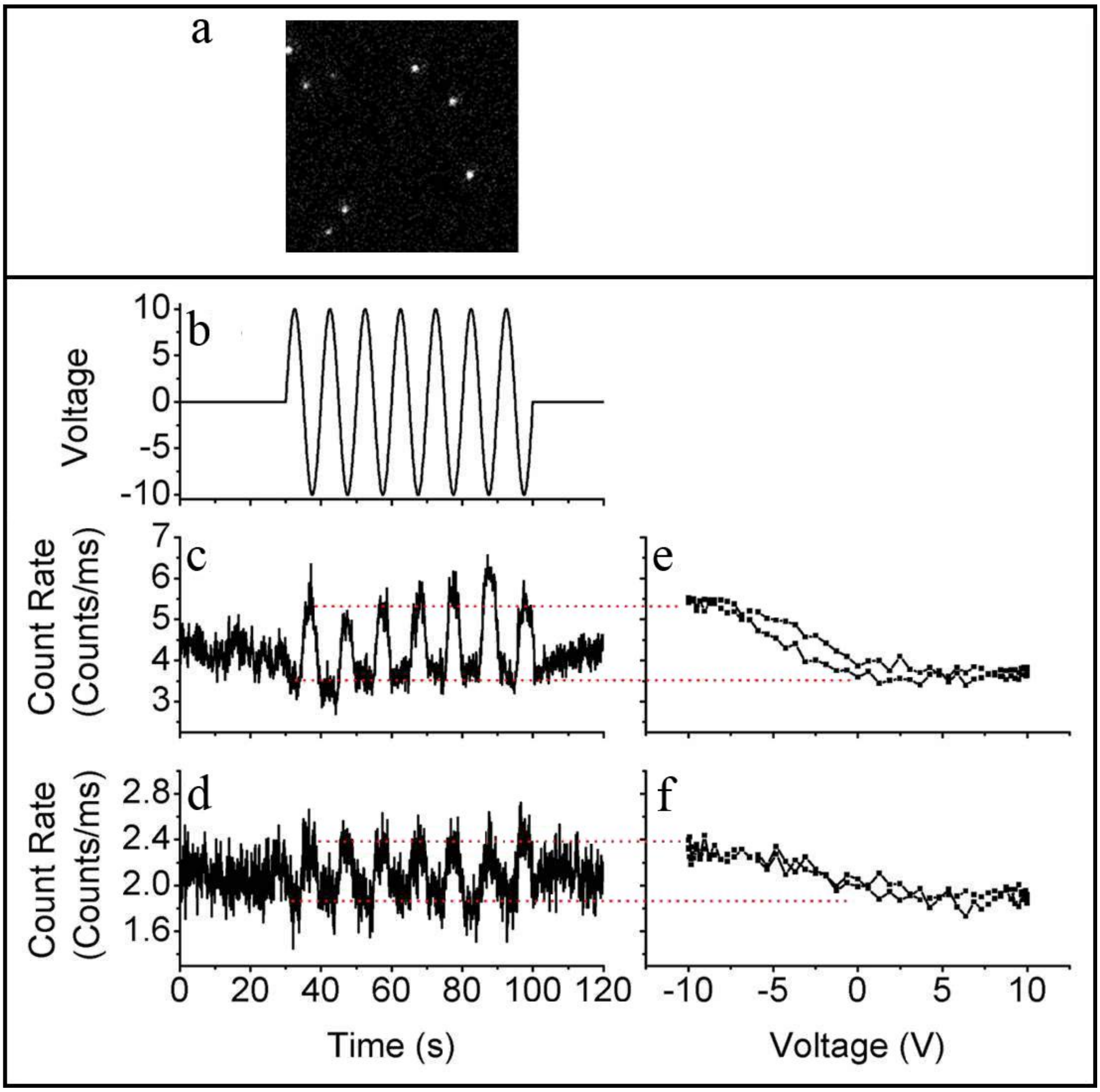

Figure 5: Confocal scanning image of single fluorescent nanoparticle in a 10 μm ×10 μm area (a). External sinusoidal potential (b) induces a change in the electric field which then modulates the fluorescence time trace of MEH-PPV nanoparticle (c) and MEH-PPV:TPP-1% nanoparticle (d). One may correlate graph b and c/d to obtain fluorescence intensity against external potential for MEH-PPV nanoparticle (e) and MEH-PPV:TPP-1% nanoparticle (f).

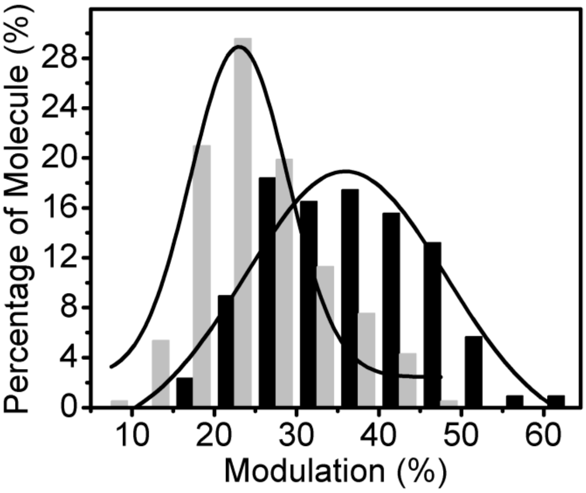

Figure 6: Modulation of fluorescence intensity time trace of MEH-PPV nanoparticle (black) and MEH-PPV:TPP-1%) nanoparticle (light gray). From the fitted Gaussian, modulation of MEH-PPV and MEH-PPV:TPP-1% nanoparticle is found to be 36% and 23%, respectively.

Effect of external electric field	Example	Percentage (%)	
		MEH-PPV	MEH-PPV: TPP
Enhancement	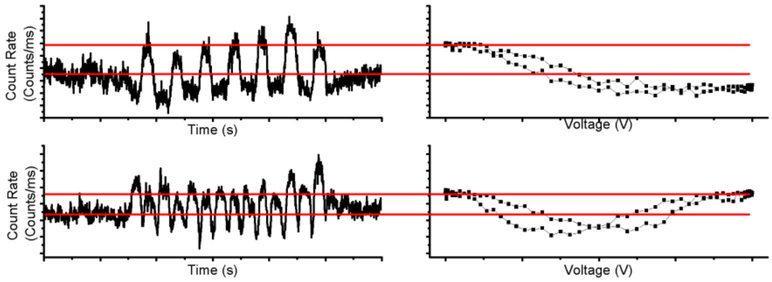	40	11
Quenching	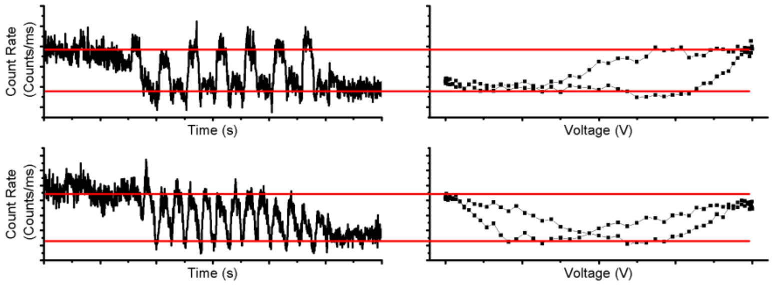	60	89

Table 1: Effect of external electric field in modulating fluorescence intensity time trace of single nanoparticles. It can enhance or quench fluorescence of MEH-PPV nanoparticle. On the other hand, it mainly quenches fluorescence of MEH-PPV:TPP-1% nanoparticle.

MEH-PPV nanoparticle behaves like a ‘bulk’ material consisting of many single polymer chains. A single polymer chain of MEH PPV can adapt various conformations depending on the environment: folded in toluene solvent or open in chloroform solvent.[14] For the same polymer chain, this conformation will then determine the volume occupied by the chain. We note that we are unable to accurately calculate how many polymer chains there are in a nanoparticle due to numerous kinks and bends formed during the synthesis. Nevertheless, we crudely approximate the number of chains using the following method: each MEH-PPV repeating unit occupies ~0.45 nm^3 volume. A spherical nanoparticle with a diameter of 80 nm will possess a volume of ~ 2.68×10^5 nm^3. This means in each nanoparticle there will be 6×10^5 repeating units. MEH-PPV with *Mn* of 200000 used here will have ~800 repeating unit.[20] Hence, each nanoparticle is made up of ~750 chains. This large number of chains shows the degree of collapse and compactness of polymer chains when forming a nanoparticle.

It is interesting to compare the fluorescence intensity modulation of a single MEH-PPV nanoparticle with that of single MEH-PPV chain or MEH PPV film. At low temperature, single MEH PPV chain shows shift in maximum fluorescence wavelength in the presence of electric field (Stark effect).[21] We tentatively exclude Stark effect from this study as the experiment was conducted in room temperature, and hence it greatly diminished any Stark effect due to thermal line broadening.[21] The presence of oxygen has been suggested to quench singlet exciton of single MEH-PPV chain via the formation of charge transfer complex MEH-PPV^+/O^{2-} in the absence[22] or presence of external electric field.[23] Such complex causes fluorescence 'flickering' and can be repaired with the application of external electric field and a hole transport layer.[24] Triplet state of MEH-PPV is known to quench the singlet state of MEH-PPV.[25] The hole injected due to external electric field has been found to quench triplet state of MEH-PPV more efficiently than singlet state.[26] Electric field is found to quench the fluorescence intensity of MEH-PPV film by dissociation of the singlet exciton into electron and hole pair.[27] The same mechanism has been used to explain the electric field induced modulation of fluorescence intensity (quenching or enhancement) in MEH-PPV single polymer.[17]

MEH-PPV is an example of *p*-phenylene vinylene class of polymer (PPV). A widely accepted model to explain charge carrier generation in PPV is the exciton model. Incident light (470 nm in this study) generates first singlet exciton possessing finite binding energy that depends on the molecular structure.[27] This first singlet exciton is basically a bound electron-hole pairs which then dissociates into free carriers under an applied electric field.[28] The binding energy of this electron hole pair is estimated to be ~0.5eV[29] and efficiency of charge carrier generation was estimated to be 42% at 300V/μm field.[28] The fluorescence quenching can then be rationalized as there is lesser singlet excited electron-hole pair which relaxes radiatively. Furthermore, free carrier itself may quench other singlet exciton through charge transfer or energy transfer mechanism. Other than fluorescence intensity, dissociation of singlet state into charge carriers can be evidenced through shortening of singlet fluorescence lifetime.[27] In the context of single MEH-PPV chain, electron is trapped by electron acceptor groups surrounding it. This electron accepting groups could be carbonyl group in the polymer matrix or intrachain contact.[17] Presumably, such intrachain contact leads to π-stacking interaction with lower energy state which acts as an electron trap. Hole polaron is then free to diffuse around due to influence of external electric field.[17] In addition to charge transfer mechanism, hole polaron may quench singlet exciton via energy transfer as its absorption spectra overlaps with that of singlet emission spectrum.[30] In this work, MEH-PPV nanoparticle was dispersed in PVA matrix which has no electron accepting group. In a nanoparticle, a number of polymer chains are compressed together in a compact space. Hence, we assign interchain contact as the possible electron trap. The alternating electric field induces the movement of hole polaron, quenching the fluorescence intensity (table 1). Fluorescence quenching of singlet exciton by hole polaron is not that efficient, probably due to limited quenching volume of ~390 nm^3 as compared to the size of nanoparticle here (~80 nm in diameter).

We note that electric field can enhance fluorescence intensity of conjugated polymer. This phenomenon has been observed in single MEH-PPV chain[17] as well as single composite nanoparticle of polythiophene:C_{60}.[32] In the former, electric-field induced hole polaron quenches triplet state instead of singlet exciton, increasing its fluorescence intensity.In the latter, ultrafast electron transfer from P3HT to C_{60} generates the formationof $P3HT^+/C_{60}^-$ ($P3HT^+$ is a fluorescence quencher) which is driven away from singlet P3HT exciton by the external electric field, thereby increasing the fluorescence intensity. We believe these two mechanisms are in operation for our single nanoparticle here (Table 1). MEH-PPV triplet state quantum yield has been determined to be 1.25%. Since nanoparticle is made up of large number of polymer chains, some singlet exciton may undergo intersystem crossing to triplet state before the application of electric field (0-30s, Figure 5c). This triplet state, quenches singlet exciton; in other words, the fluorescence time trace in the first 30s comes from singlet exciton partially quenched by triplet. During application of electric field (30s-100s, Figure 5c), the dissociated hole polaron quenches this triplet state, thereby restoring the fluorescence. Alternatively, one may want to consider the presence of oxygen since the experiment was carried out in ambient atmosphere. Oxygen may diffuse into the device through the pinhole in aluminum electrode which will then form a charge transfer complex $MEH\text{-}PPV^+/O_2^-$(similar to $P3HT^+/C_{60}^-$ above).[22] This charge transfer complex, like any radical cation, may behave as fluorescence quencher.[33] Similar to the first mechanism, the fluorescence time trace before application of external field comes from singlet exciton partially quenched by the complex. Depending on the conformation and location of this complex, application of electric field may drive this complex away from singlet exciton, hence increasing its fluorescence intensity.

The presence of TPP seems to discourage fluorescence intensity enhancement in the presence of electric field (table 1). The first possible reason is that TPP quenches singlet exciton and hence decreases the number of triplet state. The fluorescence intensity in the absence of electric field (the first 30s, Figure 5d) effectively represents singlet exciton having far lesser triplet state and is partially quenched by TPP. During the application of electric field (30s-100s, Figure 5d), dissociated hole will more likely quench the singlet exciton further. The second possible reason is similar. 1% TPP in MEH-PPV corresponds to mole fraction of TPP:MEH-PPV=3.25:1. TPP is located within nanoparticle. However, it is difficult to ascertain whether TPP is located inside or on the surface of the nanoparticle. Due to the higher number of TPP than MEH-PPV, TPP may be able to 'shield' MEH-PPV from oxygen, reducing the number of MEH-PPV$^+$/O$_2^-$. The fluorescence intensity in the absence of electric field (the first 30s, Figure 5d) effectively represents singlet exciton having far lesser complex state and is partially quenched by TPP. The application of electric field will then influence singlet exciton more than the complex.

5.4 Conclusion

Modulation of fluorescence was observed when MEH-PPV nanoparticle was subjected to external electric field and is attributed due to dissociation of singlet exciton into free charge carrier: electron and hole polaron. Electron is proposed to be trapped in a low energy site such as interchain contacts whereas hole polaron is proposed to move along under the influence of electric field, quenching nearby singlet exciton. The observed fluorescence enhancement is attributed to hole polaron quenching triplet state or to cationic complex moving away from singlet exciton. Modulation of fluorescence was also observed when MEH-PPV nanoparticle was doped with TPP. TPP may quench singlet exciton via an energy transfer mechanism. Since singlet exciton experiences competition between radiative decay and energy transfer relaxation, the fluorescence modulation for MEH-

PPV:TPP system is smaller than that of MEH-PPV. TPP also reduces the likelihood of electric field induced fluorescence enhancement. The reason is proposed to be due to TPP quenching singlet exciton and hence reducing the population of triplet state and charge transfer complex. The free hole polaron will then further quench singlet exciton.

5.5 References

(1) Thomas, S. W., III; Joly, G. D.; Swager, T. M. *Chem. Rev.* **2007**, *107*, 1339.

(2) Grimsdale, A. C.; Chan, K. L.; Martin, R. E.; Jokisz, P. G.; Holmes, A. B. *Chem. Rev.* **2009**, *109*, 897.

(3) Günes, S.; Neugebauer, H.; Sariciftci, N. S. *Chem. Rev.* **2007**, *107*, 1324.

(4) Pecher, J.; Mecking, S. *Chem. Rev.* **2010**, *110*, 6260.

(5) Wu, C.; Schneider, T.; Zeigler, M.; Yu, J.; Schiro, P. G.; Burnham, D. R.; McNeill, J. D.; Chiu, D. T. *J. Am. Chem. Soc.* **2010**, *132*, 15410.

(6) Moon, J. H.; McDaniel, W.; Maclean, L.; Hancock, L. E. *Angew. Chem. Int. Ed.* **2007**, *46*, 8223.

(7) Howes, P.; Thorogate, R.; Green, M.; Jickells, S.; Daniel, B. *Chem. Commun.* **2009**, 2490.

(8) Green, M.; Howes, P.; Berry, C.; Argyros, O.; Thanou, M.*Proc. R. Soc. A* **2009**, *2751*, 9.

(9) Piok, T.; Gamerith, S.; Gadarmaier, C.; Plank, H.; P. Wenzl, F.; Patil, S.; Montenegro, R.; Kietzke, T.; Neher, D.; Scherf, U.; Landfester, K.; List, E. J. W. *Adv. Mater.* **2003**, *15*, 800.

(10) Kietzke, T.; Neher, D.; Kumke, M.; Montenegro, R.; Landfester, K.; Scherf. U. *Macromolecules* **2004**, *37*, 4882

(11) Wu, C.; Bull, B.; Christensen, K.; McNeill, J. *Angew. Chem. Int. Ed.* **2009**, *48*, 2741.

(12) Shen, X.; Li, L.; Wu, H.; Yao, S. Q.; Xu, Q. –H. *Nanoscale* **2011**, *3,* 5140.

(13) Schwartz, B. J. *Annu. Rev. Phys. Chem.* **2003**, *54*, 141.

(14) Huser, T.; Yan, M.; Rothberg, L. J. *PNAS* **2000**, *97*, 11187.

(15) Yu, Z.; Barbara, P. F. *J. Phys. Chem. B* **2004**, *108*, 11321.

(16) Khan, M. I.; Bazan, G. C.; Popovic, Z. D. *Chem. Phys. Lett.* **1998**, *298*, 309.

(17) Hania, P. R.; Thomsson, D.; Scheblykin, I. G. *J. Phys. Chem. B* **2006**, *110*, 25895.

(18) Wu, C.; Szymanski, C.; McNeill, J. *Langmuir* **2006**, *22*, 2956.

(19) Syzmanski, C.; Wu, C.; Hooper, J.; Salazar, M. A.; Perdomo, A.; Dukes, A.; McNeill, J. *J. Phys. Chem. B* **2005**, *109,* 8543.

(20) Schindler, F.; Lupton, J. M. *ChemPhysChem* **2005**, *6*, 926.

(21) Schindler, F.; Lupton, J. M.; Müller, J.; Feldmann, J.; Scherf, U. *Nat. Mat.* **2006**, *5*, 141.

(22) Yu, J.; Hu, D.; Barbara, P. F. *Science* **2000**, *289*, 1327.

(23) Hania, P. R.; Scheblykin, I. G. *Chem. Phys. Lett.* **2005**, *414*, 127.

(24) Gesquiere, A. J.; Park, S. –J.; Barbara, P. F. *J. Phys. Chem. B* **2004**, *108,* 10301.

(25) Yu, J.; Lammi, R.; Gesquiere, A. J.; Barbara, P. F. *J. Phys. Chem. B* **2005**, *109,* 10025.

(26) Gesquiere, A. J.; Park, S.- J.; Barbara, P. F. *J. Am. Chem. Soc.* **2005**, *127,* 9556.

(27) Deussen, M.; Scheidler, M.; Bässler, H.*Synth. Met.* **1995**, *73*, 123.

(28) Esteghamatian, M. Popovic, Z. D.; Xu, G. *J. Phys. Chem.* **1996**, *100*, 13716.

(29) Arkhipov, V. I.; Bässler, H. *Phys. Stat. Sol. (a)* **2004**, *201*, 1152.

(30) Lane, P. A.; Wei, X.; Vardeny, Z. V. *Phys. Rev. B* **1997**, *56*, 4626.

(31) Yu, J.; Song, N. W.; McNeill, J. D.; Barbara, P. F. *Isr. J. Chem.* **2004**, *44,* 127.

(32) Hu, Z.; Gesquiere, A. J. *J. Am. Chem. Soc.* **2011**, *133*, 20850.

(33) Seth, J.; Palaniappan, V.; Johnson, T. E.; Prathapan, S.; Lindsey, J. S.; Bocian, D. F. *J. Am. Chem. Soc.* **1994**, *116*, 10578.